# Hydrous Regions of the Mantle Transition Zone Affect Patterns of Intraplate Volcanism

Helene Wang


Thesis submitted for the degree of
Master in Geophysics and Geodynamics
60 credits

Department of Geosciences and Centre for Earth Evolution and Dynamics
Faculty of Mathematics and Natural Sciences

UNIVERSITY OF OSLO

June 2022

2022

Hydrous Regions of the Mantle Transition Zone

Affect Patterns of Intraplate Volcanism

Supervisors: Clinton P. Conrad, Valentina Magni, Mathew M. Domeier and Grace Shephard

This work is published digitally through DUO – Digitale Utgivelser ved UiO

http://www.duo.uio.no/

Printed: Reprosentralen, Universitetet i Oslo

# Acknowledgments

First and foremost, I would like to express my gratitude to my principal supervisors, **Clinton P. Conrad** and **Valentina Magni**, for their valuable guidance and dedication throughout this project. Clint really awakened my interest in geodynamics by being the wonderful professor he is and has been a great inspiration and help ever since. Likewise, Valentina has supported me by always being available and accommodating whenever I have needed to discuss my work and progress. I have sincerely appreciated having you as my supervisors.

I would also like to express my appreciation towards my co-supervisors, **Mathew M. Domeier** and **Grace Shephard**, for assisting with software guidance, valuable insight, and constructive feedback. In addition, a big thank you to **Krister S. Karlsen** for his commitment, programming guidance and helpful advice during the writing process.

I would also like to thank my friends and fellow master's students at the Department of Geosciences (UiO) for many cheerful lunch breaks and inspiring discussions. Lastly, thank you to my family and loved ones for believing in me, supporting me in everything I do, and for their unconditional love and encouragement.

***Helene Wang***
*Oslo, June 2022*

# Abstract

The Earth's mantle transition zone (MTZ), located between approximately 410-660 km depth, can store an amount of water equivalent to 2-10 oceans of water, which is transported into the deep mantle by subducting oceanic lithosphere. The presence of water is likely to reduce the viscosity of mantle rocks and has the potential to generate melting in the upper mantle that could promote the occurrence of intraplate volcanism (IPV). Therefore, water within the Earth's interior impacts mantle convection dynamics, plate tectonics and could alter the chemical and thermal evolution of the planet. Despite its importance, the amount and spatial distribution of water within the mantle, and its effect on the origin of volcanism far from plate boundaries, are poorly constrained.

Previous modeling studies have estimated rates and volumes of water subducted into the deep mantle based on plate tectonic reconstructions that track the history of subduction through time. In this work, I extend this approach to model the spatial and temporal heterogeneity of water in the MTZ during the past 400 million years (Myr) and compare the predicted regions of wet and dry MTZ with the locations of past and present IPV. I conduct a parametric study where I vary the residence time of water in the MTZ, the slab sinking rate, and the delay period between water in the MTZ and IPV occurrence. Despite the uncertainties associated with the plate tectonic reconstructions and IPV dataset, my models show a remarkable agreement between the hydrated regions of the MTZ and locations of IPV. I find a statistically significant correlation at the 95% confidence level for models where 60-89% of IPV locations occur above wet regions of the MTZ during the past 250 Myr. This confirms the hypothesis that water is transported to the MTZ by subducting slabs and, consequently, causes spatial and temporal mantle heterogeneities. Furthermore, my results show that the MTZ water residence time significantly impacts the distribution of water, with the best fits obtained for residence times of 100 Myr or longer. This implies that MTZ water reservoirs caused by the dehydration of stagnating slabs can remain stable for time periods much longer than the sinking time of a slab. In contrast, the effect of varying the vertical descent rate of slabs and the IPV delay period is modest. However, a delay of 10-50 Myr between water in the MTZ and intraplate eruptions better predicts IPV locations than accounting for no delay. Overall, these findings suggest a link between the formation of volcanism far from plate boundaries and water within the MTZ.

# 1. Introduction

The water located at Earth's surface represents only a fraction of the total water content within the entire Earth System (Hirschmann & Kohlstedt, 2012). A large amount of the water is located within the geosphere, deep inside the Earth's interior. Recent studies estimate that the water content in Earth's interior ranges from approximately one present-day ocean mass (OM = $1.4 \cdot 10^{21}$ kg, Bodnar et al., 2013; Hirschmann & Kohlstedt, 2012) to seven times the present-day ocean mass (Nestola & Smyth, 2016). This extensive range primarily arises from the fact that the water content of Earth's interior cannot be directly measured but has to be estimated (Bell & Rossman, 1992); samples for water analyses are only available from the crust, upper mantle (UM), and very rarely from the mantle transition zone (MTZ, i.e., 410-660 km, Bodnar et al., 2013; Murakami et al., 2002; Smyth & Jacobsen, 2006).

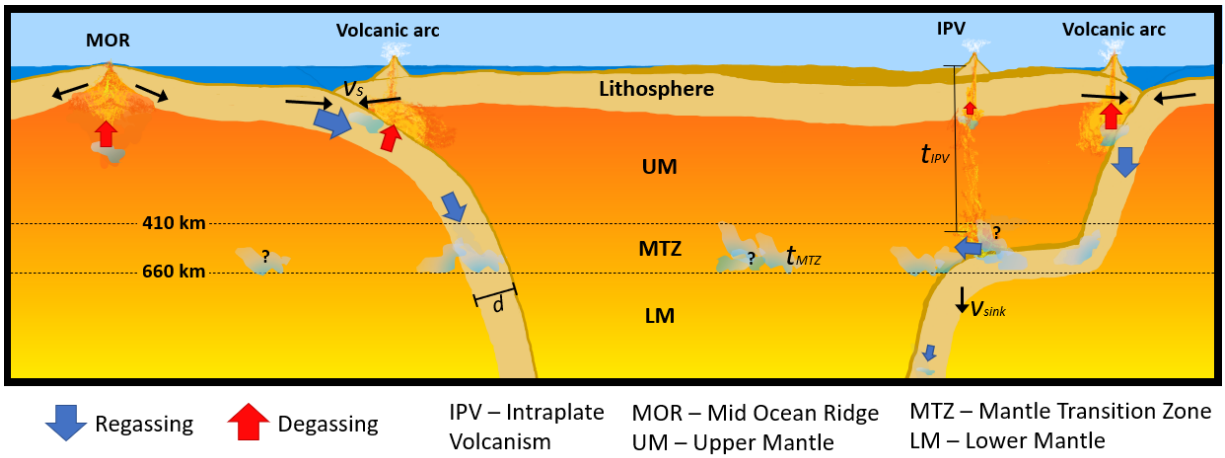


***Figure 1. Schematic of the deep Earth water cycle.*** *Water exchange between Earth's surface and Earth's deep interior is strongly controlled by plate tectonics. Water flux from the Earth's mantle to its surface is governed by degassing (the release of water to the surface) at spreading ridges, arc volcanoes, and through intraplate volcanism (IPV), such as via mantle plumes. Water transport to the deep mantle (regassing) is controlled by subduction – the sinking of the oceanic lithosphere into the Earth's interior with velocity $v_{sink}$. However, the water brought to the deep interior through subducting slabs is highly controlled by the convergence velocity ($v_s$) and slab age (which is coupled with the thickness of the plate, d); some of the water in the slab is released in the mantle wedge triggering partial melting and is degassed at the surface through arc volcanism. The remaining water might be released via dehydration at great depths, e.g., above the 660 km mantle transition zone (MTZ) discontinuity, where slabs often stagnate. Water is plausibly stable at great depths for a significant time ($t_{MTZ}$), possibly even after the slab has continued sinking into the lower mantle. The regionally hydrous MTZ might induce melting, hydrous upwellings, and subsequent IPV that is not plume-related. Eruptions at intraplate locations above water-rich locations in the MTZ could occur an unknown number of million years after the water reaches the MTZ; here, I define this as the IPV delay period ($t_{IPV}$).*

Water exchange between the Earth's surface and interior is controlled by active plate tectonic processes, such as volcanism, seafloor spreading, and subduction (Figure 1; Bodnar et al., 2013; Kelbert et al., 2009; Thompson, 1992; van Keken et al., 2011). Subduction of the oceanic lithosphere may deliver considerable amounts of water to great depths (Hirschmann, 2006). This is due to the fact that subducting slabs contain water in pore spaces within the sediment layer and chemically-bound water within mineral structures of the sediments, oceanic crust, and lithospheric mantle (Faccenda, 2014; Rüpke et al., 2004; van Keken et al., 2011). Subducted water could potentially be stored in significant quantities where mantle conditions allow for large water solubility in minerals, such as the MTZ (Huang et al., 2005; Suetsugu et al., 2006). The water distribution within the Earth's interior is consequently thought to be highly heterogeneous (Peslier et al., 2017).

The MTZ is a zone located between the lower and upper mantle at a depth of 410-660 km (Figure 1). Seismic discontinuities define this zone through phase transformations from olivine to wadsleyite, wadsleyite to ringwoodite, and ringwoodite to silicate perovskite and magnesiowüstite at about 410 km, 520 km, and 660 km depth, respectively. The high-pressure phases, wadsleyite and ringwoodite, allow high concentrations of hydrogen atoms in their crystal structures (up to 2-3 wt.%; Schulze et al., 2018), as opposed to the olivine in the upper mantle and silicate perovskite and magnesiowüstite in the lower mantle (Hirschmann, 2006). Consequently, the MTZ is believed to be a large water reservoir capable of holding more water than the Earth's oceans (Pearson et al., 2014; Smyth & Jacobsen, 2006; Suetsugu et al., 2006). Therefore, the MTZ is the most essential region to investigate when examining the distribution of water within the Earth's interior.

## 1.1 Aim of the study

Constraining the amount and distribution of water in the Earth System is fundamental for understanding the deep water cycle and its effects on the mantle's rheological properties (Hacker, 2008). Without water in the deep Earth, the process of plate tectonics might not be possible (Nestola & Smyth, 2016) because water lowers the mantle's viscosity and initiates melting. Even small quantities of water could significantly affect the viscosity (Hirschmann & Kohlstedt, 2012; Luth, 2003; Wright, 2006) and production of melt (Drewitt et al., 2022; Hirschmann, 2006) of mantle rocks (van Keken et al., 2011). This directly affects mantle convection dynamics, plate tectonics, and chemical differentiation (Faccenda, 2014; Hirschmann, 2006; Kelbert et al., 2009; van Keken et al., 2011). As a result, the Earth cools, and more water enters at trenches, promoting further convection as the viscosity is decreased and melting is initiated. In turn, this further cools the interior of the Earth and prolongs the efficient cooling period. Thereby, water influx to the interior of the Earth will, in the long run, eventually alter the chemical and thermal evolution of the planet (Crowley et al., 2011; Karato, 2011; Korenaga, 2011; Peslier et al., 2017; Sandu et al., 2011; van Keken et al., 2011). Consequently, water cycling between Earth's surface and deep interior impacts the development of oceans, the atmosphere, and life.

In 2014, a rare ringwoodite inclusion in a diamond provided direct proof of the existence of water in the MTZ (Pearson et al., 2014). The ringwoodite was strongly hydrous, containing about 1.5 wt.% $H_2O$. If this water content represents the actual concentration of water in the MTZ and was not just a localized enrichment, the MTZ could store an amount of water proportionate to, or greater than, the mass of the Earth's hydrosphere (Nestola & Smyth, 2016; Peslier et al., 2017). The presence of water in the mantle has previously been investigated through many different approaches. This includes attempts to measure the water content in specific regions of the mantle through seismic wave speeds (Houser, 2016; Meier et al., 2009; Suetsugu et al., 2006), electrical conductivity (Huang et al., 2005; Karato, 2011; Kelbert et al., 2009), and diamond inclusions (Pearson et al., 2014; Shirey et al., 2021; Wirth et al., 2007). At the same time, others have tried to estimate the water content potential through indirect measurements (mineral physics and laboratory experiments, Huang et al., 2014; Schulze et al., 2018), kinematic plate models (Karlsen et al., 2019), and

thermopetrological models (Hacker, 2008; Rüpke et al., 2004; Syracuse et al., 2010; van Keken et al., 2011). Nevertheless, the magnitude and distribution of water in the Earth's interior, both today and in the geologic past, are still poorly quantified and mapped (Hirschmann, 2006).

In principle, it should be possible to estimate rates and volumes of water transport into the deep mantle from models of subduction flux based on plate tectonic reconstructions (e.g., Karlsen et al., 2019). However, the spatial heterogeneity of mantle water content has not been predicted from such models. Significant uncertainties included in the reconstructions themselves, the quantity of water retained by slabs during subduction, and the mechanisms behind the release of these fluids (van Keken et al., 2011; Wang et al., 2015), limit such an approach. The resulting uncertainty in the deep water transport throughout Earth's history is mainly due to the poor constraints on essential factors such as subduction velocity ($v_s$), slab age ($\tau$), slab sinking rates ($v_{sink}$), slab dip, slab lithology, and initial water content (Suetsugu et al., 2006). To better address these variables, I investigate a range of plausible parameters and estimate the spatial distribution of water in the mantle from plate tectonic reconstructions.

In this project, I aim to estimate patterns of heterogeneous water storage in the Earth's mantle over timescales extending 400 million years (Myr) back in time from global plate tectonic reconstructions (Karlsen et al., 2021; Karlsen et al., 2020; Matthews et al., 2016; Torsvik et al., 2019) and identify the link, if there is any, between wet regions in the MTZ and intraplate volcanism (abbreviated as IPV here). Modern, digital plate tectonic models (Gurnis et al., 2012) provide kinematic descriptions of how plates and plate boundaries have moved through geologic time. From these global plate models, one can extract the location of past subduction zones, relative to a given reference frame – such as a mantle reference frame, and the velocity at which convergence across the boundary occurs. By combining the plate kinematic model (I here use the global model of Matthews et al., 2016) with paleo-seafloor age grids (Karlsen et al., 2020 , 2021) the age of the subducting plates can be inferred. Subduction zone locations, plate age, and convergence velocity through geologic time from the kinematic plate tectonic model have here been extracted. I then use them to make predictions of the spatial and temporal distribution of water in the MTZ.

Due to poor constraints on essential factors controlling the locations of subducted water, I investigated several different plausible parameters. This approach resulted in numerous parameterized Earth models that map the heterogeneous storage of subducted water during the past 400 million years. My models enable us to better understand the interplay between the deep water cycle, intraplate volcanism, and water distribution in the Earth's interior, and provide the basis for investigating the effects of these properties in connection with seismic wave velocities and electrical conductivity profiles. In the subsequent sections, we shall see how subduction brings water into the deep mantle, why the MTZ is likely to be the main water reservoir, and how it may be related to IPV.

## 1.2 The deep water cycle

The process of transporting water from the surface into the mantle through subduction is referred to as regassing (Figure 1; Karlsen et al., 2019; Rüpke et al., 2004; van Keken et al., 2011). At the same time, the return of water to the exosphere through volcanism is known as degassing (Figure 1; Bodnar et al., 2013; Karlsen et al., 2019). Over time, the imbalance between regassing and degassing affects the volume of water stored within the mantle and within Earth's surface environment (Andrault & Bolfan-Casanova, 2021). For example, the mantle's water content could increase (or decrease) with time if regassing at trenches is larger than (or smaller than) degassing at divergent boundaries and through volcanism (Houser, 2016). The regassing flux has been estimated to be larger than the degassing flux, both in the present day (Peslier et al., 2017) and in the past (Korenaga et al., 2017). The amount of water transported into the mantle by regassing depends particularly on the kinematics and characteristics of a subduction zone, and in particular, the thermal structure of the slab.

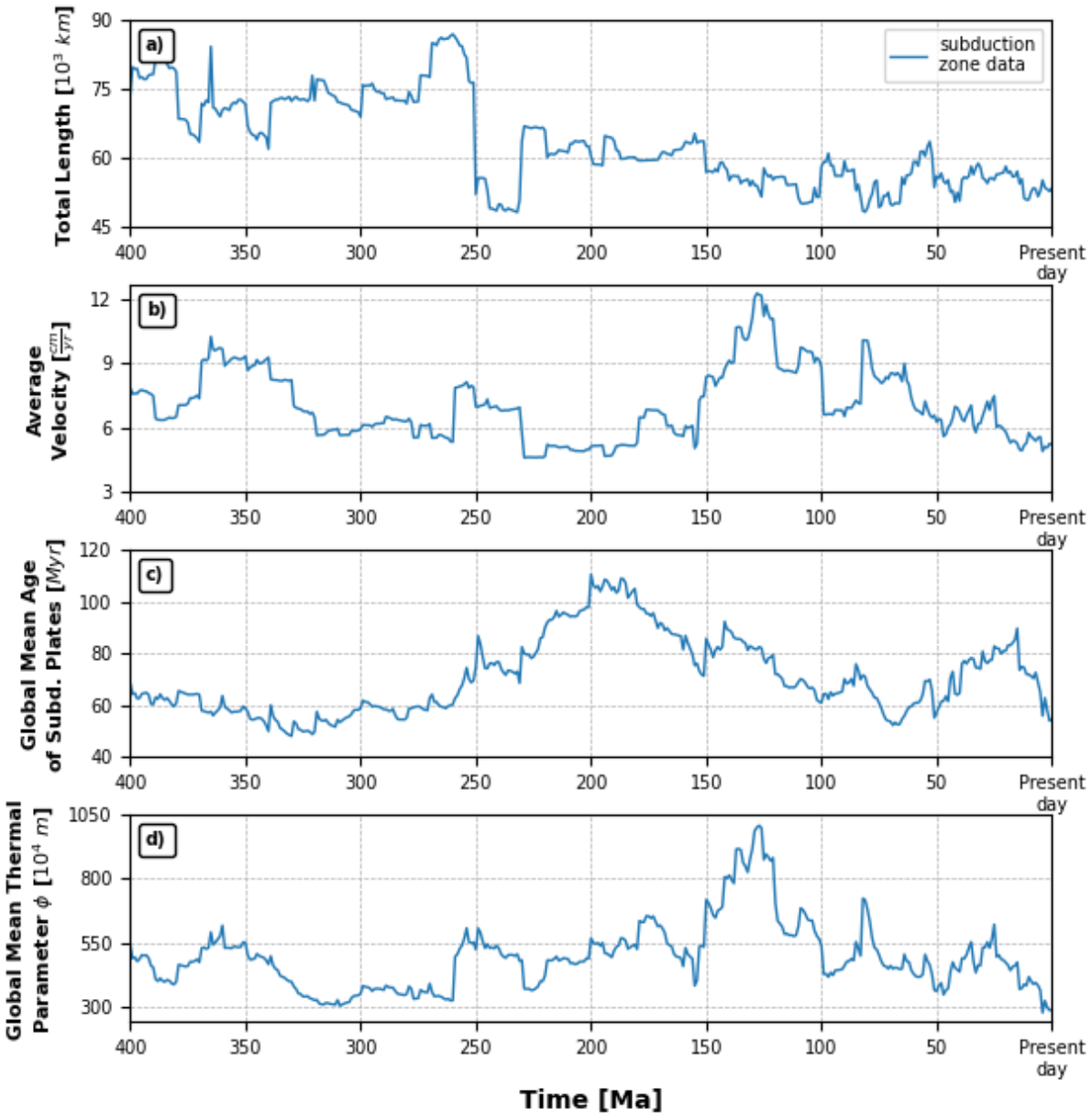


***Figure 2. Subduction-related data applied in this study.*** *Temporal changes in a) the total subduction zone length ($L_S$), b) average convergence velocity ($v_s$), c) global mean age of subducting plates($\tau$), and d) thermal parameter ($\Phi$) of subduction zones between 400 Ma and the present day. The data is extracted from plate tectonic reconstructions of Matthews et al. (2016), modified with the seafloor age model of (Karlsen et al., 2020 , 2021), and regionally updated according to Torsvik et al. (2019). A threshold of 0.2 cm per year has been applied to the velocity data to ensure the inclusion of only active subduction zone segments.*

Hydrous minerals within subducting slabs of oceanic lithosphere, such as mica, apatite, amphibole, serpentine, and chlorite, incorporate water as hydroxyl OH, and are stable only at upper mantle pressure and temperature (PT; Luth, 2003; Peslier et al., 2017). With increasing PT conditions, these hydrous minerals become unstable and undergo phase changes. Either the water is released (dehydration), or their structure is re-arranged in a way that allows the water to remain chemically bound (retention). The latter allows for the creation of high-pressure hydrous minerals, e.g., phase-A (Komabayashi & Omori, 2006), which could stay stable at high pressures, but still requires lower temperatures than those of the ambient mantle. These conditions can be reached inside slabs since subducting oceanic lithosphere has a cold geotherm relative to the surrounding mantle (Long et al., 2019; Syracuse et al., 2010). Therefore, these high-pressure hydrous minerals play an essential role in transporting water to the Earth's interior within slabs (Drewitt et al., 2022). However, dehydration processes often occur during subduction; therefore, only a fraction of the slab's initial water content can be transported into the deeper mantle (Conrad, 2013; Drewitt et al., 2022; Hacker, 2008; Karlsen et al., 2019; Rüpke et al., 2004).

The aforementioned dehydration and retention processes within a slab depend on several factors, of which the descending oceanic plate's subduction velocity ($v_s$, Figure 2b) and age ($\tau$, Figure 2c) are the most significant (Figure 1; Faccenda, 2014; Hacker, 2008; Karlsen et al., 2019; Magni et al., 2014; Rüpke et al., 2004; van Keken et al., 2011). Hot mantle rocks continually erupt at mid-ocean ridges via decompression melting. With time, the newly created oceanic lithosphere moves away from the ridge, cools, and thickens (Schmeling et al., 2017). Old, and therefore cold, fast subducting slabs will have a larger capability to transport water to great depths (ca. >200 km) than young and warm, slowly subducting slabs (Thompson, 1992; van Keken et al., 2011). This is mainly because these fast and old oceanic plates can sustain a colder interior for longer, and thereby hydrous phases within the slab could stay stable to greater depths. van Keken et al. (2011) found indications that mineralogically bound water could efficiently pass into the mantle via old and rapid subduction zones, while almost complete dehydration of the subducting plate was predicted for hot and slowly subducting slabs.

In addition to the convergence rates and age of oceanic lithosphere, subduction zone lengths ($L_s$) are required to estimate the global water retention to great depths. Figure 2 displays data extracted from the plate tectonic reconstruction model from 400 Ma to the present day in single million year timesteps (more details on the used model in Chapter 2; Karlsen et al., 2021; Karlsen et al., 2020; Matthews et al., 2016; Torsvik et al., 2019). The total length of subduction zones has varied greatly with time i.e., between a range of 48-87 $\cdot 10^3$ km (Figure 2a). The length-weighted average convergence velocity also varies; an upper and lower rate of 12.3 cm/yr and 4.6 cm/yr is found at 128 Ma and 229 Ma, respectively (Figure 2b). Additionally, at 200 Ma, the mean age of subducting oceanic lithosphere was twice the present-day value of 54 Myr (Figure 2c). The product of these two factors gives the thermal parameter ($v_s \cdot \tau = \Phi$, Figure 2d), which provides an overall measure of the thermal structure of a subducting slab. Consequently, a large thermal parameter is consistent with high water retention capabilities to great depths. Recently published estimates find that 26% of the global water influx is recycled into the mantle (Magni et al., 2014). In comparison, van Keken et al. (2011) suggest that about one-third of $H_2O$ bound in slabs subducts to a depth of 240 km on average globally. In fact, it has also been suggested that subducted slabs, if sufficiently old and cold, could retain up to 40% of their initial water content to the same depths (Rüpke et al., 2004). More frequent subduction of colder oceanic lithosphere occurred at past times (Figure 2), indicating that the water retention capability of slabs has been likely more significant in the past than it is now. Overall, eight independent studies of regassing fluxes estimated an amount of water subducted into the deep mantle at present-day day to be in the range of 0.0-8.4 $\cdot 10^{11}$ kg/yr with an average of 4.5±1.5 $\cdot 10^{11}$ kg/yr (Bodnar et al., 2013; Faccenda et al., 2012; Hacker, 2008; Magni et al., 2014; Parai & Mukhopadhyay, 2012; Rüpke et al., 2004; van Keken et al., 2011; Wallmann, 2001). Other essential factors controlling the amount of water subducted into the Earth's deep interior are the initial water content, dip angle, pressure, slab lithology, and mantle temperature (Karlsen et al., 2019; Magni et al., 2014; van Keken et al., 2011).

## 1.3 Water distribution in the mantle

The mantle only contains a small fraction of hydrous minerals (Peslier et al., 2017); contrarily, most of the mantle consists of nominally anhydrous minerals (NAMs; Hirschmann & Kohlstedt, 2012; Huang et al., 2014). Water in the mantle and crust is primarily present as trace elements (<0.1 wt.%) in NAMs. In these phases, water is incorporated into the crystal lattice as hydrogen (H) defects (Andrault & Bolfan-Casanova, 2021; Wright, 2006), bounded to structural oxygen (Bell & Rossman, 1992; Huang et al., 2014; Smyth & Jacobsen, 2006). Therefore, I emphasize that the term 'water' in this project accounts for a broader definition than simply $H_2O$ molecules. In this sense, 'water' includes H incorporated as various species in fluids, melts, and minerals (Bodnar et al., 2013; Peslier et al., 2017). Since NAMs mainly make up the mantle, even trace amounts of each mineral could in total represent an enormous amount of water.

The heterogeneous distribution of water in the Earth's interior results from, among many factors, the early planetary differentiation into the core, mantle, and crust and the later infusion of water by subduction of hydrated oceanic lithosphere (Peslier et al., 2017). In silicates, the diffusion of water (i.e., hydrogen) is fast compared to the diffusion of other elements. However, considering the extent of the mantle and the amount of water subducted to the Earth's deep interior, diffusion is not sufficient to cause a uniform distribution of H throughout the mantle. On the contrary, water distribution in the mantle is highly heterogeneous. In fact, it takes ~10 Ga for hydrogen to diffuse ~10 km in typical asthenospheric conditions (Karato, 2007; Kohlstedt & Mackwell, 1998; Peslier & Bizimis, 2015). In addition to the recycling of water-bearing materials via subduction, heterogeneity in the Earth's interior is also sustained by partial melting and subsequent ascent or sinking of melt, and by the inefficiency of convection to homogenize water in the mantle (Peslier et al., 2017).

The distribution of hydrated areas in the mantle depends on multiple factors, many of which are poorly constrained. Most of the water in the Earth's interior is thought to be found in the MTZ. This zone is dominated by the NAMs wadsleyite and ringwoodite, which have significant water storage capabilities in their crystal structure at the PT conditions of the MTZ (Kelbert et al., 2009). The storage capacity is up to 3 wt.% $H_2O$ for wadsleyite and up to 2.8 wt.% $H_2O$ for ringwoodite (Schulze et al., 2018). In comparison, the water storage capacities of NAMs in the upper and lower mantle are estimated to be about 0.005-0.02 wt.% (Hirschmann & Kohlstedt, 2012; Karato, 2011) and 0.002-0.4 wt.% (Murakami et al., 2002), respectively (Hirschmann, 2006). A water storage capability of ~3 wt.% makes the MTZ a potentially important major water reservoir (Pearson et al., 2014; Smyth & Jacobsen, 2006; Suetsugu et al., 2006), possibly capable of holding up to 10 oceans of water (Houser, 2016). A mantle transition zone water reservoir could be stable for millions (Schulze et al., 2018) or >billion (Kuritani et al., 2011) years. However, it is essential to note that the water solubility of wadsleyite and ringwoodite decreases with increasing PT (Bolfan-Casanova et al., 2006; Demouchy et al., 2005; Hirschmann, 2006; Huang et al., 2005). Hence, the water storage capacity of these minerals might become lower at relatively high PT.

Even more significant uncertainty is associated with the lateral extent of water in the mantle since it depends on subduction and mantle convection. The descent velocity of a slab ($v_{sink}$; assumed to be near vertical sinking) is vital because it controls the thermal state of the slab. Moreover, seismic tomography studies have disclosed various slab deformation behaviors at mantle transition zone depths (Karato et al., 2001; and references therein), involving both vertical and lateral deflections. Several slabs, such as under Japan, stagnate at the 660 km discontinuity (Karato et al., 2001; Wang et al., 2015), while some slabs, such as the Cocos Plate, penetrate straight through the MTZ (e.g., Goes et al., 2017). The stagnation, deformation and/or horizontal deflection of slabs are hypothesized to be an essential mechanism of deep mantle hydration (Komabayashi & Omori, 2006; Suetsugu et al., 2006). This is because hydrous phases within the slab may dehydrate by heating from the surrounding mantle during stagnation, hydrating the MTZ (Figure 1). As the MTZ is composed of NAMs with significant water storage capacities, the water released by stagnating slabs could result in a local water enrichment, which could be stable even after the slab continues into the

lower mantle. In addition, the geographic position of wetter regions depends on the diffusion and mixing of water within the mantle, and the regional history of mantle convection (e.g., subduction dynamics, presence of plumes, broad-scale mantle flow, and dehydrating processes such a mid-ocean ridge or plume volcanism).

Several studies have used global seismic wave speeds (Houser, 2016; Schulze et al., 2018) and electrical conductivity (Kelbert et al., 2009) to investigate the present-day lateral distribution of water in the MTZ. Contrasting seismic wave speed studies predicted that the MTZ is variously dry (Houser, 2016), strongly hydrated (Suetsugu et al., 2006), or partly hydrated away from subduction zones (Meier et al., 2009). This diversity could be caused by the different methodologies and by heterogeneities within the MTZ today, as different studies might measure various factors, such as hydrated areas, dry areas, temperature, or major element chemistry (Karato, 2011). However, these discrepancies might also be a consequence of water not being readily detectable by variations in seismic wave speeds in the MTZ (Schulze et al., 2018). Since subduction is the primary carrier of water into the mantle, the position of wetter regions within the MTZ should depend on the location of slabs at depth, and the regassing efficiency of the specific slab. Kelbert et al. (2009) found the highest electrical conductivities in MTZ areas with significant recent subduction input, supporting the widely recognized theory of cold subducting slabs carrying water into the MTZ. Electrical conductivity is the most convenient property to affirm water content due to its high water sensitivity and modest sensitivity to other factors (Karato, 2011).

## 1.4 Intraplate volcanism and hydrous upwellings

Intraplate volcanism (IPV) is defined as volcanism occurring within the interiors of tectonic plates, i.e., away from plate boundaries. IPV can occur within both oceanic and continental plates and is often produced by decompression melting of hot mantle rocks caused by mantle plumes (Wang et al., 2015; Yang & Faccenda, 2020). However, not all IPV is associated with mantle plumes (Long et al., 2019). Indeed, it has been found that the chemical composition of many continental flood basalts (CFBs) differs from that of ocean island basalts (OIBs) caused by mantle plumes (Wang et al., 2015). Moreover, some CFBs exhibit geochemical components equivalent to subduction-like signatures (Merle et al., 2014), although these observations are, by definition, far from plate boundaries. It has been suggested that some IPV may be associated with a locally hydrated mantle transition zone below it (Faccenna et al., 2010; Kuritani et al., 2019; Long et al., 2019; Motoki & Ballmer, 2015; Wang et al., 2015; Yang & Faccenda, 2020). For example, suppose the MTZ becomes locally saturated or hydrated and that MTZ material rises to the upper mantle by mantle convection. Under these conditions, water migrates to the upper mantle, where the NAMs do not have sufficient water storage capacities (Hirschmann, 2006; Yang & Faccenda, 2020). The uplift of hydrous MTZ material has also been hypothesized to be caused by slabs interacting with ancient stable MTZ water reservoirs (Kuritani et al., 2011; Wang et al., 2017). This influx of water lowers the solidus of the mantle above the 410 km discontinuity, resulting in hydrous melting (Wang et al., 2015). At this point, melts generated in the upper mantle would rise and could erupt at the surface, away from plate boundaries (Komabayashi & Omori, 2006; Kuritani et al., 2019), illustrated in Figure 1. This has been suggested to explain Cenozoic IPV in Northeast China (Kuritani et al., 2011; Yang & Faccenda, 2020), where the Pacific slab has stagnated in the MTZ for more than 30 Myr (Long et al., 2019).

Some IPV has also been hypothesized to be caused by a convective instability of stagnant slabs at MTZ depths (Long et al., 2019; Motoki & Ballmer, 2015). Slabs are generally cold and dense compared to the surrounding mantle; however, it has been demonstrated that the base of a stagnant slab could become thermo-chemically unstable. The relatively warm harzburgite underbelly of a slab is less dense than the compositionally (eclogitic) and thermally (cool) denser upper part. Thereby, instabilities could lead to plume-like upwellings. However, the positive buoyancy of these hydrous upwellings is insufficient to sustain ascent to the base of the lithosphere. Therefore, in this case, sublithospheric small-scale convection (SSC) cells are required to bring melt further upwards. If this melt reaches the lithosphere, it may cause volcanism located far from plate margins and above stagnant slabs. In fact, some IPV has globally been observed to regionally cluster above stagnated slabs, in many cases explicitly linked to the slab tip (Motoki & Ballmer, 2015; and references therein; Long et al., 2019). A wet MTZ could, thus, provide an explanation for IPV in the absence of pre-magmatic lithospheric extension or hotspot tracks usually associated with mantle plumes. It could also help to explain findings of subduction-like signatures detected for some intraplate magmatism (Wang et al., 2015; Yang & Faccenda, 2020).

It is important to note that there are many other mechanisms invoked for non-hotspot volcanism; not all IPV events that are not related to plumes are expected to be linked to MTZ water. Some of these other mechanisms include shear-driven upwelling (Ballmer et al., 2013; Bianco et al., 2011; Conrad et al., 2010; Till et al., 2010), lithospheric cracking (Gerbault et al., 1999; Hieronymus & Bercovici, 1999, 2000; Sandwell et al., 1995), sublithospheric convective instability (Ballmer et al., 2007; Bonatti & Harrison, 1976; Dumoulin et al., 2008; Parmentier & Buck, 1986; Parsons & McKenzie, 1978; Richter & Parsons, 1975), and buoyant decompression melting (Aivazpourporgou et al., 2015; Hernlund et al., 2008; Raddick et al., 2002). Notably, these mechanisms are both more likely to occur and to be enhanced if the MTZ is hydrated because water promotes more melting. Establishing affirmative evidence of a correlation between IPV locations and the presence of MTZ water would represent an essential step toward an improved understanding of the deep water cycle. It would also help confirm water content and distribution predictions within the MTZ and serve to identify other possible areas of current and previously regionally hydrated MTZ.

## 1.5 Main hypothesis and goals of the project

The main goal of this project is to predict the spatial and temporal heterogeneous distribution of water in the mantle transition zone and its possible correlation with intraplate volcanism. Existing research on deep Earth water content attempted to measure hydrous regions in the mantle or estimate the potential for water content in the mantle. Instead, I here attempt to predict the most plausible distribution of hydrous regions during the past 400 Myr using tectonic reconstructions of subduction (Karlsen et al., 2021; Karlsen et al., 2020; Matthews et al., 2016; Torsvik et al., 2019).

There is still much unknown about MTZ hydration; I, therefore, allow a few key parameters to vary when undertaking this study. These parameters include the residence time of water in the MTZ ($t_{MTZ}$), the slab sinking rate ($v_{sink}$), and the delay period ($t_{IPV}$) between water in the MTZ and the occurrence of IPV (Figure 1). I hypothesize that there will be more intraplate volcanism, in terms of occurrence, over hydrated regions as compared to regions of no/low hydration. To achieve this, I have therefore compared present and past active continental IPV locations (GROROC, 2021), with various model parameterizations of the wet portions of the MTZ. In simpler terms, I aim to test models of MTZ hydration patterns against continental IPV locations. Any major discrepancies in the presence of IPV above the estimated maps of MTZ hydration, will weaken the hypothesis that a wet MTZ induces intraplate magmatism. By contrast, a notably good correlation between IPV locations and a particular model, governed by specific parameters, would indicate more credibility in this particular model. In addition, I have tested whether the observed correspondence could be a result of random chance by conducting 10.000 re-orientations of the MTZ hydration patterns below stationary IPV locations. In doing so, I hope to establish a testable and solid link between these two important Earth processes.

The applied data and plate kinematic model will be described in more detail in the following section (Section 2.1), along with the various parameters and models used to map the subducted water (Section 2.2). The analysis of the correlation between the processed IPV data (Section 2.3) and predictions of a wet MTZ is further described in Section 2.4. Thereafter follows a presentation of the results (Chapter 3), where findings related to the observed predictions of MTZ water distributions and active IPV regions (Section 3.2) are compared to randomly re-oriented MTZ water contents to investigate the statistical significance of the observed results (Section 3.4). In Chapter 4, I discuss the implications of the presented results and present them in the light of previous studies. Finally, the conclusions of the study are presented in Chapter 5.

# 2. Methods

Because water enters the mantle primarily through the process of subduction, plate tectonic reconstructions can be used to predict the heterogeneous water distribution in the Earth's deep interior. To predict the distribution of mantle water, and to link it to surface volcanism, I developed a Python workflow (Figure 3). Subduction zone locations through time is obtained from state-of-the-art plate tectonic reconstructions and related frameworks (Karlsen et al., 2021; Karlsen et al., 2020; Matthews et al., 2016; Torsvik et al., 2019) to acquire information on where and when subducted water entered the mantle. In order to estimate how much water should be allocated for deep mantle hydration along the specific subduction zone segment, the convergence velocity ($v_s$) and slab age ($\tau$) is extracted from the reconstruction model (following Karlsen et al., 2019). Following on the above, models with various values of slab sinking rates ($v_{sink}$) are computed to track the water transport to the MTZ, along with models of varying MTZ water residence times ($t_{MTZ}$), to estimate the temporal extent of the water in the MTZ. Finally, a comparison of these findings with the locations of active IPV is conducted to test the credibility of these models.

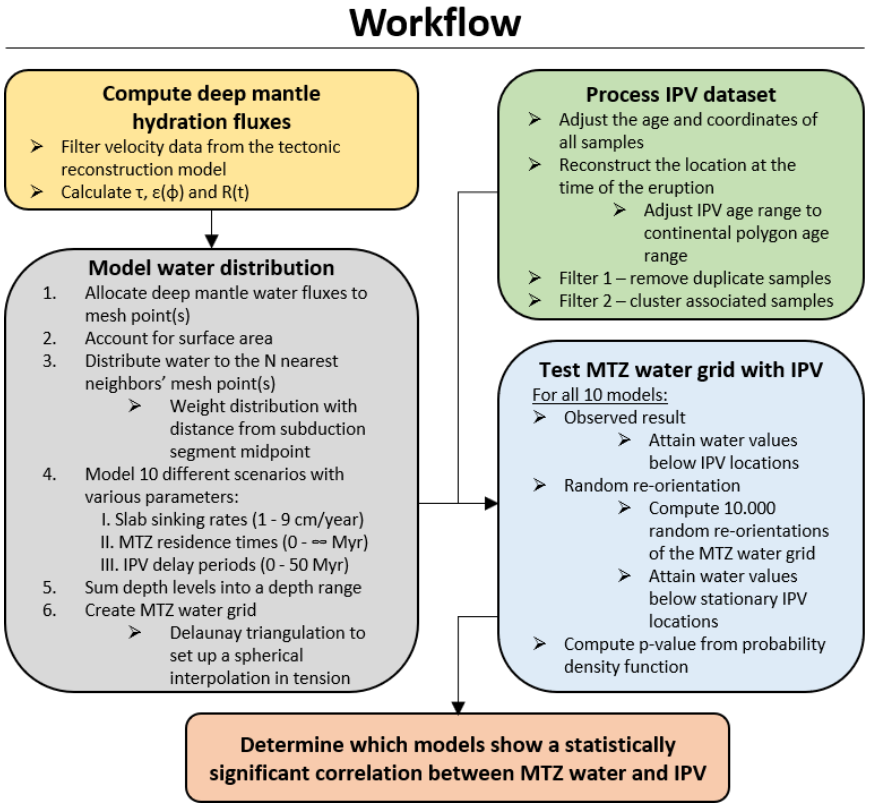


***Figure 3. Flowchart of the work conducted during this thesis**. The numerical modeling steps described in the flowchart were conducted to predict the mantle transition zone (MTZ) water distribution for 10 different scenarios and test correlations with intraplate volcanism (IPV) locations.*

## 2.1 Computing deep mantle hydration fluxes

The data applied in this project for computing subduction water fluxes back in time are based on the global plate tectonic reconstructions of Matthews et al. (2016), modified with the seafloor age model of (Karlsen et al., 2020 , 2021), and with corrections to the reconstruction of the Pacific after Torsvik et al. (2019). This model is constructed upon a mantle-based absolute reference frame and extends from 400 Ma to present-day. This global plate model was constructed from a large number of data from various sources representing different scales (local to global). As such, this published model is subject to numerous uncertainties in global and regional reconstructions, which are not the focus of this study. The tectonic model can be viewed and analyzed via the open-source GPlates software (https://www.gplates.org/; Müller et al., 2018). Henceforth, this model will be referred to as the tectonic reconstruction model. We analyzed this model at 1 Myr increments across its entire 400 Myr duration (400-0 Ma). For every time step, each subduction trench (as identified by metadata in the model) was divided into short (on average 248 km) segments, for which the segment coordinates and their respective convergence velocity ($v_s$), length ($L_s$), and slab age ($\tau$) were extracted (Figure 2a-c). Using this data, the water flux into the deep mantle and its spatial distribution can be calculated and tracked for individual subduction zone segments. The magnitude of water retained at different mantle depths depends on several other factors; however, a range of studies find the slab age and convergence velocity to have first-order control on the regassing of a slab (Faccenda, 2014; Hacker, 2008; Magni et al., 2014; Rüpke et al., 2004; van Keken et al., 2011). Hence, the subduction water flux can be sufficiently parametrized in terms of these two quantities (Karlsen et al., 2019).

***Table 1. Overview of various parameters applied in this study.*** *Including data obtained from the tectonic reconstruction model (Karlsen et al., 2021; Karlsen et al., 2020; Matthews et al., 2016; Torsvik et al., 2019), parameters used to compute deep mantle hydration fluxes, and various parameters applied to create the different models of this study. Description of the various elements used, and their respective symbol and value are listed in the table.*

| Description | Symbol | Value |
|---|---|---|
| **Data obtained from tectonic reconstructions** | | |
| Length of the subduction segment | $L_s$ | Varies with segment and time |
| Convergence velocity of segment | $v_s$ | Varies with segment and time |
| Age of subducting plate segment | $\tau$ | Varies with segment and time |
| **Deep mantle hydration flux parameters** | | |
| Upper mantle density | $\rho$ | 3200 kg/m$^3$ |
| Thermal diffusivity | $\kappa$ | $7.6 \cdot 10^{-7}$ m$^2$/s |
| Constant in water retention function fit | a | -0.1 |
| Constant in water retention function fit | b | 0.5 |
| Constant in water retention function fit | c | 0.0023 |
| Plate thickness | *d* | Varies with $\tau$ |
| Thermal parameter | $\phi$ | Varies with segment and time |
| Nondimensional regassing factor | $\alpha$ | $2.28 \cdot 10^{-3}$ |
| Present day water retention fraction | $\varepsilon(\phi(0))$ | 0.14 |
| Present day regassing flux | R(0) | $3.44 \cdot 10^{11}$ kg/year |
| **MTZ water distribution model parameters** | | |
| Water mass per area | *M* | Varies with segment and *A* |
| Mesh point surface area | *A* | Varies with depth |
| Time step | $\Delta t$ | 1 Myr |
| Slab sinking rate | $v_{sink}$ | 1 - 9 cm/year |
| MTZ water residence time | $t_{MTZ}$ | 0 - ∞ Myr |
| IPV delay period | $t_{IPV}$ | 0 - 50 Myr |
| Number of nearest neighbours | N | 10 |
| Wet MTZ threshold | | $2 \cdot 10^6$ kg/km$^3$ |

An expression for the regassing rate of individual segments is used following the parametrization of Karlsen et al. (2019). The rate of mass transport of oceanic lithosphere into the mantle is described by

$$\frac{dM_l}{dt} = \rho v_s d L_s \qquad \left[\frac{\text{kg}}{\text{year}}\right], \tag{1}$$

where $\rho$, $v_s$, $d$ and $L_s$ are the density, convergence velocity, thickness of the plate and length of the subduction zone segment, respectively (Table 1). To find the regassing rate of the segment, Equation ( 1 ) is multiplied with the nondimensional regassing factor $\alpha$ (Table 1; and described further below) since only a fraction of the initial mass of the lithosphere consists of water. However, most of this water will be degassed through a volcanic arc. To eliminate the water that does not reach the deep mantle, a small fraction $\varepsilon$ (Table 1; and described further below) is multiplied into Equation ( 1 ) as well, leaving us with the deep mantle water flux ($R$),

$$R = \alpha \varepsilon \rho v_s d L_s \qquad \left[\frac{\text{kg}}{\text{year}}\right]. \tag{2}$$

The thickness of the subducting slab is highly dependent on the age $\tau$ of the oceanic lithosphere, and is calculated using the half-space cooling model (Parsons & Sclater, 1977). The plate thickness $d$ is thereby,

$$d(\tau) = 2.32\sqrt{\kappa \tau} \quad , \tag{3}$$

where 80 Myr > $\tau$ > 10 Myr and $\kappa = 7.6 \cdot 10^{-7}$ m$^2$/s (Table 1). For $\tau$ >80 Myr and $\tau$<10 Myr, an upper and lower plate thickness limit of 100 km and 36 km, respectively, have been set (Sclater et al., 1980). In addition, a velocity limit was set to prevent the inactive plate boundaries from being included; these are segments classified as subduction zones that are not converging (and can be considered an artefact of the global plate model's construction). Thus, a threshold of 0.2 cm/yr was applied to the velocity data $v_s$ to ensure the inclusion of only active subduction boundaries. This filtering mainly affects the total length of subduction zones, but does not significantly affect the total area of seafloor subducted (Karlsen et al., 2019) because only inactive or very slowly converging trenches are removed. In addition, while both continental and oceanic subduction zones are included, any 'convergent' boundaries that are not explicitly

identified as a subduction zone by the metadata of the model are ignored, which could cause the dismissal of some actual subduction zones.

The nondimensional regassing factor $\alpha$ relates to the slab's initial bulk water content. I chose a value of $\alpha$ that yields the present-day global $H_2O$ subduction flux of $3.4 \cdot 10^{11}$ kg/yr (Table 1; Karlsen et al., 2019) to depths >230 km estimated by van Keken et al. (2011). This results in a relatively high regassing flux (Karlsen et al., 2019) compared to the findings of most studies (Bodnar et al., 2013; Faccenda et al., 2012; Parai & Mukhopadhyay, 2012; Rüpke et al., 2004; van Keken et al., 2011; Wallmann, 2001); however, the subduction water flux has been predicted to be larger than the degassing flux today (Peslier et al., 2017) and in the past (Korenaga et al., 2017). Additionally, significantly higher regassing fluxes have been estimated for the present Earth (Hacker, 2008; Magni et al., 2014). Furthermore, applying a scenario with a high regassing factor does not significantly affect the mapping of the heterogeneous distribution of water in the mantle. It is thereby suitable for the purpose of this study. The retention factor $\varepsilon$ governs how much of the oceanic lithosphere's initial water content will reach the deep mantle as it descends. The slab's relative water retention factor applied in this study is dependent on the thermal parameter $\Phi$ of each specific subduction zone segment and is calculated by the water retention parameterization, $\varepsilon(\Phi) = max\big(0, a + b(1 - e^{-c\Phi})\big)$, of Karlsen et al. (2019). The constants *a*, *b* and *c* were determined by fitting the function $\varepsilon(\Phi)$ to an independent study of slab water retention (Table 1; Rüpke et al., 2004). The calculated global mean water retention fraction per million years is displayed in Figure 4a.

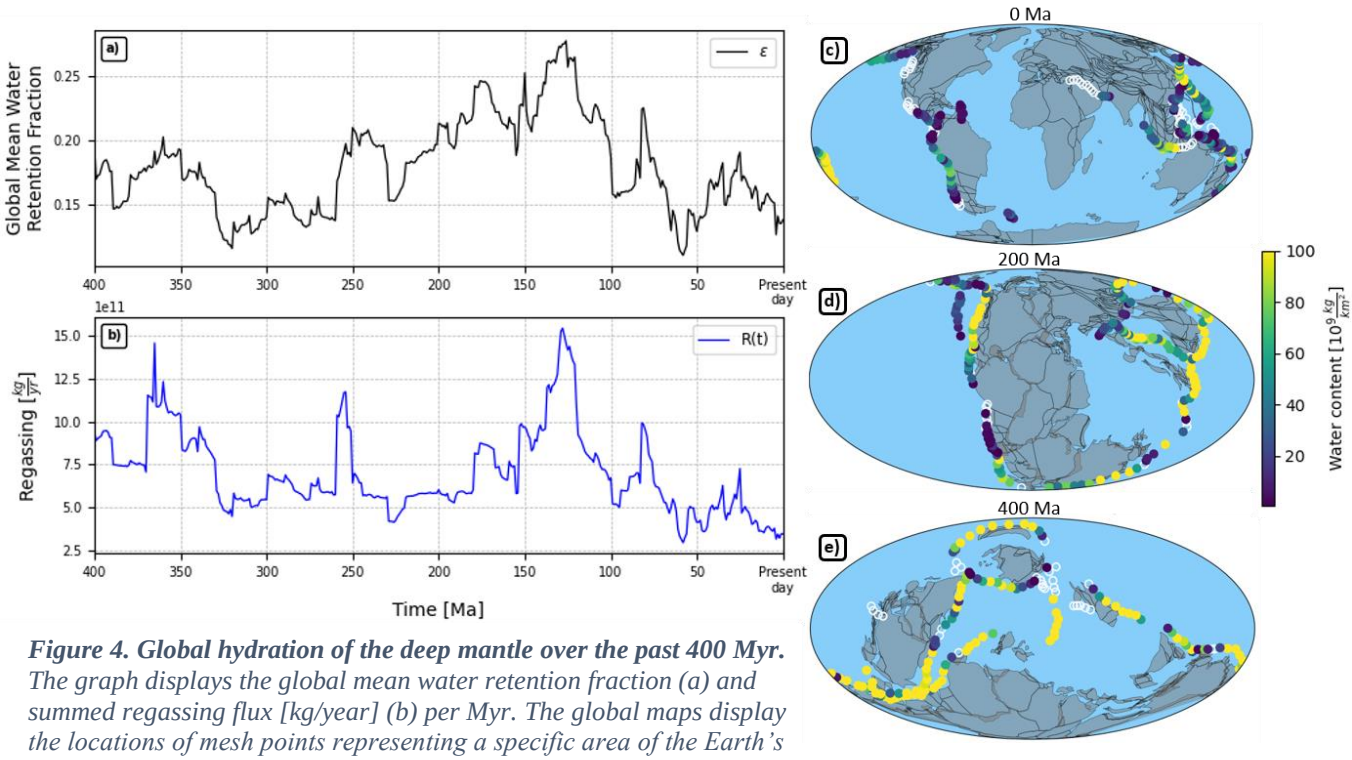


***Figure 4. Global hydration of the deep mantle over the past 400 Myr.*** *The graph displays the global mean water retention fraction (a) and summed regassing flux [kg/year] (b) per Myr. The global maps display the locations of mesh points representing a specific area of the Earth's surface and the location of a subduction zone segment. Each mesh point has received a specific amount of water at 0 Ma (c), 200 Ma (d), and 400 Ma (e). The amount of water [kg/km$^2$] allocated to the mesh points is determined by the regassing of subduction zone segments at the displayed time. In addition, the locations of subduction zone segments that do not contribute to the deep mantle water flux are displayed as hollow white points, along with the (reconstructed) coastlines at the time of subduction.*

I simulate the regassing rates for subduction zones back in time for the period of interest (last 400 Myr). The plate tectonic reconstructions (Karlsen et al., 2021; Karlsen et al., 2020; Matthews et al., 2016; Torsvik et al., 2019) give information on plate boundary evolution and plate motions since 400 Ma. At each point in time, subduction zone segment coordinates, convergence velocity ($v_s$), length ($L_s$), and slab age ($\tau$) are obtained. From these quantities a parameterized estimate of the regassing flux at a specific subduction zone segment can be obtained from Equation ( 2 ),

$$R(t) = \alpha\varepsilon(\Phi)\rho v_s d(\tau) L_s \quad , \qquad (2)$$

for individual subduction zone segments for a given time, $t \in [0,400]$. The summation over all segments per million years is displayed in Figure 4b, alongside global maps of the amount and segment location of subducted water at a specific point in time (Figure 4c-e).

## 2.2 Mapping hydrated regions in the mantle

Producing maps of possible hydrated regions in the mantle require tracking the subducting slabs with time and depth as they descend into the Earth's deep interior. Equation ( 2 ) finds the water flux per segment per timestep [kg/year]. A CitcomS-type mesh (Zhong et al., 2000) was utilized to store the associated water flux values; the mesh is displayed in Figure 5. Despite CitcomS being a code designed for studies of mantle convection (which is not undertaken here), I use the 'CitcomS-type' mesh because it is designed such that the distance between the points is nearly equal on a spherical surface (and thus the points appear to be non-uniform on a rectangular projection). Though the Earth is ellipsoidal, the deviation is slight, and a spherical model is more suitable for global modeling studies.

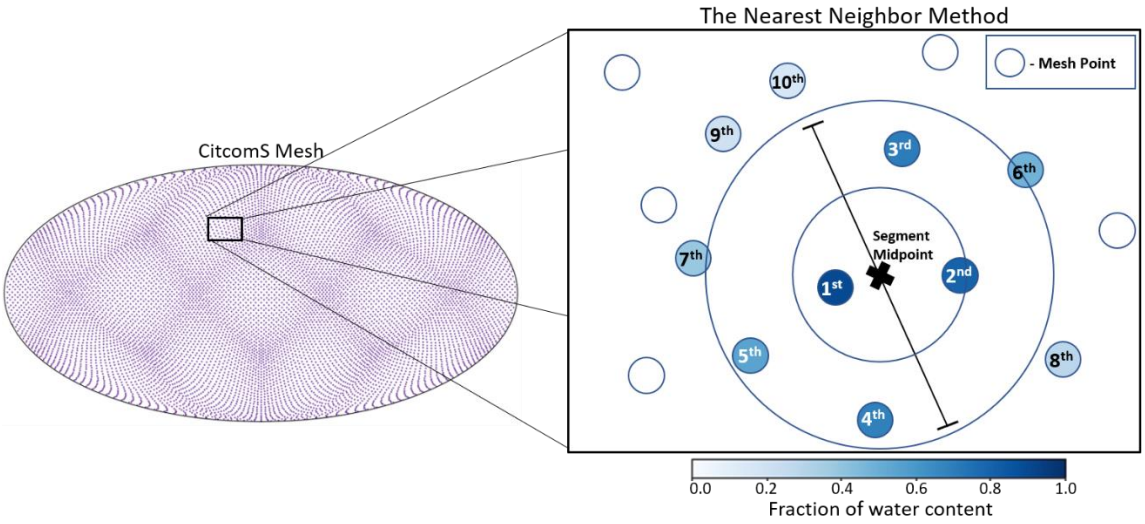


***Figure 5. Global mesh and nearest neighbor method.*** *The left-hand figure shows the global mesh point locations (purple, i.e., 10094 global mesh points based on CitcomS workflow) with the Mollweide projection. The global mesh comprises 12 diamond-shaped "caps" that cause a nearly equal distance between the mesh points on a spherical surface. On the surface of the Earth, one mesh point represent approximately 50.000 km$^2$. In addition, an illustrative figure of the nearest neighbor method, with an arbitrary distribution of points, is displayed on the right-hand side. The illustration shows a segment and its midpoint (marked with an X) where the 10 nearest neighbor mesh points have received a weighted amount of the total water content (blue) associated with this segment midpoint. The associated water, i.e., the regassing flux of the particular segment, is distributed to the 10 closest mesh points based on the distance from the segment midpoint. The closer to the segment midpoint, the more water (darker blue) is added to the mesh point. Likewise, the further away from the segment midpoint, the less water (lighter blue) is added to the mesh point. The mesh points that are not one of the 10 closest points to the segment midpoint will not receive any water (white) from the particular segment displayed in this illustration.*

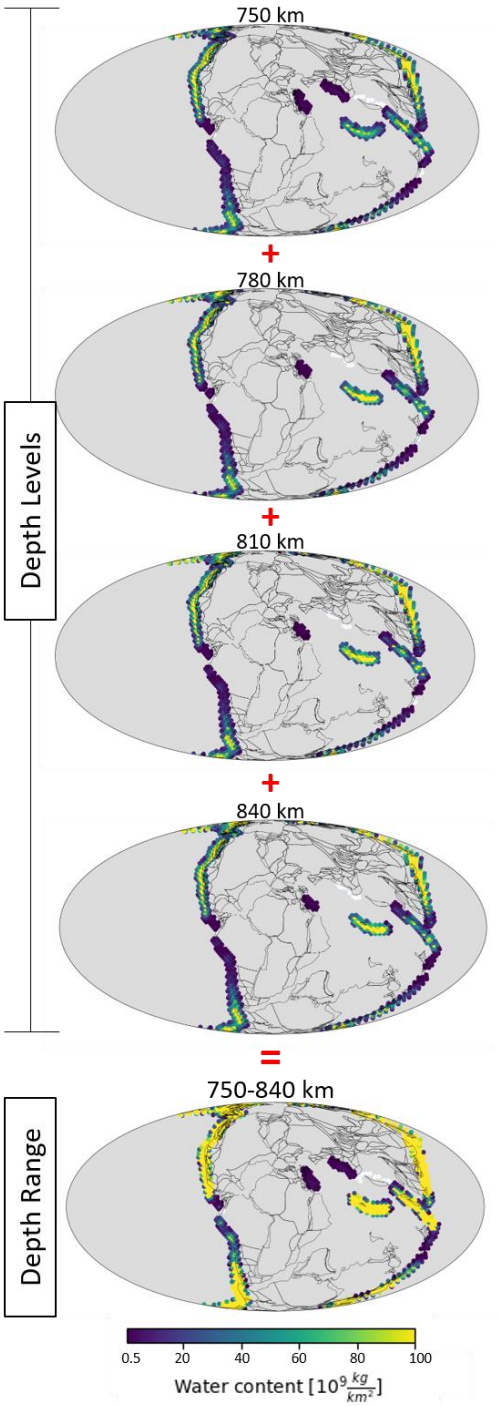


***Figure 6. From depth levels to a depth range**. The figure illustrates the process of adding water values stored in a mesh representative of different depth levels (750, 780, 810 and 840 km) to obtain a new mesh with the summed water values stored in the representative depth range (750-840 km). Hence, the depth range should subsequently be divided by the thickness of the layer, i.e., 90 km. The depth levels containing water are determined by the time the water initially subducted (here 125-128 Ma), the MTZ residence time (100 Myr) and the applied slab sinking rate. Here $v_{sink}$ = 3 cm/yr, causing water to descend 30 km per million years.*

The mesh point(s) closest to each segment midpoint were found using the nearest neighbor method (Figure 5; Fix & Hodges, 1951; Hackeling, 2017). After that, the water associated with the specific segment midpoint was added to the nearest mesh point(s) for each million year within the time of interest. This resulted in the mapping of the water flux into the mantle at a particular time, illustrated in Figure 4c-e for 0 Ma, 200 Ma, and 400 Ma, respectively. In turn, as the water was simulated to subduct to a deeper part of the mantle, the water flux map could be converted to represent the specific depth level. I here assume a vertical sinking, the implications of this will be further discussed. Summing the mesh over several depth levels yields a map of the water stored in the particular depth range (Figure 6). By using this method and dividing these values by the thickness of the layer (i.e., 250 km) I have determined the water distribution in the MTZ (410-660 km) for the various models of this study.

The lateral area into which water is assigned depends on the mesh density and at which depth the water is located within the Earth. This is because each mesh point represents a particular area of the globe, estimated to be approximately 50.000 km$^2$ at Earth's surface (Figure 5). The total number of points in the mesh (i.e., 10094) has been kept constant for all depths within the Earth. By calculating the surface area at a specific point of depth, based on the radius of the Earth minus the distance subducted, the area of a mesh point ($A$) could be established by dividing the surface area by the total number of mesh points. By dividing each mesh point water value by the

approximate area of a mesh point, the reduction in surface area with depth was accounted for. In addition, the individual mesh point water value was multiplied by the timestep. For a particular mesh point and subduction zone segment at a specific time and depth in the Earth, this can be expressed by

$$M = \frac{\mathrm{R}}{A}\Delta t\,,$$

( 4 )

where $M$, $R$, $A$, and $\Delta$t are the water mass per area [kg/km$^2$] assigned to a mesh point, the regassing flux of a segment [kg/year], the mesh point surface area [km$^2$] and the time step (i.e., 1 Myr, Table 1).

In deep mantle conditions, the water in the slab will likely migrate or diffuse to surrounding minerals, affecting the lateral reach of the subducting water. Even though water diffuses very slowly in mantle conditions, a saturated slab contains vast amounts of water that will travel great distances in the enclosed dry mantle given an infinite amount of time. However, there are significant uncertainties regarding how far the water will diffuse from slabs with a certain water content (Demouchy, 2010). In addition to diffusion, the location of the water will often deviate from the vertical point of subduction because of the slab dip, slab deformation, and partly by horizontal movement of stagnated slabs (Goes et al., 2017). To account for the lateral movement of hydrogen after subduction and uncertainties related to segment midpoint locations relative to the mesh points, the water is distributed to the $N$ closest neighbor mesh points (Figure 5). Consequently, the water will spread over a greater distance instead of only to the closest point. The amount of water added to each $k^{th}$ nearest neighbor mesh point has been weighted with the distance from the segment midpoint. If $d_k$ is the distance to the $k^{th}$ nearest neighbor mesh point and $N$ is the total number of nearest neighbors, $D$ can be expressed by $D = \sum_{k=1}^{N} \frac{1}{d_k}$. Modifying Equation ( 4 ),

$$M_k = \frac{R}{A}\Delta t\,\frac{\mathrm{D}}{d_k}\,,$$

( 5 )

we find an expression for the water mass per area assigned to a nearest neighbor mesh point. Thereby, the mesh point closest to the segment midpoint will receive most of the water. In contrast, the most distant neighbor will receive only a tiny fraction of the water associated with the segment midpoint in question (Figure 5).

Changing the total number of nearest neighbors *N* affects the overall lateral reach of the water and the amount of water added to each mesh point at a particular timestep. The mesh point closest to a specific segment midpoint, namely the 1st nearest neighbor, is on average approximately 85 km away from the segment midpoints at the surface with the mesh. Moreover, applying 10 and 30 nearest neighbors represents, on average, spreading the water to a reach of ~390 km and ~690 km from the segment midpoint, respectively. When applying different numbers of nearest neighbors, the mesh point water values in the MTZ over the past 250 Myr will therefore vary (Figure 7). The fewer nearest neighbors, the fewer the points with little water content and more points with substantial water content. When increasing the number of nearest neighbors, the water is more evenly distributed over the mesh, resulting in fewer points with abundant water content. However, the discrepancy between the three scenarios in Figure 7 is modest. In addition, the spreading of the water is closely related to the stagnation of slabs which has a much more significant impact on the water distribution in the MTZ and is consequently accounted for by other means as described in the subsequent paragraphs. Thus, to limit the number of variables in this study, 10 closest neighbors are hereafter applied to all models (Table 1). More essential variables are the slab sinking rate ($v_{sink}$) and the water residence time in the MTZ ($t_{MTZ}$).

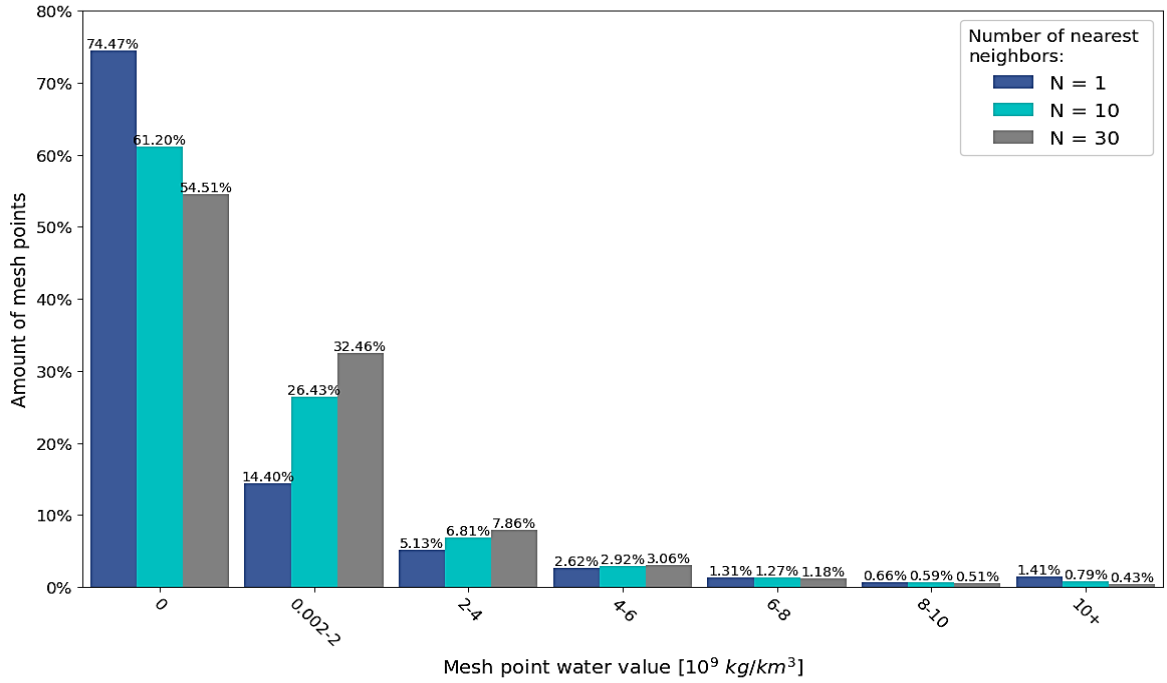


***Figure 7. Mesh point water values in the mantle transition zone over 250 Myr.*** *The percentage of mesh points with a specific water value defined by a range. This includes the water values for 10094 mesh points per timestep, each representative of the MTZ for each Myr the past 250 Myr. The different colors represent scenarios of varying number of nearest neighbors N, here 1, 10 and 30 nearest neighbors. The model applied has a MTZ residence time of 100 Myr and an averaged slab sinking rate of 3 cm/yr.*

The rate of descent for water-carrying slabs within the mantle is unknown and can vary among subducting plates and depths within the mantle. For modeling purposes, all subduction zone segments maintain a constant **slab sinking rate ($v_{sink}$)** in the subsequent models. However, the uncertainty regarding the sinking speed of the slabs has been accounted for by looking at several possibilities. Consequently, several models with differing $v_{sink}$ have been introduced during the mapping of the different scenarios of heterogeneous distributions of water to varying depths in the mantle. Subducting plate motions are primarily controlled by upper mantle (UM) slab pull, thereby, the $v_{sink}$ is mainly determined by slab buoyancy and shape, and mantle viscosities (Goes et al., 2011). Goes et al. (2011) finds that if a plate is pushed down faster than the Stokes' sinking rate, the slab will buckle and thicken, and if it's held back, the slab will thin or detach. An average sinking velocity of 1-4 cm/yr (van der Meer et al., 2018), 5-7 cm/yr (Goes et al., 2011), 10 cm/yr (Bercovici & Karato, 2003) and 1.5-6.0 cm/yr (Domeier et al., 2016) in the UM have been suggested to be reasonable rates. Hence, a slab sinking rate (applicable for the UM and MTZ) in the range of 1-9 cm/yr is adopted in this study (Table 1) and is used as an unknown parameter. When the slabs reach the 660 km discontinuity, there is often a change in the rate of descent (indeed global, whole mantle averaged sinking rates are in the order of 1.3 cm/yr (Butterworth et al., 2014). Thereby, it must also be considered that slabs often stagnate or slow down in the MTZ.

Some slabs appear to penetrate through the MTZ with the same angle and speed above and below the MTZ, whereas some slabs stagnate and slow down significantly (Figure 1; Goes et al., 2017). For scenarios of slab stagnation, a sinking rate of 0 cm/yr has been applied at the 660 km discontinuity for a selected number of million years ($t_{MTZ}$). It is unknown how long the slabs stagnate in the MTZ; therefore, several plausible scenarios are investigated; this includes a 0, 30, and 100 Myr **MTZ water residence time ($t_{MTZ}$)**, and an end member case where all the water accumulates in the MTZ from the beginning of the simulation ($t_{MTZ}=\infty$; Table 1). The residence time in the MTZ is not necessarily the time that the slabs stay in the MTZ before continuing to sink into the lower mantle. As the MTZ consists of wadsleyite and ringwoodite, which have significant water storage capacities (more detailed explanation in Section 1.3), some of or all the slab's water is possibly released during the stagnation. This would result in water staying in the MTZ even after the slab moves further into the mantle. Therefore, the case of accumulating water over an infinite amount of time in the MTZ is included.

## 2.3 Processing of the IPV dataset

In this thesis, I test for a correlation between continental intraplate volcanism (IPV) and water in the MTZ. The GEOROC (Geochemistry of Rocks of the Oceans and Continents) database (GROROC, 2021) contains information regarding IPV occurrences dating back to the Paleozoic. The obtained data includes onshore basalts classified as 'Intraplate Volcanism'. The present-day locations of these 5404 samples are displayed in Figure 8. The presented IPV in this map are dated to have erupted within the most recent 250 Myr. The obtained dataset does not include sites classified as ocean islands, as a majority of those sites might be related to mantle plumes. Nonetheless, some of the present-day active IPV points in the obtained dataset are related to plumes. However, these known points are not filtered out because other IPV points are likely caused by former plume-related eruptions where the plume-sourcing is not known. Thus, I used the database "as-is" (downloaded on November 16, 2021) to preserve consistency. In addition, oceanic intraplate volcanism has not been included as the geologic record is continually erased, hence the database is incomplete. The applied continental IPV dataset consists of the present-day maximum and minimum coordinates (either the extent or uncertainty in the location of the IPV sample), geologic era (time of eruption), and the minimum and maximum age of the erupted rock.

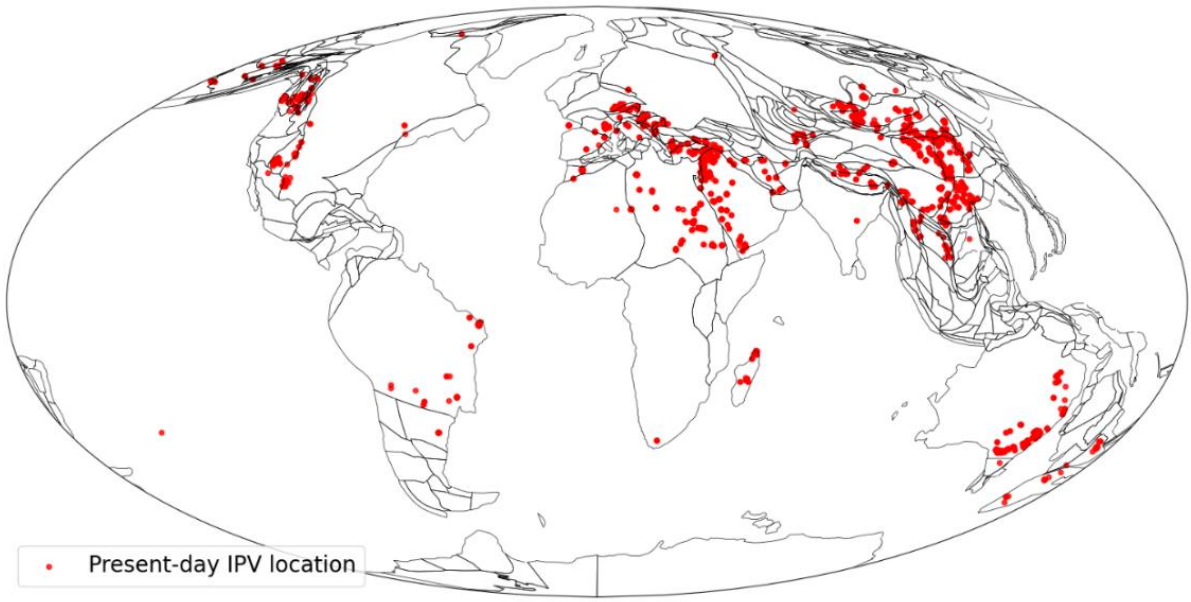


***Figure 8. 5404 intraplate volcanism locations at present-day**. The intraplate volcanism (IPV) samples displayed are defined as basalts from the GEOROC database (GROROC, 2021) and erupted within the past 250 Myr. The figure presents the present-day location of these samples, erupted locations can be applied based on a reconstruction of the continental polygons (e.g., Matthews et al., 2016). No filters are applied to the raw data displayed.*

As with many large geoscience databases, there are significant variations in the accuracy of the extracted IPV data. Some volcanic rocks have been dated with only a few million years or less uncertainty. Others are specified within a specific geological era, giving them an age range that spans over tens of million years. A more significant inaccuracy is generally presented back in time, i.e., more recent eruptions are more precisely dated. In the case of observations determined with both an era and an epoch and no specific age range, the shortest time interval has been set as the minimum and maximum age of eruption. In addition, if no minimum age is given or the minimum age is set to be older than the maximum age, the maximum age has been assigned. Likewise, only the minimum age has been kept if no maximum age is given. Though a temporal range has been considered, only one spatial location was desired for each IPV point in the dataset. Therefore, the minimum and maximum latitude and longitude average have been included in the following reconstructions.

The following functionalities were incorporated using the Python library pyGPlates (Williams et al., 2017), enabling access to the GPlates software (Boyden et al., 2011) via the Python programming language. GPlates is a plate tectonics program designed to generate reconstructions of geological and paleogeographic features through geological time (Müller et al., 2018). The outline encompassing the continental lithosphere remains roughly unaltered within the considered timeframe. However, their position on the Earth's surface changes over time due to seafloor spreading and subduction of the oceanic lithosphere. Hence, the coordinates of IPV today may not be the same as when they erupted. Therefore, when comparing IPV and the subducted water in the MTZ for the last 400 million years, the IPV location must reflect the location on Earth at the time of the eruption. To meet this criterion, the location of IPV must be relocated according to the tectonic reconstructions in accordance with the time of the eruption. Reconstruction models includes a rotation file, a plate boundary file, and a continent polygon file. Importantly, for consistency, these files were attained from the same plate tectonic reconstruction model (Matthews et al., 2016; Torsvik et al., 2019) applied to estimate the water flux to the mantle.

The continent polygon file contains static polygons representative of blocks of continental lithosphere which can be rotated back through time according to the rotation file. By assigning each IPV point to a continental polygon based on the present-day location, the reconstructed location of the eruptions could be established. Since all selected basaltic rock observations are intraplate, i.e., located within continents, they are confined within static polygons. However, the GEOROC dataset of IPV does include some points outside continental polygons (e.g., in the Pacific Ocean in Figure 8); these points have been filtered out. After assigning points to their representative plate (i.e., the PlateID), the IPV points are rotated, along with the continental polygons, back to their locations at the time of eruption. In addition, the age range of the IPV samples has been adjusted to fit within the polygon age range if their ranges are partially overlapping.

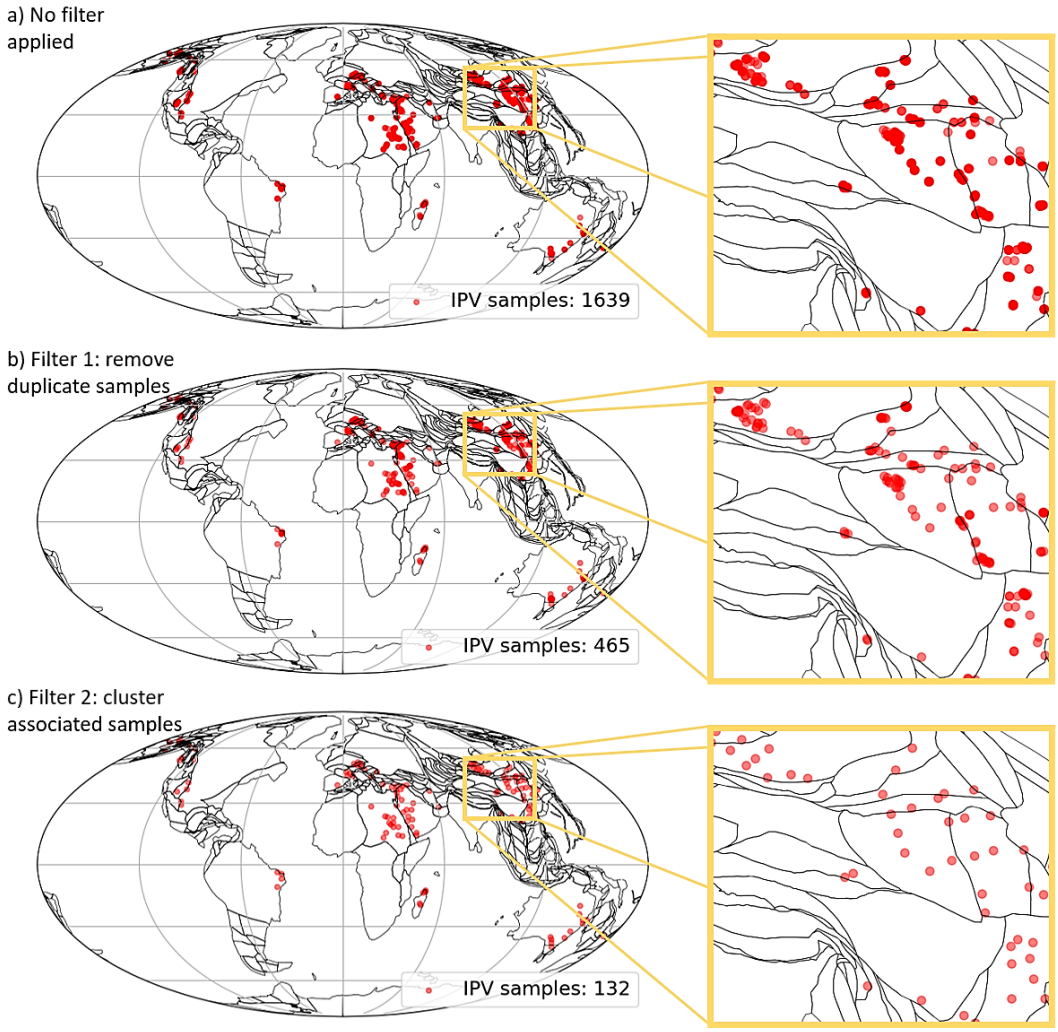


***Figure 9. Effect of filtering the active intraplate volcanism (IPV) samples at present-day (0 Ma).*** *All samples active at 0 Ma are displayed. Firstly, from the raw dataset (1639 samples, a), then the IPV data after filtering out duplicate points (465 samples, b), and thereafter samples of only individual observations (132 samples, c). Individual observations are referring to points that are not associated with the same volcanic event. The IPV data is obtained from the GEOROC database (GROROC, 2021).*

After reconstructing each IPV point to the location at the time of the eruption, 1639 active IPV samples (Figure 9a) as accessed from the GEOROC database (GROROC, 2021) are found at 0 Ma. However, the dataset has been further processed by applying two filters. Firstly, the obtained record of IPV includes 'duplicate' points; these are observations listed with the same longitude, latitude, and dating (often reflecting studies which generate multiple samples from similar site locations). Such overlapping points have been filtered out to prevent oversampling (Filter 1), leaving 465 active IPV points at 0 Ma (Figure 9b). Furthermore, IPV observations positioned in the near vicinity of each other (0-225 km radius) are likely associated with the same volcanic eruption. Where several IPV points were associated with the same mesh point, I merged the cluster into one single point, retaining the coordinates of the particular mesh point to reduce further oversampling (Filter 2). The above exclusions narrow the number of present-day active intraplate volcanic samples to 132 (Figure 9c). This filtering has been applied to each timestep in the considered time range, resulting in the number of IPV points at each timestep displayed in Figure 10. There tends to be a long period with the same number of IPV samples and then a leap in the number of samples. This is because several samples are defined with an age range, instead of the specific time of the eruption, especially with the increasing uncertainty back in time. In addition, more IPV data are available in more recent times as the geologic record is increasingly erased with time.

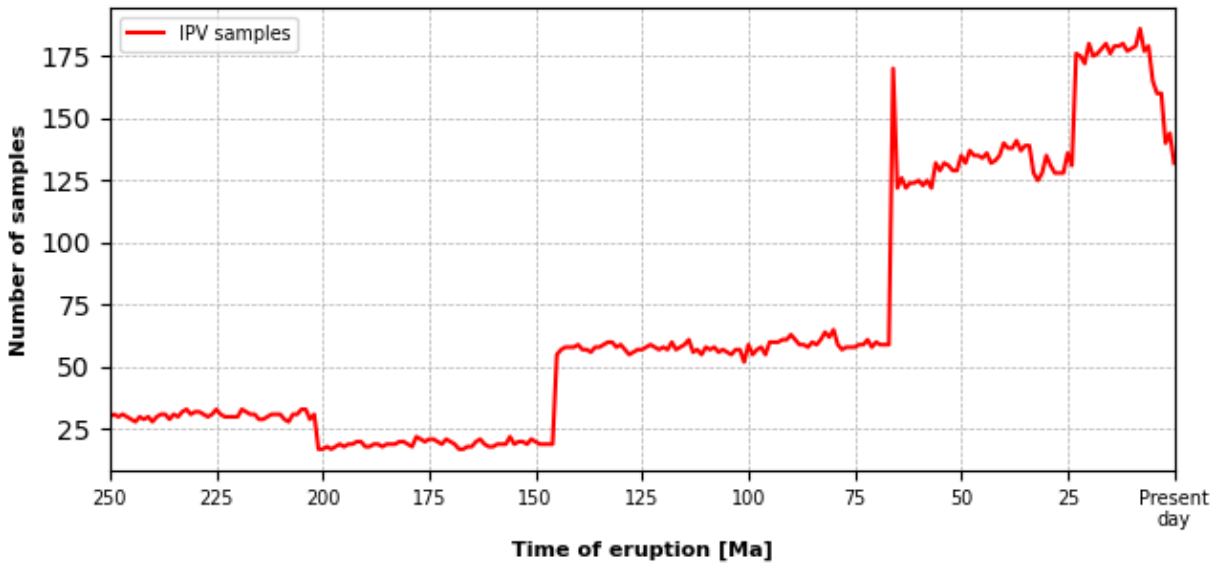


***Figure 10. Number of IPV samples****. The amount of intraplate volcanism (IPV) samples per million years after filtering (i.e., after removing duplicates and clustering associated points).*

## 2.4 Locations of active IPV and water in the MTZ

Several quantitative analyses have been performed throughout this study to investigate the possible connection between IPV and hydrated regions in the MTZ. The goal is to determine if there is, or has been, a considerable amount of water in the MTZ vertically below each IPV point at the moment (or the time interval) of eruption. Subsequently, if there has been water at some point, I can examine how long in the past and if there is an overall pattern for this time delay ($t_{IPV}$) between water in the MTZ and the associated intraplate eruptions. This highly depends on the time that the water is simulated to stay in the MTZ, i.e., the MTZ water residence time ($t_{MTZ}$). Consequently, it can be determined whether IPV can be used as a proxy to detect wet regions in the mantle.

Water-induced IPV is not necessarily coeval with the presence of water in the MTZ at the time of the eruption. There may be a **delay period ($t_{IPV}$)** between the arrival of water in the MTZ and the eruption of the volcanic rocks. This can possibly be controlled by the time it takes before melting initiates, which can be affected by the properties of the slab and the portion of the plate at which melting originates (Long et al., 2019). In addition to the mechanism behind the formation of hydrous melt (e.g., convective instability or slab interaction with a hydrous MTZ), the ascent period of the hydrous upwellings and the time it takes to penetrate the lithosphere could affect the timing of the eruption. Previous studies indicate IPV delay periods of ~12 Myr (Yang & Faccenda, 2020), 10-$10^6$ Myr (Motoki & Ballmer, 2015), and 10-30 Myr (Long et al., 2019). Thereby, $t_{IPV}$ of 10, 35, and 50 Myr are tested to assess this hypothesis (Table 1).

The reconstruction used in this study to investigate the water flux into the mantle extends 400 million years back in time. However, IPV from only the past 250 million years has been considered for the following reasons. Considering a shorter time range will reduce the overall uncertainty in the following results as greater uncertainties are generally presented further back in time. Additionally, in some of the scenarios explored, water has a $t_{MTZ}$ of one hundred million years. Thus, the MTZ will not have fully accumulated water for a hundred million years in the 300-400 Ma period since tectonic models with reconstructions from 400-500 Ma is not used, which is sensible as models from deeper time are even more poorly constrained. Likewise, additional time needs to be included for a potential $t_{IPV}$.

### 2.4.1 A wet or dry MTZ below active IPV?

The following modeling and calculations were conducted by applying a Pythonic interface for the Generic Mapping Tools (GMT, Wessel et al., 2019), namely PyGMT (Uieda et al., 2021). The PyGMT library was developed to process geophysical and geospatial data and create high-quality figures and maps. With the coordinates of the mesh and associated MTZ water values, a Delaunay triangulation was performed to set up a spherical interpolation in tension. These calculations were performed using the PyGMT class Sphinterpolate (Renka, 1997a, 1997b). By applying a Delaunay Triangulation, a discrete set of vertices is created such that no vertex lies inside the circumcircle of any triangle made from the mesh. This gives a triangular mesh, followed by an interpolation of the water values, resulting in a 1*x*1 degree global grid. The grid value below an IPV point represents the amount of water estimated to be located at that coordinate vertically within the MTZ.

Whether or not there is water at a particular point in the MTZ requires us to choose a threshold when comparing with the locations of volcanic eruptions at the surface, as tiny amounts of water might not create sufficient volumes of melt. This threshold has been set to $2 \cdot 10^6$ kg/km$^3$ (Table 1). Grid values above this limit are here considered as 'wet mantle transition zone', and values below $2 \cdot 10^6$ kg/km$^3$ are designated as 'dry'. It has been found that even small amounts of water can cause reduced viscosity and melting of mantle rocks (Drewitt et al., 2022; Hirschmann & Kohlstedt, 2012; Hirschmann, 2006; Luth, 2003; Wright, 2006). Hence, a low threshold is reasonable. This is especially true when considering that the amount of volcanism is not investigated; only the presence of continental basaltic eruptions is considered. In addition, due to this, along with the poor understanding of how much water is needed to create IPV and other factors controlling the formation of IPV, greater importance is not attributed to IPV occurrences above higher water values. To obtain manageable data regarding the incidence of intraplate volcanism eruptions over the wet MTZ, the grid value below each IPV point has been examined to see if the 'wet' threshold value has been met. The percentage of volcanic eruptions localized vertically above the wet MTZ was obtained for every million years in the considered time range (250-0 Ma). The percentage of such occurrences was then averaged over the past 250 million years. This was repeated for each of the various scenarios of this study (Table 1).

### 2.4.2 Random re-orientations of the hydrated MTZ grid

A statistical approach has been applied to investigate further the correlation between IPV and the heterogeneous distribution of hydrated regions in the MTZ. To quantify the significance of a measured difference between the observed result and a randomly obtained outcome, I preform a one-tailed hypothesis test with a 95% confidence level. I compute the p-value to investigate if the null-hypothesis is true, i.e., investigate if the observed result could be a chance occurrence. The p-value is a measure of the likeliness that a given observed value could have occurred by random chance. A small p-value, $\leq 0.05$, rejects the null-hypothesis and thereby yields a very low likeliness that the observed result is random. Hence, the smaller the p-value, the more statistically significant the results. The p-value is calculated from the probability density distribution for all values from the observed match percentage to the most significant one. The probability density is the fraction of instances that produce the same match percentage over all possible matches.

To develop a random set of comparisons from which to develop a distribution, the simulated MTZ water grid, as constructed for a given set of modeled parameters, has been randomly re-oriented on the Earth's surface 10.000 times (Figure 11). To clarify, the same re-orientation is applied to all time steps in the investigated period (i.e., 250 Myr), resulting in 251 MTZ water grids with the equivalent re-orientation; this is conducted 10.000 times. Consequently, for these random re-orientations, the configuration of the water in the MTZ is unrelated to the IPV locations, which are left in place. For each re-orientation, the MTZ grid values were compared to the IPV locations per million years, and averaged over 250 million years (that is, using the abovementioned method to determine the presence of water vertically below a point). As a result, the average percentage of points above water in the MTZ over 250 Myr was found for 10.000 random re-orientations and compared to the previously observed result. Note that the p-value is independent of the number of volcanism samples and is valid regardless of whether the sampling is complete or not (Conrad et al., 2011). This approach was applied to all scenarios of this study to determine if the observed correspondence is statistically significant.

There are multiple factors to consider when selecting the new orientations. Firstly, an entirely random orientation on the globe must be chosen based on a rotation pole consisting of longitude, latitude, and a rotation angle θ (Figure 11). To choose these values, a floating-point number between 0 and 1 was first selected using the Python module *random*. Secondly, since lines of longitude grow closer together moving toward the poles, fewer points had to be set at high latitudes than at low latitudes. A latitude value was selected from the distribution $90 - 2\left(\frac{180}{\pi}\right)\sin\left(\sqrt{x}\right)$, where $0 \leq x \leq 1$ and x are random floating-point numbers. Thirdly, an arbitrary rotation angle θ was required; the rotation had to be picked from a specific distribution to maintain randomness. A specific distribution serves to compensate for the fact that not all rotations are equally likely on a sphere. To ensure a random distribution of rotations, the approach of Miles (1965) has been applied. This provides a random pick of rotations from a uniform distribution of points on the surface of the Earth and rotation angles θ from the distribution $\frac{\theta - sin\theta}{\pi}$, where $0 \leq \theta \leq \pi$ (Conrad et al., 2010).

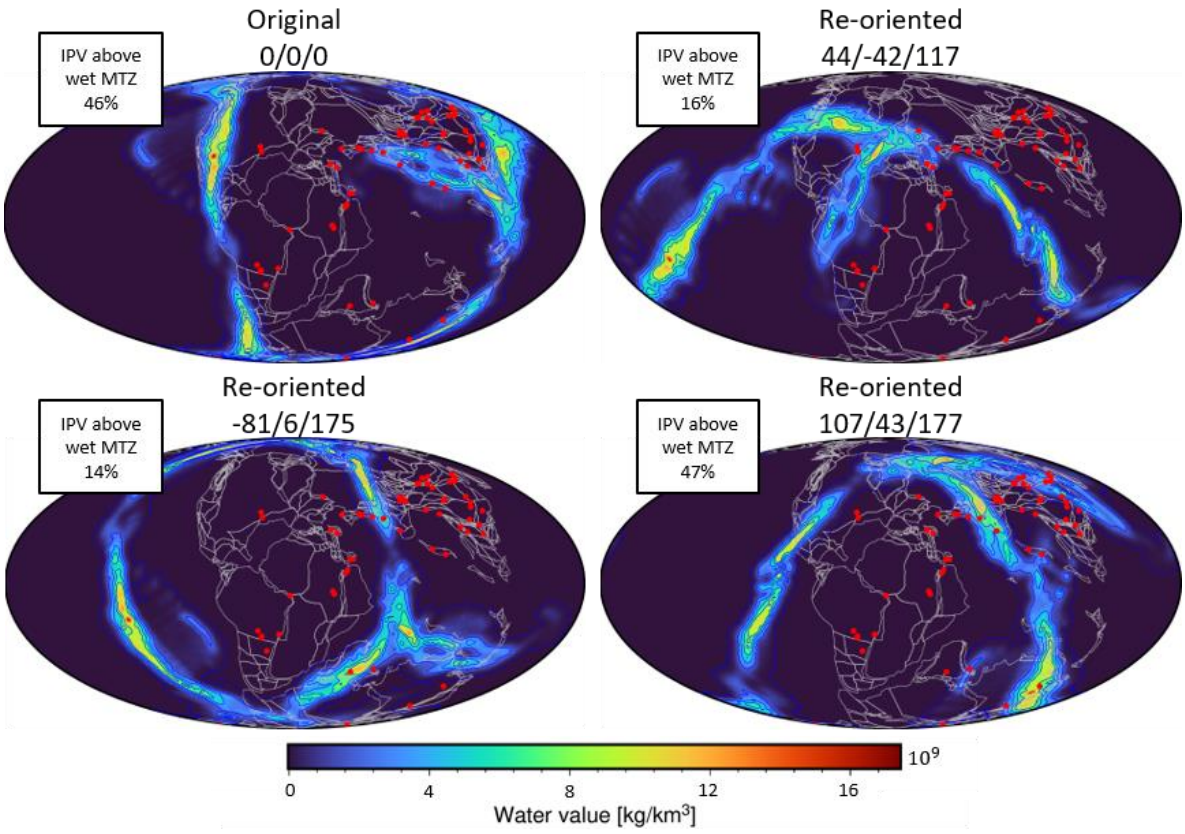


***Figure 11. Example of re-orientation of the MTZ water grid.*** *The illustration displays the mantle transition zone (MTZ) water grid at 125 Ma with a MTZ water residence time of 100 Myr, slab sinking rate of 3 cm/yr, and IPV delay period of 0 Myr, i.e., the reference scenario of this study. Various orientations of this grid defined by longitude/latitude/rotation (in degrees) is shown. Stationary intraplate volcanism (IPV) locations (red dots) and reconstructed coastlines (gray lines) are also displayed. The percentage of IPV samples above wet MTZ values (i.e., ≥2 ·10$^6$ kg/km$^3$) are listed in the inset.*

# 3. Results

The results of this thesis are presented through predictive maps of the mantle water content in the transition zone (410-660 km depth) at a particular time within the past 400 Myr. The predictive maps display multiple scenarios represented by various choices of model parameters and intraplate volcanism locations. Firstly, the reference scenario of this thesis is presented (Section 3.2.1), followed by the effect of varying the mantle transition zone water residence time (Section 3.2.2), the slab sinking rate (Section 3.2.3), and the effect of adding an IPV delay period between water at a specific point and an eruption vertically above this location when testing the agreement with locations of active IPV (Section 3.2.4). In addition, the results include graphs and tables that compare the predicted water content in the MTZ with IPV locations to determine whether IPV preferentially occurs above regions of hydrous MTZ. Finally, to test whether the incidence of IPV above regions of hydrated MTZ in the models is a chance occurrence, 10.000 random re-orientations of the predicted wet MTZ grid under unaltered IPV locations were conducted (Figure 11; elaborated in Section 2.4.2). This test has been applied to ten different scenarios for which the MTZ residence time $t_{MTZ}$, slab sinking rate $v_{sink}$, and IPV delay period $t_{IPV}$ have been changed (Table 1). Note that the figures display greater uncertainties the further they are traced back in time; this depends on the IPV data, the plate tectonic reconstruction model, and thereby the water grid data.

## 3.1 A heterogeneous mantle generated by subduction water influx

To investigate temporal changes in the water content retained by slabs at great depths (Figure 4a) and the global deep water flux (Figure 4b) during the past 400 Myr, I use a parameterization of the regassing fluxes per segment at a specific reconstruction age (Equation ( 2 )). The computed total regassing flux *R(t)* shows small fluctuations throughout the 400 Myr period, while several more distinct peaks occur over the observed interval. There is not a clear negative or positive trend, though the last 60 Myr yields the lowest global deep water flux over this time range (with an average value of $4.36 \cdot 10^{11}$ kg/yr). Indeed, it is here shown that the amount of water transported to the deep mantle through subduction has been notably more significant in the past than it is today. As expected, the amount of water reaching the deep mantle correlates well with the global mean water retention fraction (Figure 4a) and the global mean thermal parameter (Figure 2d). In addition, the regassing curve strongly reflects the subduction flux (i.e., $L_s \cdot v_{s,}$ Hounslow et al., 2018).

The slabs retain about 11-28% of their initial water content on a global average throughout the simulated period (Figure 4a). Model parameters (Table 1) were chosen to achieve the reasonable present-day regassing rate of $3.44 \cdot 10^{11}$ kg/yr (van Keken et al., 2011) and a global water retention fraction value of 0.14 (Karlsen et al., 2019). Based on these present-day values, an average global regassing rate over the past 400 Myr is computed to $7.0 \cdot 10^{11}$ kg/yr with a standard deviation of $2.4 \cdot 10^{11}$ kg/yr. Moreover, minimum and maximum regassing rates of $2.93 \cdot 10^{11}$ kg/yr at 58 Ma and $15.4 \cdot 10^{11}$ kg/yr at 128 Ma, respectively, are estimated. By attributing the subduction segment water fluxes to a particular area at each time increment (1 Myr), I find the distribution of water that subducts within the slab into the mantle (Figure 4c-e). The total water distribution (summed over various mantle depths, see Section 2.2 for details on the methodology) is presented in the subsequent section.

## 3.2 Water distribution and intraplate volcanism

To account for the poor constraints on essential factors that control the mantle's water distribution and mechanisms behind IPV production, I investigate the effect of different variables on the water distribution in the MTZ. These factors, described in Chapter 2, include the residence time of water in the MTZ ($t_{MTZ}$, Section 2.2), the slab sinking velocity ($v_{sink}$, Section 2.2), and a delay period ($t_{IPV}$, Section 2.4) between the time of arrival of the water in the MTZ and the eruption of IPV. Several different variables create the need for a reference scenario, here set to a 3 cm/yr slab sinking rate, a 100 Myr MTZ water residence time, and a 0 Myr IPV delay period. Firstly, the reference scenario of this study is presented. Thereafter, I investigate additional MTZ water residence times of 0, 30, and ∞ Myr with a 3 cm/yr slab sinking velocity. Following, I investigate the effect of altering the slab sinking rates to 1, 6, and 9 cm/yr with a MTZ residence time of 100 Myr. Finally, various IPV delay periods are added, this includes time delays of 10, 35, and 50 Myr for which eruptions occur after the presence of water in the MTZ, with the reference scenario MTZ water residence time (100 Myr) and slab sinking rate (3 cm/yr). I will investigate the amount of active IPV points above wet MTZ for the different scenarios listed above in the following subsections. Wet MTZ values are here set to $\geq 2 \cdot 10^6$ kg/km$^3$; values below this limit are designated as 'dry'. Henceforth, the instance of an IPV point located above wet MTZ is considered a 'match'.

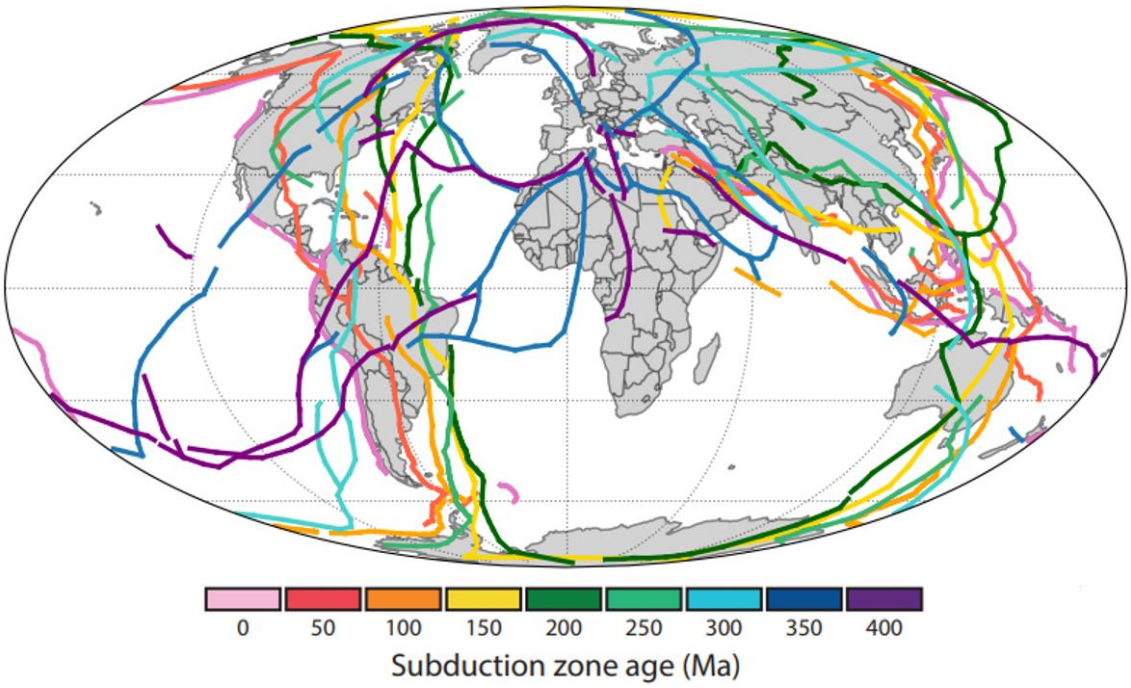


***Figure 12. Subduction zone locations for the past 400 million years.*** *The subduction zones are displayed with 50 Myr time increments (Matthews et al., 2016; Torsvik et al., 2019). A velocity filter has been applied to this data. In addition, present-day coastlines (light gray polygons) and geopolitical boundaries (dark gray lines) are displayed.*

### 3.2.1 The reference scenario

The mesh is used to store subduction water flux values through time and to calculate the location and extent of this water with depth. The location of water at depth largely depends on the location of subduction zones at earlier times depending on the depth and at which speed the water descends (Figure 12). The mapped water distribution of the upper mantle (UM, Figure 13a), mantle transition zone (MTZ, Figure 13b), and lower mantle (LM, Figure 13c) in the present Earth have been computed with this study's reference scenario parameters, which includes $t_{MTZ}$=100 Myr, $v_{sink}$=3 cm/yr and $t_{IPV}$=0 Myr. This is only one of many scenarios simulated in this study.

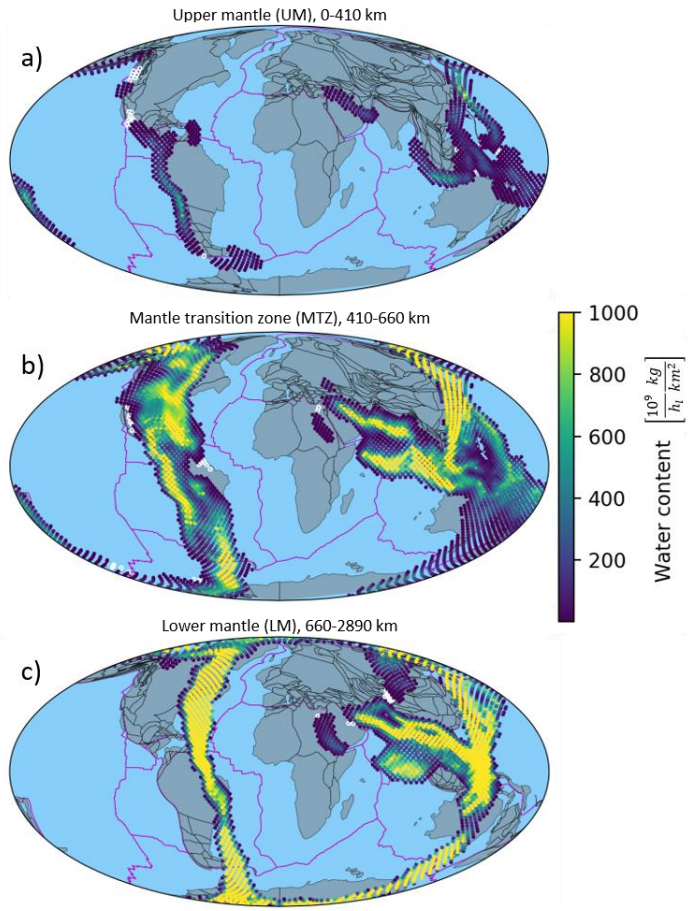


***Figure 13. Water distribution in the present-day mantle.*** *The water values for a model of the present Earth are depicted for the UM, MTZ, and LM in a), b) and c), respectively. The figure displays the water content of each depth range with the mesh (derived from CitcomS) applied in this study with present-day coastlines and plate boundaries. The scenario applied is the reference case of this study. White hollow points represent segments that did not transport water to the deep mantle, i.e., slabs that fully dehydrate during surface subduction. I chose not to plot grid points where no subduction occurred. The water values presented here are not divided by the layer thickness $h_l$ (e.g., 250 km for the MTZ).*

Expectedly, water contents in the UM are found close to present-day subduction zones (Figure 12; Figure 13a). The most hydrated region of the UM is beneath Eastern Asia, the western coast of South America, the Tonga and Java trench, and all along the Pacific Ring of Fire. The hydrated regions of the MTZ extend from Antarctica to the Arctic below South and North America (Figure 13b). Water-rich areas are also depicted below East Asia and India to the Middle East. Subduction brings significant amounts of water into the lower mantle below the eastern coast of South and North America (Figure 13c). In addition, hydrated areas extend from central Australia towards Northeast Asia and India towards the Middle East. A small, hydrated region can also be found below the Red Sea and the Afar Triple Junction, likely from the subduction of the Southern Neo-Tethys during Cretaceous time. It could also be observed that only a few areas linked to specific subduction zone segments do not contribute to the hydration of the deeper mantle (white circles in Figure 13). This includes subduction zone segments in North America and parts of Southeast Asia. I hereafter focus on the heterogeneous distribution of water in the mantle transition zone and its concurrence with continental intraplate volcanism.

The predicted water distribution in the MTZ at different times between 0-250 Ma, along with the locations of active IPV, is displayed in Figure 14. The water distribution extends over a much larger area of the globe at older times (200 Ma and 250 Ma) compared to younger times (0-100 Ma). However, at 50 Ma and 100 Ma, greater areas display significant water values ($\geq 4 \cdot 10^9$ kg/km$^3$) compared to past times; this includes areas in the MTZ beneath East Asia, America, and East Australia. Thereby, a greater regional extent does not necessarily signify a much greater total volume of subducted water in the MTZ. Many active IPV points are located above slightly hydrated regions in the present day (0 Ma; Figure 14a). Notably, relatively many of them appear within a confined area in Northeast Africa. Furthermore, a line of IPV locations is positioned along the edge of the hydrated region in Northwest America. IPV that is not above the hydrated parts at present-day is mainly located close to the edge of the MTZ water outline. Spreading the water further or having a greater MTZ water residence time would likely result in many of these points overlaying wet regions. Moreover, there are more locations of active IPV recorded in the database during more recent times (Figure 10); this could result in fewer matches, particularly since we know some are associated with mantle plumes. At 50 Ma (Figure 14b), many IPV points are parallel with the below field of highly hydrated MTZ beneath Australia. The 200 Ma and 250 Ma predictive maps (Figure 14e-f) yield a particularly good match between the mapped hydrous regions in the MTZ and IPV locations. This is especially true at 200 Ma, where most IPV points are above intensely hydrated regions in Eastern Asia. In fact, Eastern Asia is overlain by IPV at all times.

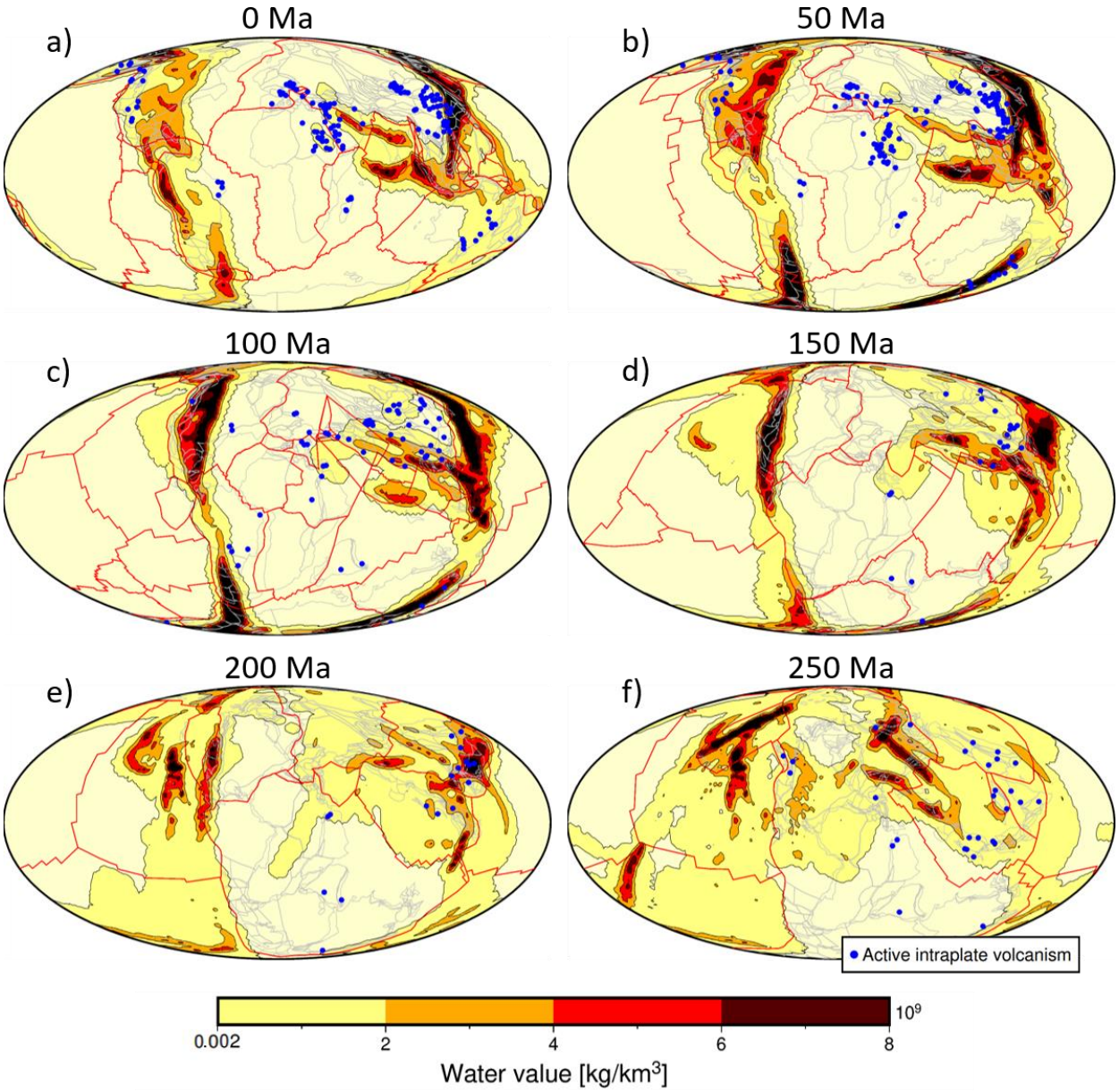


***Figure 14. Distribution of water for the reference scenario through time.*** *Predictions of the water distribution in the mantle transition zone (MTZ) and locations of active intraplate volcanism (IPV, blue points). The water is computed to have a 100 Myr residence time in the MTZ, a slab sinking velocity of 3 cm/yr, and no IPV delay period, i.e., the reference scenario of this study. The above global maps show the MTZ water distribution from the present-day to 250 Ma in 50 Myr time increments. In addition, the corresponding reconstructed coastlines (gray lines) and plate boundaries (red lines) are plotted.*

The amount of water in the mantle transition zone below locations of active intraplate volcanism varies significantly over time. The percentage of IPV locations that erupted in the past 250 Myr, located above a particular range of water values, is displayed in Figure 15 for the reference scenario. About half (46.53%) of all active IPV samples occur above dry regions throughout the 250 Myr considered. Most IPV occurs above hydrated regions with water values ranging between 0.002-2 $\cdot 10^9$ kg per km$^3$. Only a few intraplate volcanoes are located above areas with a large water content (i.e., greater than 4 $\cdot 10^9$ kg/km$^3$; Figure 15).

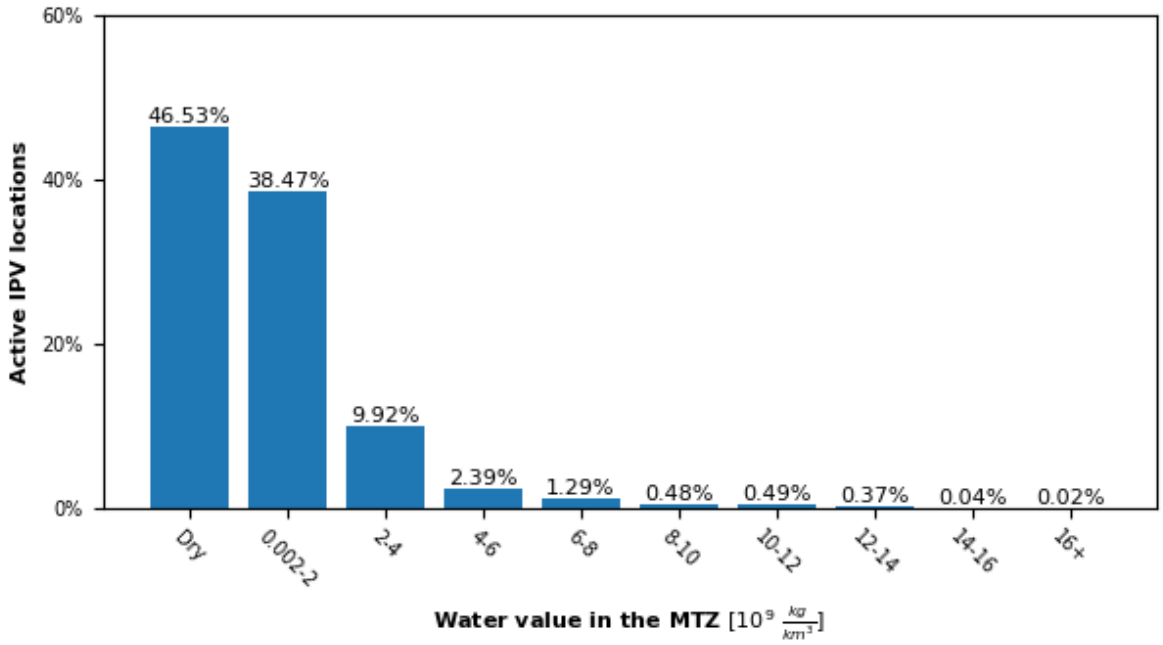


***Figure 15. Amount of water in the mantle transition zone (MTZ) below all active intraplate volcanism (IPV).*** *The bar plot displays the percentage of IPV points throughout the past 250 Myr that lie above a particular range of water values in the MTZ.*

The percentage of IPV over wet MTZ has been computed and averaged per million years over the past 250 Myr for the reference scenario (Figure 16). At present day, 46% of the 132 IPV samples overlie a wet MTZ. The percentage of IPV points above hydrated regions of the MTZ fluctuated between 40-60% over the past 125 Myr, while the area fraction of wet MTZ is about the same. However, the percentage of IPV samples above wet MTZ nearly doubles for older times, along with an increase in the area fraction of wet MTZ. There is a substantial increase in the wet MTZ and IPV location match percentage between ~125 Ma and ~150 Ma, while the extent of the hydrated regions in the MTZ increases steadily. In the reference scenario, throughout 0-250 Ma, an average of 64% of the IPV locations are above wet MTZ.

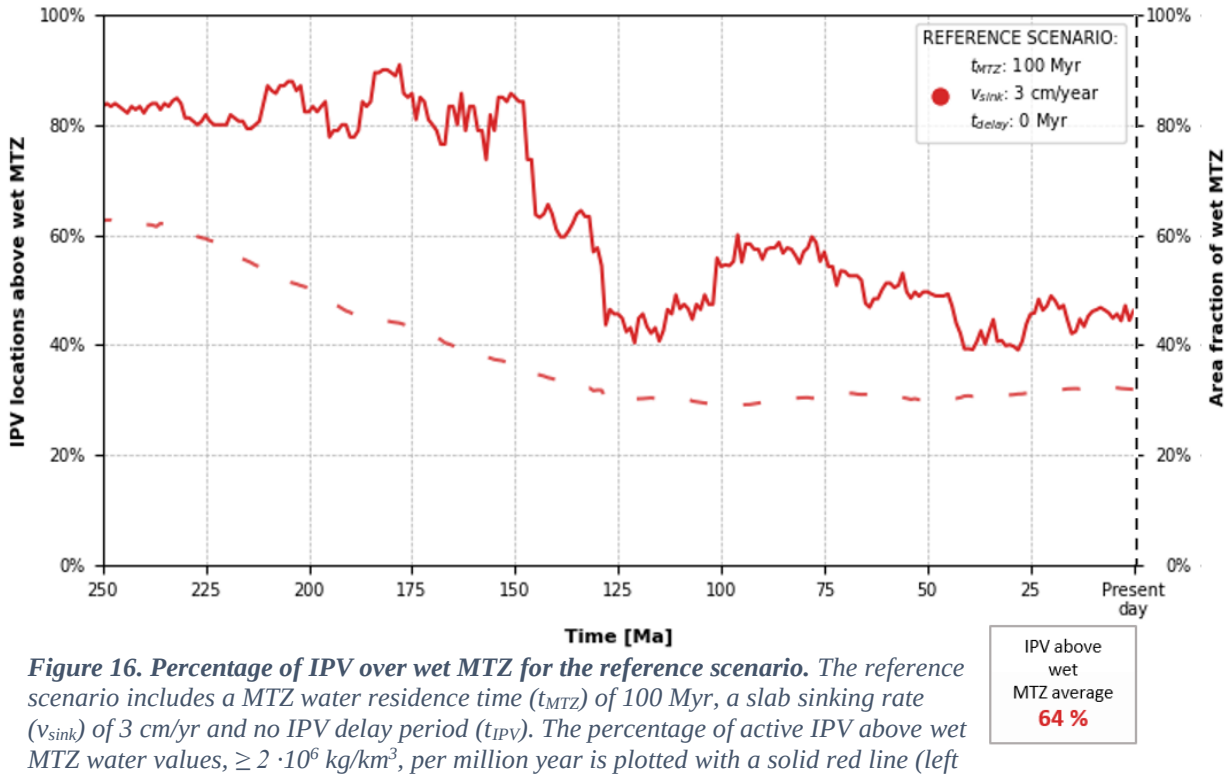


***Figure 16. Percentage of IPV over wet MTZ for the reference scenario.*** *The reference scenario includes a MTZ water residence time ($t_{MTZ}$) of 100 Myr, a slab sinking rate ($v_{sink}$) of 3 cm/yr and no IPV delay period ($t_{IPV}$). The percentage of active IPV above wet MTZ water values, $\geq 2 \cdot 10^6$ kg/km$^3$, per million year is plotted with a solid red line (left axis). In addition, the fraction of water grid area covered by hydrated (rather than dry) MTZ regions (dashed line, right axis).*

### 3.2.2 MTZ water residence time

I now investigate the effect of varying the MTZ water residence time, i.e., the time the water stays in the MTZ (Section 2.2). This could vary depending on the time the slab remains in the MTZ; a stagnating slab is expected to release more water in the MTZ than a slab that penetrates straight through. A longer $t_{MTZ}$ will result in a greater extent of hydrous regions and consequently a greater or unaltered correspondence with IPV. The water distribution in the MTZ for the reference scenario was presented in Figure 14; that is, a $t_{MTZ}$ of 100 Myr. A comparison of the effect of varying the MTZ residence time is shown at 0 Ma and 200 Ma in Figure 17 and Figure 18, respectively. Maps of the hydrated MTZ with a 0 Myr and 30 Myr residence time are displayed (Figure 17a-b; Figure 18a-b). In addition, one scenario for when all the water is accumulated in the MTZ from 400 Ma to the stated time (i.e., 0 Ma and 200 Ma, Figure 17d and Figure 18d, respectively). The amount of water in the MTZ increases with increased residence time; therefore, there are fewer IPV locations above hydrated regions with a shorter residence time. As mentioned in the previous subsection, many of the IPV points at present-day are adjacent to the hydrated regions in the MTZ (Figure 14a; Figure 17c). Thus, there is obviously a significant increase in the number of matches at present-day, associated with an increase in the MTZ water residence time (Figure 17).

Furthermore, we see a more considerable percentage of IPV locations above wet MTZ at 200 Ma for a 0, 30, and 100 Myr MTZ residence time (Figure 18a-c) compared to the present day with the equivalent scenarios (Figure 17a-c). However, I find a better agreement between IPV locations and the hydrated MTZ in Figure 17d (0 Ma) compared to Figure 18d (200 Ma) since, with an infinite MTZ water residence time, there is more water at 0 Ma than at 200 Ma. For this scenario of accumulating all subducted water in the MTZ from 400 Ma (Figure 17d; Figure 18d), the dry MTZ areas are, thus, regions that have not had any water contribution by subduction of oceanic plates between 400 Ma and the depicted time. At the same time, a relatively high water value signifies that there has been a significant water influx from overlaying subduction zones.

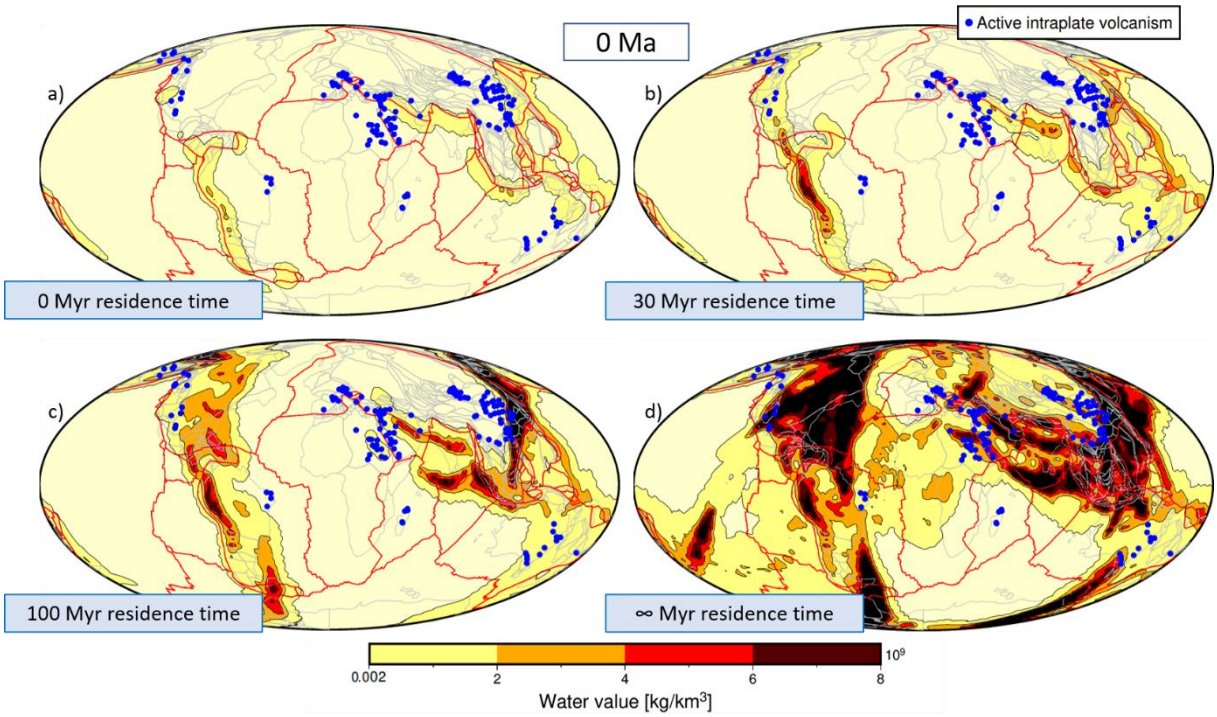


***Figure 17. Effect of varying MTZ water residence time, shown at 0 Ma.*** *Present-day predictions of the water distribution in the mantle transition zone (MTZ) with different MTZ water residence times and active intraplate volcanism (IPV) locations. The figure follows the same principles as Figure 14; in addition, c) reproduces Figure 14a. The slab sinking rate is 3 cm/yr, and no IPV delay period is added.*

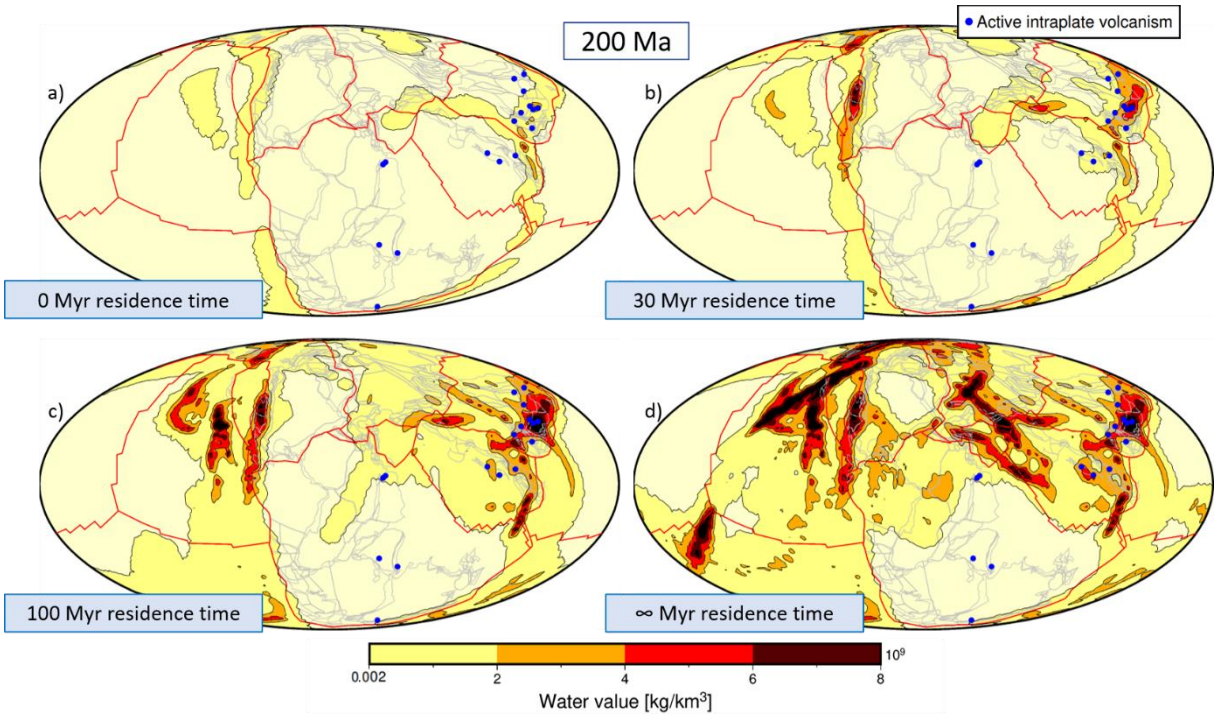


***Figure 18. Effect of varying MTZ water residence time, shown at 200 Ma.*** *Predictions of the water distribution in the mantle transition zone (MTZ) at 200 Ma with different MTZ water residence times and active intraplate volcanism (IPV) locations. The figure follows the same principles as Figure 14; in addition, c) reproduces Figure 14e. The slab sinking rate is 3 cm/yr, and no IPV delay period is added.*

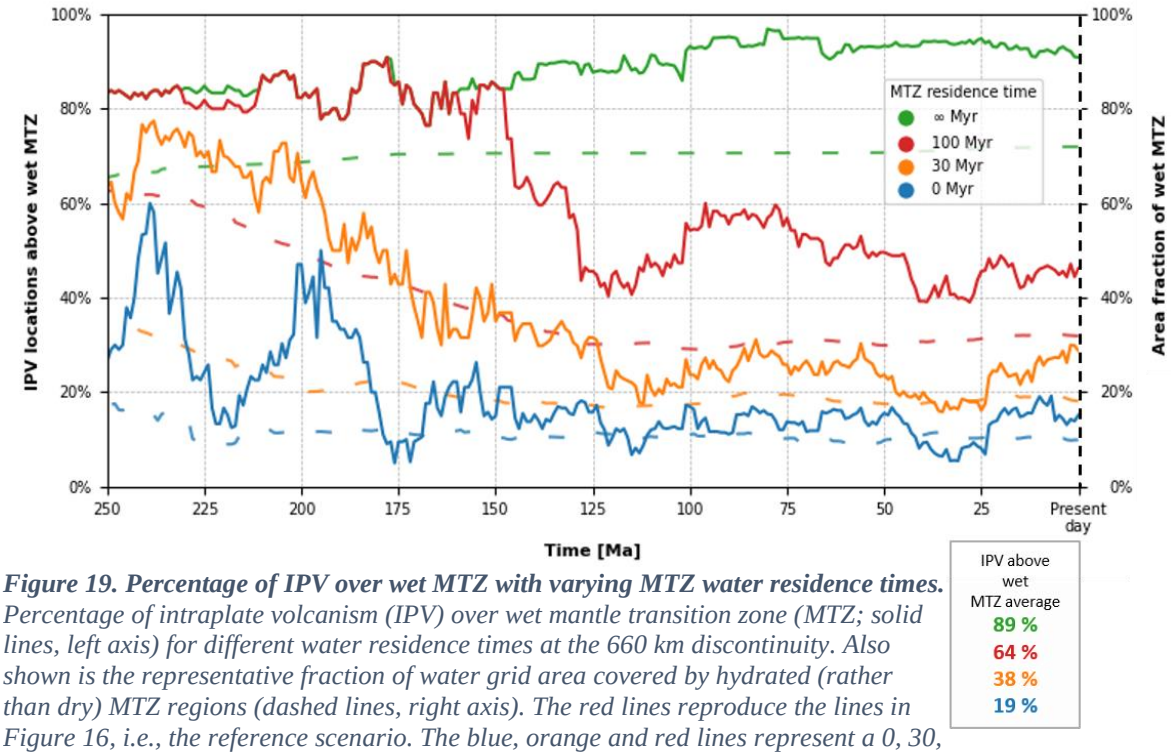


***Figure 19. Percentage of IPV over wet MTZ with varying MTZ water residence times.*** *Percentage of intraplate volcanism (IPV) over wet mantle transition zone (MTZ; solid lines, left axis) for different water residence times at the 660 km discontinuity. Also shown is the representative fraction of water grid area covered by hydrated (rather than dry) MTZ regions (dashed lines, right axis). The red lines reproduce the lines in Figure 16, i.e., the reference scenario. The blue, orange and red lines represent a 0, 30, and 100 Myr MTZ water residence time. With the green line, the water has accumulated in the MTZ since 400 Ma, i.e., a MTZ residence time of ∞ Myr. The slab sinking rate is 3 cm/yr and no IPV delay period is added.*

The average percentage of active IPV points above wet MTZ as a function of time throughout the past 250 Myr, for varying water residence times, largely follows the representative area fraction of the wet MTZ (Figure 19). The four different scenarios of 0, 30, 100, and ∞ Myr MTZ residence time deviate considerably, except for the 100 Myr and ∞ Myr scenarios from 250 Ma to ~150 Ma. As expected, for all four scenarios at all timesteps, a greater $t_{MTZ}$ results in a higher or equal percentage of IPV locations above hydrous MTZ. The graph shows a better agreement between IPV locations and wet MTZ further back in time for a 30 Myr and 100 Myr residence time. When there is no stagnation, i.e., the water sinks straight through the MTZ with the slab sinking rate (3 cm/yr), there are significant fluctuations in the percentage of matches between 250-170 Ma. For the same scenario, the past 170 Myr yield a steady match percentage just below or around 20%. When accumulating water in the MTZ from the start of the simulation (400 Ma), there is a positive trend in the occurrence of IPV above wet MTZ from 250 Ma to the present day. For every million years, more water subducts into the MTZ, but no water exits; hence, there is an increase in water content and extent. More substantial water distribution in the MTZ would naturally result in more IPV above hydrated regions.

### 3.2.3 Slab sinking rate

The rate at which slabs sink within the mantle is poorly constrained and varies between individual plates and regions of the mantle (Section 2.2). Here, the slab sinking rate controls the time it takes for the water subducted at the trench to reach the MTZ and, consequently, the time it takes for the water to sink through the MTZ. Hence, with a slow $v_{sink}$, the MTZ will contain water that was subducted at more timesteps than with a fast slab $v_{sink}$. Additionally, with a slower slab sinking rate, the water present in the MTZ will have subducted at older times compared to when applying a fast slab sinking rate. This will, in turn, affect the extent and amount of water in the MTZ. However, variation of the slab sinking rate does not result in strong changes to the predicted water distribution in the MTZ (Figure 20); although, there is slightly more water in the MTZ with a slower $v_{sink}$ at 0 Ma. When considering the full time range (Figure 21), a 1 cm/yr slab sinking rate results in a generally greater match between IPV and wet MTZ than in the other three scenarios, especially from 150 Ma to the present. While the area fraction of wet MTZ does not deviate much from the other scenarios from ~70-0 Ma. In addition, the match percentage is also not higher from 250 Ma to ~150 Ma even though the extent of wet regions is much greater. However, the area fraction of wet MTZ, and the percentage of IPV above wet MTZ, is both increased between ~150-70 Ma with a $v_{sink}$ of 1 cm/yr. Indeed, the average percentage of IPV occurrence above wet MTZ (71%) is the highest with a 1 cm/yr slab sinking rate. The other models show average values of 64%, 61%, and 60% for sinking rates of 3 cm/yr (reference model), 6 cm/yr, and 9 cm/yr, respectively.

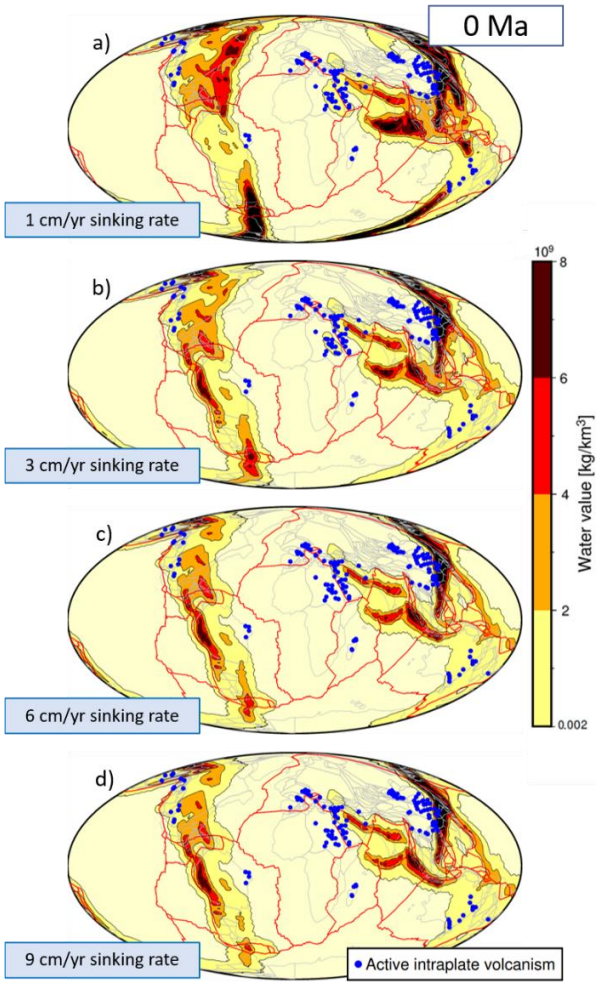


***Figure 20. Varying slab sinking rates at 0 Ma.*** *Predictions of the water distribution in the mantle transition zone (MTZ) at 0 Ma with slab sinking rates of 1, 3, 6 and 9 cm/yr, and active intraplate volcanism locations. The figure follows the same principles as Figure 14; in addition, b) reproduces Figure 14a. The MTZ residence time is 100 Myr and no IPV delay period is added.*

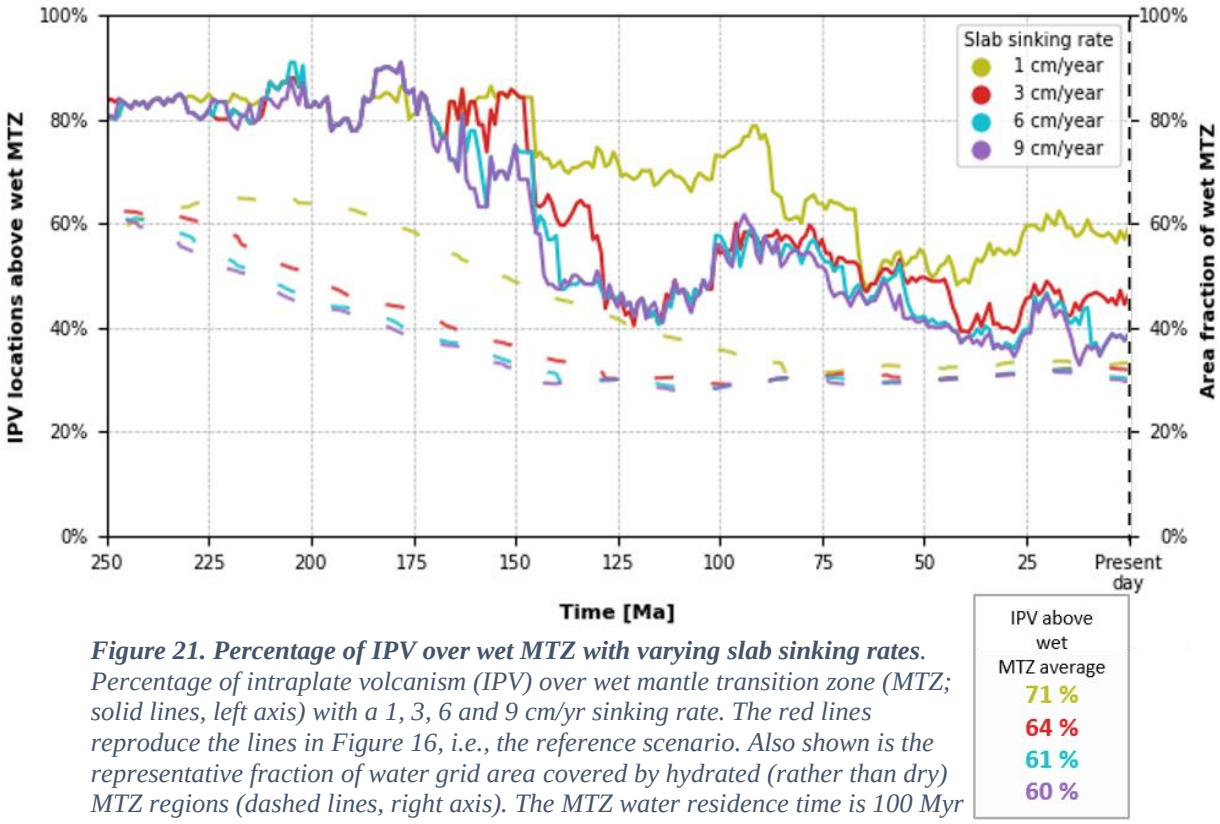


***Figure 21. Percentage of IPV over wet MTZ with varying slab sinking rates.*** *Percentage of intraplate volcanism (IPV) over wet mantle transition zone (MTZ; solid lines, left axis) with a 1, 3, 6 and 9 cm/yr sinking rate. The red lines reproduce the lines in Figure 16, i.e., the reference scenario. Also shown is the representative fraction of water grid area covered by hydrated (rather than dry) MTZ regions (dashed lines, right axis). The MTZ water residence time is 100 Myr and no IPV delay period is added.*

### 3.2.4 IPV delay period

There might be a delay period between the presence of water in the MTZ and the eruption of IPV (Section 2.4). A delay period would be reasonable since processes such as MTZ hydration, melt production, the ascent of hydrous melt, and its percolation through the lithosphere do not occur instantaneously. The IPV delay period does not significantly affect the correspondence between MTZ water and IPV eruptions (Figure 22). Adding a delay results in a similar increase in the area extent of hydrous regions to that of the 1 cm/yr slab sinking rate model (Figure 21, Section 3.2.3). Different scenarios have the highest percentage of IPV and wet MTZ matches at different times (i.e., the lines cross in Figure 22), but the averages are overall similar; 64% for 0 Myr delay time (reference model), 66% for 10 Myr, 69% for 35 Myr, and 68% for 50 Myr. A longer $t_{IPV}$ results in more IPV points above wet MTZ from 150 Ma to the present, compared to when a delay is not considered (red line). A 50 Myr delay period yields a great number of matches for the same period. However, I find a poorer match percentage further back in time and a strong negative trend from 200-250 Ma. On the other hand, a $t_{IPV}$ of 10 Myr shows similar trends to the reference scenario. Moreover, from 250-150 Ma, a 10 Myr delay period barely impacts the results compared to the reference case. The highest overall average percentage arises from a 35 Myr IPV delay period, with 69%.

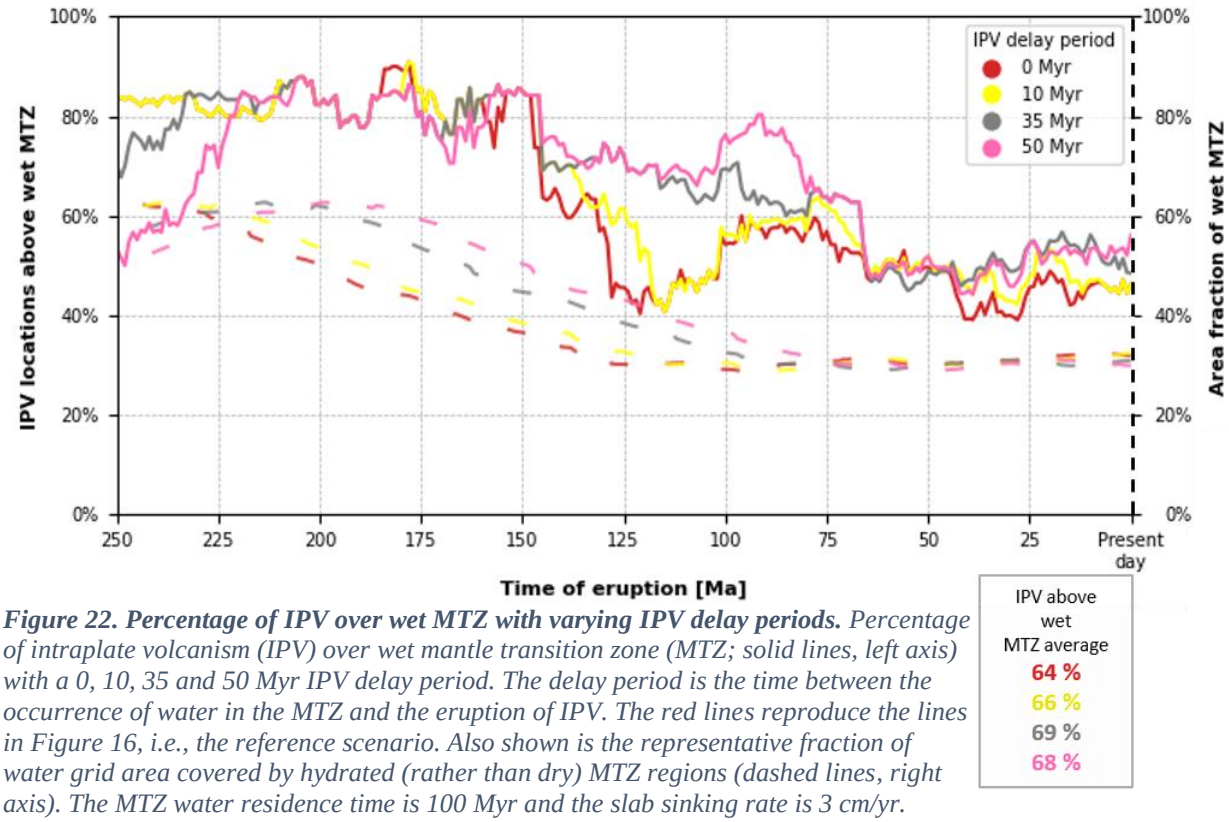


***Figure 22. Percentage of IPV over wet MTZ with varying IPV delay periods.*** *Percentage of intraplate volcanism (IPV) over wet mantle transition zone (MTZ; solid lines, left axis) with a 0, 10, 35 and 50 Myr IPV delay period. The delay period is the time between the occurrence of water in the MTZ and the eruption of IPV. The red lines reproduce the lines in Figure 16, i.e., the reference scenario. Also shown is the representative fraction of water grid area covered by hydrated (rather than dry) MTZ regions (dashed lines, right axis). The MTZ water residence time is 100 Myr and the slab sinking rate is 3 cm/yr.*

## 3.3 Mantle transition zone water content

The amount of water in the MTZ is vigorously debated in the science community (Bolfan-Casanova et al., 2006; Inoue et al., 2010; Wang et al., 2019); some find the MTZ to be dry (Yoshino et al., 2008), while others estimate the MTZ reservoir to be nearly water-saturated (i.e., ~2-3 times the ocean mass, OM = $1.4 \cdot 10^{21}$ kg, Fei et al., 2017; Ohtani, 2005). The various scenarios of this study yield varying amounts of water attributed to the MTZ by subducting slabs at different times (Table 2). I find values ranging from 0.3% to 20% of the present-day OM. For all scenarios, except with $t_{MTZ}=\infty$ Myr or $v_{sink}=1$ cm/yr, the amount of water in the MTZ was more significant at 100 Ma and 250 Ma than at 0 Ma. In addition, there was generally more water in the MTZ at 100 Ma than at 250 Ma. I find that the MTZ water content was much greater between ~100-25 Ma compared to ~250-150 Ma with the reference scenario. With $t_{MTZ}=\infty$ Myr, the MTZ water content increases with time from 400 Ma to the present, as expected (no water is transported out of the MTZ). However, it is essential to note that the amount of water allocated to the MTZ at a particular time depends on the regassing rate applied in this study, i.e., $3.4 \cdot 10^{11}$ kg/yr (van Keken et al., 2011). In addition, this is a measure of the water subducted to the deep mantle within the past 400 Myr; the MTZ could possibly contain far more water (as the MTZ likely contained water prior to 400 Ma). Notably, with the regassing rate of this study and an infinite $t_{MTZ}$, I here find that 1/5 of the surface ocean mass could be attributed to the MTZ within 400 Myr.

***Table 2. Amount of water in the Earth's mantle transition zone (MTZ) at 0 Ma, 100 Ma, and 250 Ma with the various scenarios of this study.*** *The amount is specified in the percentage of the present-day ocean masses, i.e., OM=$1.4 \cdot 10^{21}$ kg. The values originating from the reference scenario are in bold.*

| MTZ residence time [Myr] | Slab sinking rate [cm/year] | MTZ water content at 0 Ma [OM] | MTZ water content at 100 Ma [OM] | MTZ water content at 250 Ma [OM] |
|---|---|---|---|---|
| 0 | 3 | 0.3% | 0.6% | 0.4% |
| 30 | 3 | 1.3% | 3.1% | 1.7% |
| **100** | **3** | **4.7%** | **6.3%** | **5.7%** |
| 400 | 3 | 20.0% | 15.6% | 7.4% |
| 100 | 1 | 6.9% | 6.1% | 6.2% |
| 100 | 6 | 4.1% | 6.3% | 5.3% |
| 100 | 9 | 3.9% | 6.2% | 5.1% |

## 3.4 Statistical significance of the observed results

The correspondence between hydrous MTZ and IPV locations varies significantly for the different scenarios presented in this study. A longer water residence time results in a higher percentage of IPV above wet MTZ, slower slab sinking rates display a better agreement, and an increased IPV delay period yields a slightly higher match percentage. The different scenarios offer an average match over the 0-250 Ma period of 19-89% (Table 3), where the reference scenario yields a 64% match. When varying the MTZ water residence time to 0 Myr, 30 Myr, and ∞ Myr, the greatest spread is found in the percentage of matches, with 19%, 38%, and 89%, respectively. Although there is not a markedly visible difference between the water distributions in the MTZ at 0 Ma (Figure 20), it is nevertheless found an 11% greater correspondence with a 1 cm/yr slab sinking rate than with a 9 cm/yr rate over the 250 Myr period (Figure 21). The deviations are slight for the different scenarios of varying delay periods, where I find a 66%, 69%, and 68% match between the hydrated regions of the MTZ and locations of active IPV with a 10, 35, and 50 Myr IPV delay period, respectively.

However, a more significant correspondence between IPV locations and the predictions of wet MTZ, i.e., a greater percentage, does not necessarily signify that the specific values of the models with the highest match are more plausible than those of other models. The above-observed results could possibly be arbitrary. It must be determined if the positive correspondence has a statistically significant meaning. This depends on the overall coverage of the MTZ water grid and the distribution of the IPV locations. Hence, MTZ water grid re-orientations below stationary IPV locations have been conducted to test if the observed results are statistically significant. Finding the percentage of IPV locations above wet MTZ with 10.000 randomly rotated water grids can determine the p-value from the probability density distribution (more detailed explanation in Section 2.4.2). A small p-value, $\leq 0.05$, suggests that the observed result presented in Section 3.2 has a statistically significant meaning. Accordingly, it can be determined if the above-observed percentages are likely to reflect a meaningful relationship between hydrous MTZ regions and IPV occurrence.

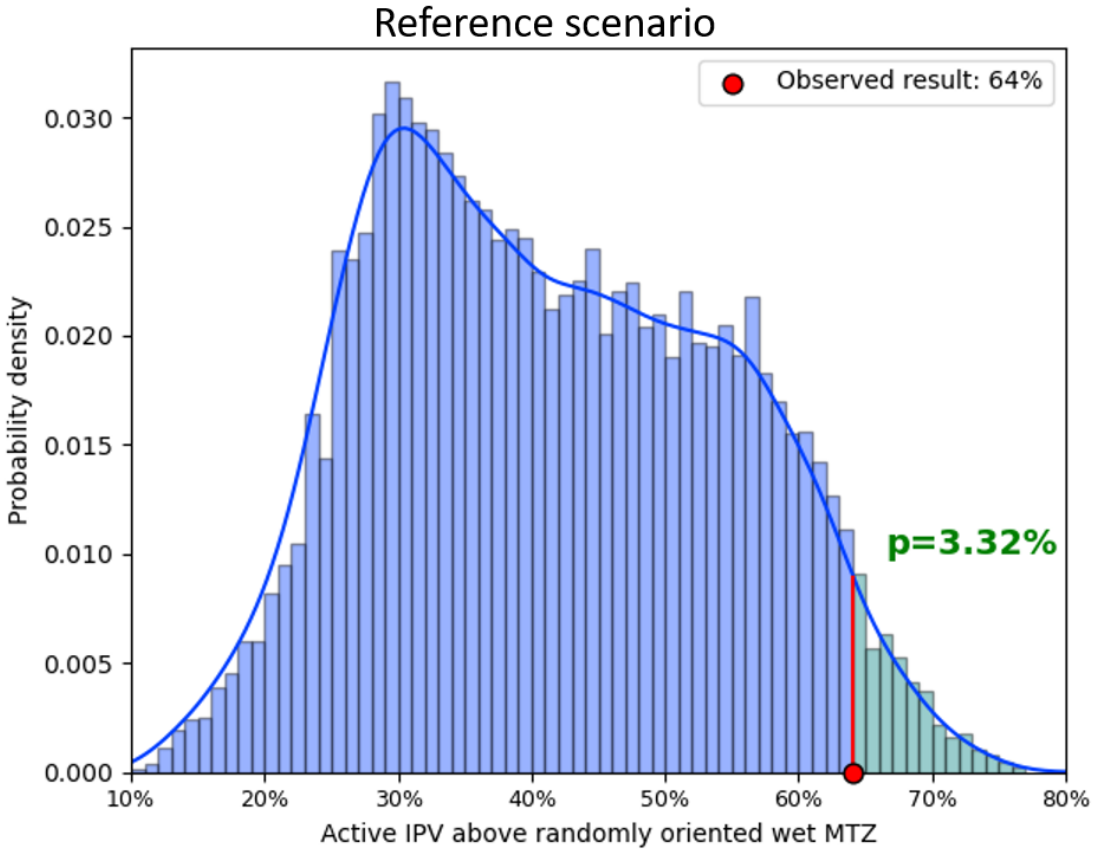


***Figure 23. The probability density for the reference scenario***. *The probability density distribution for the concurrence between stationary IPV locations and 10.000 re-orientations of the MTZ water grid (blue and green bars) and fitted probability density curve (blue line) is displayed. The area of the bars (green) with an improved fit compared to the observed result without re-orientation (red, 64%) represent 3.32%, yielding a p-value of 0.0332. The reference scenario includes a MTZ water residence time ($t_{MTZ}$) of 100 Myr, a slab sinking rate ($v_{sink}$) of 3 cm/yr, and no IPV delay period ($t_{IPV}$).*

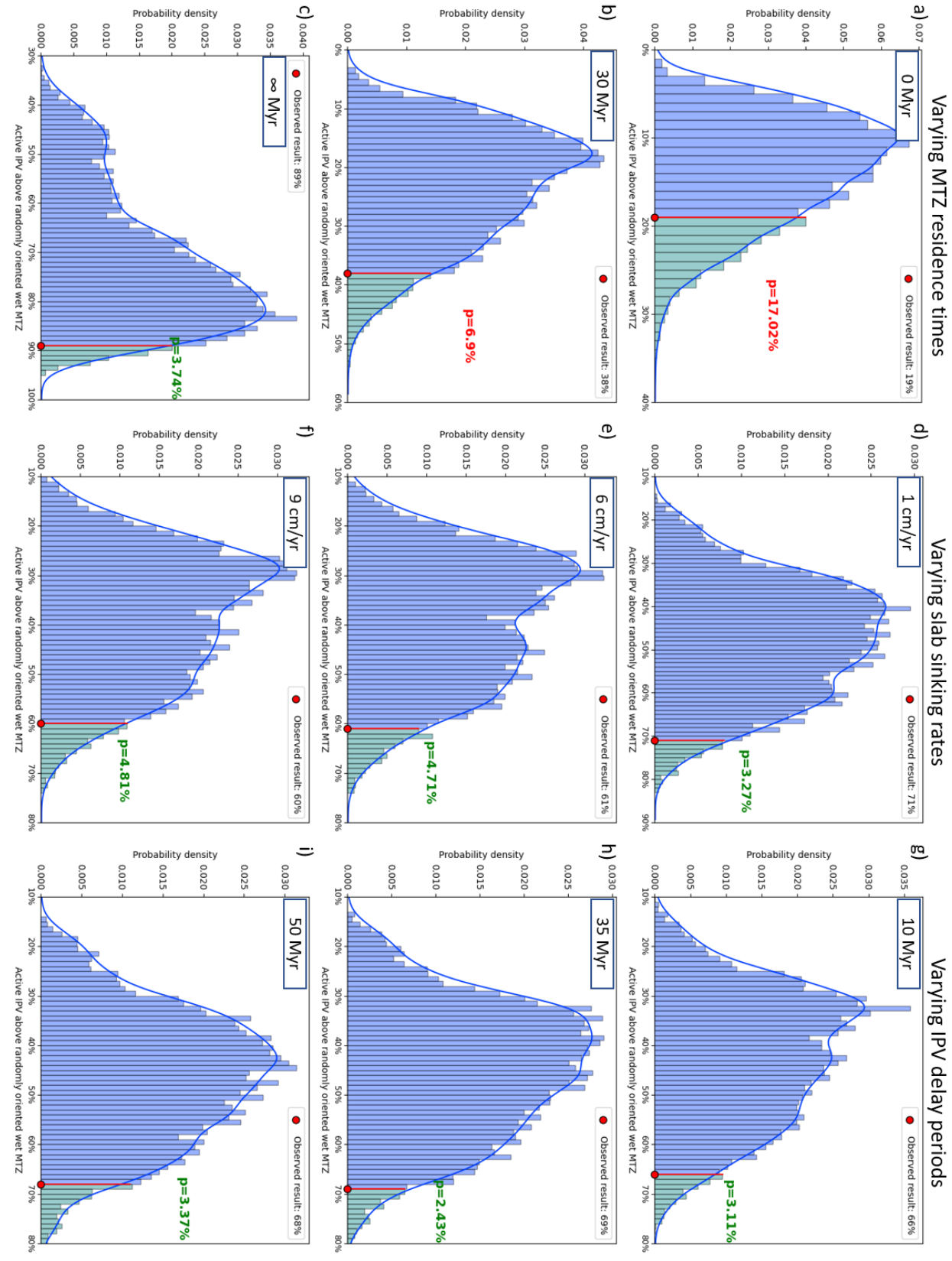


***Figure 24. Probability density for the various models of this study.*** *The scenarios include varying the mantle transition zone (MTZ) water residence time (left), varying the slab sinking rate (middle) and varying the intraplate volcanism (IPV) delay period (right). The figure follows the same principles as Figure 23.*

The p-value found from rotating the MTZ water grid beneath stationary IPV locations indicates whether a specific scenario of predicted MTZ water distribution yields a statistically significant correlation with IPV locations (Figure 23; Figure 24) or, more specifically, if the observed match between the hydrous areas and the eruption of IPV could have occurred by random chance. Small p-values, $\leq 0.05$, yield a very low likeliness that the observed result is a chance occurrence (Figure 23; Figure 24c-i), while for larger p-values, it cannot be determined a statistical significance with a 95% confidence limit (Figure 24a-b). There is a 64% correspondence between IPV locations and the wet MTZ grid for the reference scenario; with respect to the statistical test, only 3.32% of the 10.000 randomly re-oriented alternative comparisons yielded a result as extreme as the observed match between IPV and wet MTZ (64%; Figure 23). Thus, we can reject the null-hypothesis that the observed correspondence between IPV and wet MTZ is a chance occurrence at the 95% confidence level. The same applies to the infinite million years MTZ residence time scenario, where I find an agreement of 89% between hydrous MTZ regions and locations of IPV. While with a 38% match and 19% match, resulting from a MTZ water residence time of 30 Myr and 0 Myr, respectively, I find a worse p-value (6.90% and 17.02%, respectively, Table 3), and thus we cannot reject the null-hypothesis at the 95% confidence level. Compared to the reference scenario (p=3.32%), a nearly identical statistical significance (p=3.27%) is found for the scenario with a 1 cm/yr slab sinking rate (with a 71% match). While with a 35 Myr IPV delay period (69% match) we can reject the null-hypothesis at the 97% confidence level (p=2.43%). Results from this test show a statistically significance in all scenarios with a 100 Myr and $\infty$ Myr MTZ residence time (Table 3). These statistical tests indicate that the prevalence of IPV above a hydrated MTZ is unlikely to be a chance occurrence. Thus, there exists a meaningful link between the occurrence of IPV and hydrated regions of the MTZ.

***Table 3. Statistical significance of various scenarios.*** *Different variables that define the 10 models of this study, the match between intraplate volcanism (IPV) locations and mantle transition zone (MTZ) water extent, and the subsequent p-value computed using 10.000 random re-orientations (with statistically significant cases for which p≤0.05 shown in green). The values originating from the reference scenario are in bold.*

| IPV delay period [Myr] | MTZ water residence time [Myr] | Slab sinking rate [cm/year] | IPV locations positioned above wet MTZ averaged over 250 Myr [%] | p-value |
|---|---|---|---|---|
| 0 | 0 | 3 | 19 % | 0.1702 |
| 0 | 30 | 3 | 38 % | 0.0690 |
| **0** | **100** | **3** | **64 %** | **0.0332** |
| 0 | ∞ | 3 | 89 % | 0.0374 |
| 0 | 100 | 1 | 71 % | 0.0327 |
| 0 | 100 | 6 | 61 % | 0.0471 |
| 0 | 100 | 9 | 60 % | 0.0481 |
| 10 | 100 | 3 | 66 % | 0.0311 |
| 35 | 100 | 3 | 69 % | 0.0243 |
| 50 | 100 | 3 | 68 % | 0.0337 |

# 4. Discussion

I have used estimates of rates and volumes of water transport into the deep mantle from modeled subduction fluxes to quantify the spatial heterogeneity of water in the mantle through state-of-the-art plate tectonic reconstructions. Despite uncertainties affiliated with the reconstructions and the mechanisms controlling the heterogeneous distribution of subducted water, I find a statistically significant correlation between the mapped hydrous regions of the MTZ and locations of intraplate volcanism. Models with a statistical significance above the 95% confidence level display a match with IPV between 60-89%. These statistical tests indicate that the prevalence of IPV above hydrated MTZ is unlikely to be a chance occurrence, which implies a link between the occurrence of IPV and hydrated regions of the MTZ, confirming the hypothesis of this thesis.

Multiple models governed by different variables controlling the distribution of subducted water in the MTZ have been presented (Chapter 3). The models' performance in simulating the water distribution in the MTZ differs greatly depending on MTZ water residence times ($t_{MTZ;}$ described in Section 2.2). In comparison, the effect of altering the slab sinking rate ($v_{sink}$; described in Section 2.2) is slight. Remarkably, a p-value $\leq 0.05$ (indicating that the prevalence of IPV above regions of hydrated MTZ is unlikely to be a chance occurrence) is determined for all models with a 100 Myr MTZ water residence time, along with IPV match percentages between 60-71% (Table 3). In addition, I find a statistically significant correlation for the model with an $\infty$ Myr MTZ water residence time, which yields a striking 89% agreement with IPV locations. This suggests that the temporal stagnation of slabs at the 660 km discontinuity is a crucial part of the process that leads to IPV. Nonetheless, not all slabs behave in such a manner (i.e., it is shown through seismic tomography that some slabs penetrate through the MTZ), though the stagnation or stall in the MTZ has great significance for this process. This delay could result from dehydration and re-hydration reactions in the slab and the MTZ, respectively, both being slow processes. Alternatively, a long MTZ residence time might be needed for a slab to first hydrate the MTZ, after which a new slab or mantle convection must further hydrate or mobilize, respectively, the originally hydrated mantle material.

With a shorter MTZ water residence time of 0 Myr or 30 Myr, I cannot determine a statistical significance by rejecting the null-hypothesis at the 95% confidence level from the observed percentage of IPV above wet MTZ (19% and 38%, respectively). In these scenarios, the coverage of the hydrous regions in the MTZ is likely not great enough to explain the IPV. Furthermore, when applying a 35 Myr IPV delay period (explained in Section 2.4), I find a greater match (69%) and a statistically significant correlation ($p=0.0243$), supporting the likelihood of a significant delay between the arrival of water in the MTZ and subsequent eruption of IPV. The predicted distributions of water in the MTZ, and their concurrence with IPV locations, will be further discussed in this chapter. In addition, I will discuss observations and geodynamic mechanisms on the Earth, at present and in the past, which place the findings of this study into greater context within the Earth system.

## 4.1 Implications for correlation between IPV and wet MTZ

Determining that IPV patterns correlate with MTZ hydrous regions based on subduction influx and tectonic reconstructions supports the widely recognized hypothesis that water is transported to the MTZ by subducting slabs (Bodnar et al., 2013; Kelbert et al., 2009; Magni et al., 2014; Thompson, 1992; van Keken et al., 2011), and consequently generates spatial and temporal mantle heterogeneity (Peslier et al., 2017). This also suggests that tectonic reconstruction models are a valuable tool for exploring and estimating this heterogeneity. Generally, the MTZ water distribution over the period investigated (0-250 Ma) displays continuous hydration of particular regions. Many of these regions are overlain by IPV.

Many IPV samples occur above parts of great water content (here >2 $\cdot 10^9$ kg/km$^3$), including across Australia at 50 and 100 Ma and Eastern Asia at 0 and 200 Ma (Figure 14). Additionally, a considerable number of IPV locations at the present day are above regions of substantial amounts of water that subducted during the past four hundred million years (Figure 17d). More water generally promotes more melt at mantle PT conditions; accordingly, significant quantities of water (higher than this study's threshold of 2 $\cdot 10^6$ kg/km$^3$) are perhaps needed to generate IPV by hydrous upwellings. In any case, the extent of melting also depends on the temperature within the mantle; with higher temperatures, less water is required to produce the same amount of melt as with lower temperatures and more water (Karato et al., 2020).

Moreover, of the 53.5% IPV locations above wet MTZ (with the reference scenario) over the entire period investigated (past 250 Myr; Figure 15), 38.5% samples are above low water values (< 2 $\cdot 10^9$ kg/km$^3$), and only 15.0% samples are above locations of greater water content ($\geq$2 $\cdot 10^9$ kg/km$^3$). However, the role of water in the MTZ in the process that leads to IPV is not explored here; it could be that the presence of water only assists the development of IPV. Though I find a meaningful relationship between regions in the MTZ that might be wet due to subduction history and places where intraplate volcanism occurs, increasing the threshold (0.002 $\cdot 10^9$ kg/km$^3$) for whether a point in the MTZ is considered wet or not will strongly affect the results. A lower threshold could result in more IPV samples overlaying wet MTZ, while a higher threshold would likely cause a lower match percentage. However, we do not know if this will cause a reduced statistical significance. Therefore, we need better constraints on how much water is required to create IPV. This will be further discussed in Section 4.3.2.

More IPV eruptions possibly originated from hydrous MTZ material in the past, as I find a better agreement between IPV locations and the hydrated MTZ for past times (~125-250 Ma; Figure 19; Figure 21; Figure 22). Generally, the IPV dataset and plate tectonic reconstructions yield greater uncertainties further back in time; hence, one could conceivably expect the opposite trend. However, alternative explanations for the observed increase in matches for past times can be found by examining the IPV dataset and the tectonic reconstructions. Although one can observe a relatively low thermal parameter (which largely indicates less water influx into the MTZ from overlying subduction zones) before 250 Ma (Figure 2d), the total amount of water subducted to the deeper mantle may have still been significant (Figure 4b). This is because the total length of the subduction zone segments was eminently longer before 250 Ma (Figure 2a). Hence, the lateral extent of the subducted water was greater at past times, which is confirmed by the calculated area fraction of wet MTZ (Figure 19; Figure 21; Figure 22). Shortly after this increase in total subduction zone length and subsequent increase in the extent of hydrated areas in the MTZ for the scenarios with a $t_{MTZ}$ of 100 Myr and 30 Myr, far more IPV samples overlay hydrous parts of the MTZ. However, the above reasoning does not apply when $t_{MTZ}$ equal 0 Myr since water subducted at 250 Ma or earlier will sink to the lower mantle over the course of 22 million years and will therefore not be present in the MTZ (in contrast to when $t_{MTZ}$=100 Myr) at younger times (<225 Ma). Therefore, the area fraction of wet MTZ stays approximately the same throughout the entire period with a 0 Myr MTZ residence time (dashed blue line in Figure 19). Still, a markedly greater percentage of IPV overlay MTZ water around 200 Ma (solid blue line in Figure 19). Moreover, though I find a steady increase in the area fraction of wet MTZ for past times with the reference scenario, I also find a substantial increase in the number of IPV locations above wet MTZ between 125-150 Ma, indicating additional explanations for the observed increase in the number of matches at past times (Figure 16).

In addition, the global regassing flux has been much greater before 250 Ma compared to the past 100 Myr (Figure 4b). However, significant amounts of water subducted between 150-120 Ma, likely due to a rift pulse compensated by an increase in the convergence velocity (Figure 2b; Karlsen et al., 2019). This water would be stored within the MTZ at more recent times (<125 Ma) for all scenarios of varying MTZ residence time. This suggests that the match between hydrous MTZ regions and IPV location is more affected by the total length of the subduction zones (due to its effect on the distribution of MTZ water) than the global regassing flux. This further implies that the applied present-day regassing flux might only constitute a smaller uncertainty compared to other variables when using a low threshold ($2 \cdot 10^6$ kg/km$^3$) and possibly does not significantly impact the lateral extent of water in the MTZ and percentage of IPV locations above wet MTZ. This is further supported by the findings of more water in the MTZ (Table 2) and a much lower match percentage between wet regions of the MTZ and IPV locations (Figure 19), at 100 Ma than 250 Ma with a $t_{MTZ}$ of 0 Myr, 30 Myr and the reference scenario.

Another explanation for the unanticipated increasing match observed backward in time could be related to the IPV record; there is a decrease in the number of IPV samples at older times (Figure 10). A reasonable explanation for the increased percentage of IPV overlaying wet MTZ at past times could be that the sampled eruptions of the past are primarily of significant magnitude. In contrast, the more recent record, which has been sampled more extensively, includes additional small-scale volcanism. If voluminous eruptions generally characterize MTZ water-induced IPV, this could cause a more significant percentage of IPV over wet MTZ in the past. Hence, the small-scale ('relatively insignificant') IPV records are naturally filtered away for older times. Indeed, the fewest number of IPV samples is between 250-150 Ma (Figure 10), which is in good agreement with the observed concurrence between volcanism and water in the mantle (Figure 19; Figure 21; Figure 22).

### 4.1.1 Slab sinking rate and IPV delay period

For models with a 100 Myr MTZ residence time, that is, models displaying a statistical significance, I detected a range of average percentages (60-71%) of IPV over wet MTZ and low p-values (0.0243- 0.0481, Table 3). This range is a consequence of varying modeled slab sinking rates (1-9 cm/yr) and IPV delay periods (0-50 Myr). A more significant match percentage (71%) is displayed for slower rather than faster sinking velocities (Table 3). The increased number of IPV locations above wet MTZ with a slower slab sinking rate is likely due to more water (Table 2) and the greater extent of water in the MTZ (Figure 21). This is likely because it takes more time for the water to subduct through the MTZ. Still, it could possibly be due to a better fit between the extent of the water subducted at specific time periods present in the MTZ and IPV locations (more about this in Section 3.2.3).

The sinking rate of slabs in the upper mantle has been suggested to be greater than 1 cm/yr in most studies discussed in Section 2.2 (Bercovici & Karato, 2003; Domeier et al., 2016; Goes et al., 2011; van der Meer et al., 2018). Therefore, a 3 cm/yr rate is more in agreement with these findings. Furthermore, when increasing the delay time between the arrival of water in the MTZ and the eruption of IPV with 35 Myr, I find a more significant correspondence (69%) compared to the reference scenario (Table 3). A slower slab sinking rate results in a greater time gap between subduction of water and arrival of this water in the MTZ (since it spends more time sinking through the upper mantle); with a faster slab sinking rate, this time gap can be compensated for by adding an IPV delay period. The MTZ water distribution and IPV correspondence at a particular time with a slow sinking rate can be very much alike with a faster sinking rate by adding a delay period. Hence, the reference scenario ($v_{sink}$=3 cm/yr) with an increased IPV delay period (e.g., 35 Myr) could partly result in the same water distribution in the MTZ as with a 1 cm/yr $v_{sink}$ and no $t_{IPV}$. This could possibly explain the greater match percentage with slower slab sinking rates, as I expect volcanism to occur after some delay time.

Notably, simulating a 0-50 Myr IPV delay period with 5-Myr time intervals, I find the highest correspondence of IPV points above wet MTZ with a delay period of 35 Myr (69%). This further supports the expectation of an IPV delay period, which is reasonable as the hydrous melt must be created, ascend, and travel through the lithosphere to cause volcanic eruptions. However, it should be noted that these processes are possibly quite rapid, and more research is needed to constrain the process of IPV generation by hydrous melt. In addition, hydrous upwellings may already start forming before the oceanic lithosphere reaches the MTZ and begins to stagnate (Long et al., 2019). However, an ascent time of ~7-310 Myr for melt to ascend from the 410 km discontinuity to the base of the lithosphere has also been suggested (van der Lee et al., 2008). Suggestions of IPV delay times have previously been implied (elaborated in Section 2.4; Kuritani et al., 2011; Long et al., 2019; Motoki & Ballmer, 2015; Yang & Faccenda, 2020); however, due to poor constraints on mechanisms governing the development of IPV, such as MTZ melting and ascent of hydrous upwellings, the time it takes for IPV to occur after the water reaches the MTZ is not established. Additionally, this will undoubtedly vary depending on the slab characteristics, mantle conditions and flow, lithospheric thickness, etc. Intraplate volcanism has also been suggested to be caused by slabs interacting with ancient MTZ water reservoirs (Kuritani et al., 2011) that could be stable for millions (Schulze et al., 2018) or billions (Wang et al., 2017) of years. Thus, the IPV delay period of this water could potentially be much greater than considered here.

### 4.1.2 Implications of Earth's dynamic processes

Significant hydration of the MTZ depends on various processes presented throughout this project, e.g., slab water retention capabilities to great depths and slab dehydration at the 660 km discontinuity. Although this is the most plausible process behind MTZ hydration, other processes may possibly be involved. For instance, water brought even deeper into the mantle in cold and fast slabs could eventually rise with mantle flow, but these processes are unfortunately poorly understood. Moreover, although high water values promote IPV, they must do so in conjunction with other factors. The movement of materials in the mantle is complex and highly dependent on several processes that cause heterogeneity over time. This results in significant uncertainties regarding the long-term flow patterns of the mantle and the mechanism of material transport between the MTZ and the upper and lower mantles. Therefore, it is reasonable to believe that water could be stable over great timescales in one place but not in another. Thus, there could be mechanisms for transporting mantle material either down into the lower mantle (Andrault & Bolfan-Casanova, 2021; Schmandt et al., 2014), up into the upper mantle, and in some cases to the surface (Kameyama & Nishioka, 2012; Kelbert et al., 2009; Long et al., 2019), or mechanisms keeping the water within the MTZ (Karato et al., 2020). In addition, perhaps sufficient mantle upwelling is needed to drive the generated melts to reach the base of the lithosphere and erupt, independent of the local MTZ water content.

Various previously proposed and confirmed Earth processes demonstrate geodynamic mechanisms conceivably controlling MTZ water heterogeneity and affecting IPV development. Such Earth observations and mechanisms could possibly explain the presence or lack of hydrous regions in the MTZ or the occurrence or absence of IPV. Such processes could occur in regions other than those suggested in the subsequent section, on the Earth today or in the past. Moreover, it cannot be excluded that the presence or absence of water in the MTZ, or related IPV occurrences, could result from an interplay between several mechanisms controlling MTZ water heterogeneity or the development of IPV. This also applies to other regions of the globe or to geodynamic mechanisms not suggested here, at any time in Earth's history. In addition, even though significant amounts of water underlie the IPV locations, one cannot be sure that the water is a direct cause for this IPV. Importantly, though a link between IPV locations

and hydrous regions in the MTZ has been established in this study, what causes this link is not addressed. Perchance, the occurrence of IPV is not a direct consequence of, for example, hydrous upwellings. It could be that the water in the MTZ benefits another IPV mechanism (see Section 1.4), e.g., ascending flows in the 'Big Mantle Wedge' (Kameyama & Nishioka, 2012).

## 4.2 Regional discrepancies or concurrences

In all tested scenarios, some specific regions of the MTZ are always dry or wet throughout the investigated 250 Myr period, despite the range of variables explored and, consequently, the numerous predictive maps of MTZ water distribution. Above these various wet and dry MTZ regions, IPV both has, and has not, occurred. The reference scenario (Figure 14) and the 35 Myr MTZ water residence time scenario (Figure 25) of this study will be used to discuss these regions further since models with a 100 Myr MTZ water residence time yield a statistically significant correlation. In addition, the scenario of accumulating all subducted water in the MTZ for an infinite amount of time, which also showed statistically significant correlations, will be emphasized in the following subsections. It is worth noting that, in this study, I use a statistical methodology to determine the incidence of IPV over hydrous MTZ regions and find the statistical significance of these observations on a global scale. Therefore, although specific regions of the Earth are discussed, I do not aim to discriminate between IPV due to wet MTZ and other IPV processes in particular regions; far more extensive regional research is needed to do so. In the following subsections, the mapped hydrous regions of the MTZ, and various possible reasons for the observed discrepancies or concurrences with IPV locations, will be discussed.

### 4.2.1 A wet mantle transition zone and intraplate volcanism

The MTZ region below the present-day and past location of Eastern Asia displays the most distinct hydration for all scenarios and the greatest amount of IPV samples over time (Figure 25). This is due to the long history of subduction in this region. Here, the location of active IPV corresponds well to the region of deep mantle hydration, especially in the past with a $t_{MTZ}$ of 100 Myr (>50 Ma, Figure 25) and at all times with an ∞ Myr residence time. Indeed, these findings are in good agreement with suggestions of a hydrous MTZ causing IPV in Eastern Asia, as inferred from seismic tomography (Chen et al., 2017), geochemistry (Kuritani et al., 2011; Kuritani et al., 2019; Wang et al., 2015; Wang et al., 2017) and modeling (Long et al., 2019; Motoki & Ballmer, 2015; Sheng et al., 2016; Yang & Faccenda, 2020). Significant water transport into the deep mantle is expected below Eastern Asia because the cold Pacific plate initially subducted ~125 Myr ago (Sun et al., 2007) and is now subducting along the Japan trench (Kelbert et al., 2009). Hydrous phases could remain stable to great depths within an old and cold subducting lithosphere and slowly break down through time (elaborated in Section 1.2). Additionally, the Ryukyu, Honshu, Izu, and Japan-Southern Kurile slabs of the Philippine and western Pacific plates are significantly deflected above the 660 km discontinuity below Eastern Asia (Goes et al., 2017; Karato et al., 2001), which likely causes consequential hydration of the MTZ (elaborated in Section 1.3).

A poorer agreement between IPV locations and hydrated regions in the MTZ in Eastern Asia at more recent times (with $t_{MTZ}$ =100 Myr, Figure 25) could be due to the considerable length of the flat section of these slabs (estimated to be ~1000 – 1600 km, Goes et al., 2017). Especially when considering that IPV, believed to be associated with a hydrous MTZ below, has been found to regionally cluster above slab tips (also in Eastern Asia, Motoki & Ballmer, 2015; and references therein; Long et al., 2019). The displayed IPV (which overlay wet MTZ when $t_{MTZ}$ equals ∞ Myr) could be linked to water subducted at older times. Hence, a 100 Myr MTZ water residence time is perhaps not long enough to cause IPV in Eastern Asia at present day. Alternatively, IPV in Eastern Asia could be associated with a MTZ containing far more water than displayed here, due to ancient subduction and a long MTZ residence time (Kuritani et al., 2011; Wang et al., 2017). Indeed, IPV basalts with an EM1 (Enriched Mantle-1; commonly attributed to recycled crust and lithospheric mantle, Zindler & Hart, 1986) ancient (>1.5

Ga) sediment component have been found in Northeast China, this sediment component can only be related to ancient hydration of the MTZ (Kuritani et al., 2011; Wang et al., 2017). However, it's important to note that the occurrence of IPV could plausibly be attributed to a combination of ancient and recent hydration of the MTZ.

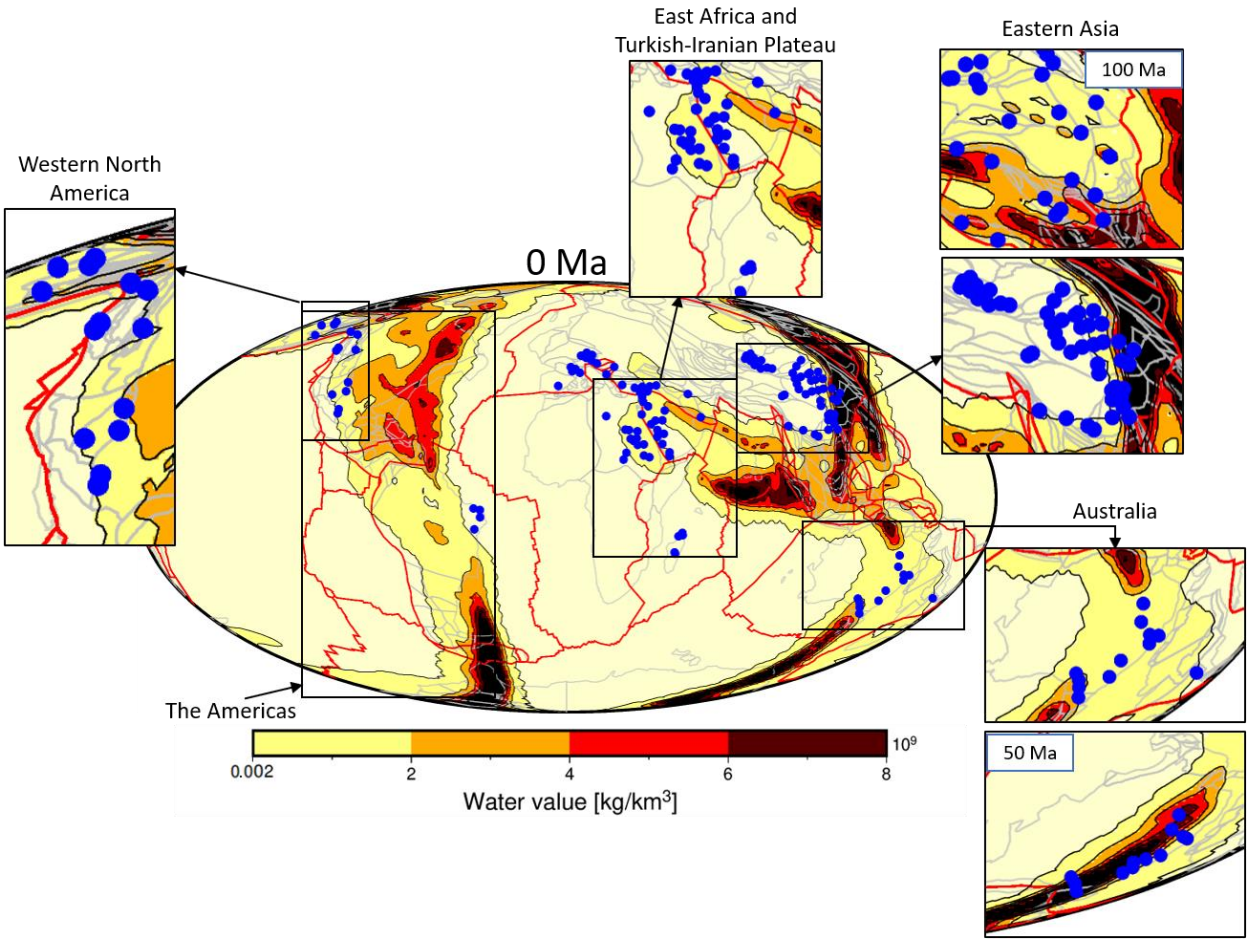


***Figure 25. Intensely hydrated MTZ regions.*** *The figure displays various regions of the Earth at the present day and additional frames from 50 Ma (Australia) and 100 Ma (Eastern Asia). The model parameters applied are a 100 Myr MTZ water residence time, 3 cm/yr slab sinking rate, and 35 Myr IPV delay period. The figure follows this studies threshold for hydrated MTZ, i.e., ≥0.002 ·$10^9$ kg/km$^3$.*

Notably, Eastern Asia is also associated with strongly elevated electrical conductivity values (Figure 26a, Kelbert et al., 2009), which could be caused by a substantial amount of water. Hence, this supports the likelihood of this area being more hydrated by significant subduction input than other parts of the MTZ. However, Houser (2016) suggested no evidence of considerable water content in this region by interpreting the topography of the transition zone observed in seismic tomography models (Figure 26b). This could be due to the method's limitations and uncertainties. Unfortunately, other seismological methods to detect water in the mantle using variations in seismic wave speeds in the MTZ have, so far, proven unsuccessful (Karato, 2011; Schulze et al., 2018). Electrical conductivity and seismic tomography measurements could also be affected by heat contrasts. However, Kuritani et al. (2019) investigated the composition of basalts from the Changbaishan volcano in Eastern Asia. They estimated the potential temperatures of the source mantle from the determined water contents to be in the range of normal upper mantle temperatures, suggesting that the upwelling causes magmatism not due to excess heat but possibly because of buoyancy caused by water in the MTZ.

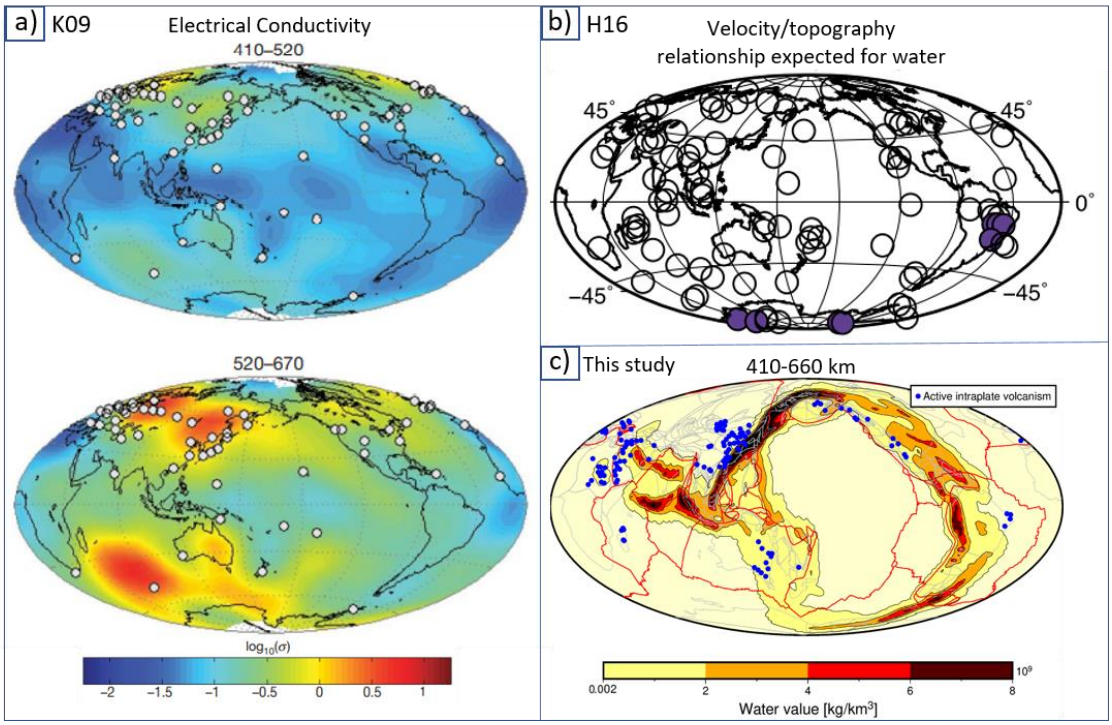


***Figure 26. Electrical conductivity and seismic tomography.*** *The figure displays (a) the MTZ electrical conductivity from K09 - Kelbert et al. (2009 ); a high conductivity could indicate water. The white points in (a) represent data stations. The figure in (b) shows points (dark purple) with a velocity/topography relationship that is expected for water in the transition zone from H16 - Houser (2016). In addition, (c) shows modeled water with the reference scenario of this study. The figures in (a) and (b) are modified from Kelbert et al. (2009) and Houser (2016), respectively.*

Another region showing a significantly hydrous MTZ is North America, which displays an eminent deep water influx through all times depicted, especially at 100 Ma (Figure 14; Figure 25). Though most regions of North America do not show any IPV, likely due to downwelling flow in the mantle below Central and Eastern North America (elaborated in Section 4.2.2), relatively many occurrences of IPV are in a confined area of Western North America during the past 50 Myr (Figure 25). These active IPV samples are currently located above hydrous regions even when applying a short (30 Myr) water residence time in the MTZ (Figure 17b). The mantle flow field beneath Western North America is dominated by shear flow rather than downwelling (Smith et al., 2008), which possibly could allow for the ascent of melt. However, the volcanism in Northwest America is poorly understood, and several different mechanisms have been suggested (Ballmer et al., 2015; Conrad et al., 2011; Dudas, 1991; Lipman & Glazner, 1991; Vollmer et al., 1984). However, it has also been proposed that these events could be due to hydrous upwellings related to slab stagnation (Faccenna et al., 2010; Long et al., 2019; Motoki & Ballmer, 2015; Yang & Faccenda, 2020), supporting the hypothesis of this thesis. As noted above, the presence of water in the MTZ and related IPV occurrences could be explained by an interplay between several different mechanisms controlling the development of IPV.

Perhaps the most striking correspondence between IPV and hydrated MTZ is displayed in Australia for the reference scenario at 50 Ma (Figure 25). Mather et al. (2020) suggest that subduction of the Pacific plate triggered IPV in Eastern Australia from 60 Ma to the present day and observe an increase in the eruption frequency with an increase in the slab flux. These findings are in good agreement with the results of this study, although alternative mechanisms, such as edge-driven convection or shear-driven upwelling, have been proposed to explain the occurrence of volcanism far from plate boundaries in this region (e.g., Conrad et al., 2011; Davies & Rawlinson, 2014). In addition, one can observe increased conductivity from the Tonga trench into Eastern Australia and towards Antarctica (Figure 26a), further agreeing with the observations in this study of a hydrous MTZ in this region.

Major upwelling of the mantle below East Africa and the big mantle plume below the Afar triple junction is likely the cause of the IPV samples in Eastern Africa (Figure 25; Behn et al., 2004; Schilling, 1973). However, I find a slightly hydrous MTZ beneath a confined area close to the Red Sea (with $t_{MTZ}$=100 Myr; Figure 25) overlain by numerous IPV samples at the present day and at 50 Ma (Figure 14a-b). In addition, this region has received a substantial amount of water throughout the past 400 Myr (Figure 17d) and is highly hydrous even after 200 Myr of recorded subduction (Figure 18d). High mantle temperatures and the presence of water could, together, create vast amounts of melt (elaborated in Section 4.1); hence, it is possible that the Afar plume and the possibly hydrous MTZ, in fact, interact with one another.

Close to the African Rift lays the Turkish-Iranian Plateau, beneath which, in this study, the MTZ is hydrous at present-day and at 50 Ma (Figure 25). This region also displays a notable amount of IPV; however, contrarily to East Africa, it is observed from seismic tomography images that the hot material does not penetrate the MTZ below the Turkish-Iranian Plateau (Alinaghi et al., 2007; Koulakov et al., 2012; Soltanmohammadi et al., 2018). This region is characterized by the long-lasting subduction of the Neo-Tethys Ocean, initiating in Triassic/Jurassic time (ca. 200 Ma, Hassanzadeh & Wernicke, 2016) from which it is here found substantial subduction water input to the deep mantle. Low velocity seismic anomalies, which are believed to be hydrous upwellings originating from the MTZ, have been observed from the base of the lithosphere to the top of the MTZ under the Turkish-Iranian Plateau (Soltanmohammadi et al., 2018). This suggests that the IPV observed over wet MTZ in this region is not plume inferred, but originates from MTZ hydrous upwellings, supporting the hypothesis of this thesis.

### 4.2.2 A wet mantle transition zone and no intraplate volcanism

The MTZ below the Americas is highly hydrous at all times depicted but not overlain by much volcanism (except in far western North America) compared to Eastern Asia (Figure 25). The Farallon slab subducted below North America during the Cretaceous and stagnated at MTZ depths. Subduction of this old oceanic lithosphere likely caused some of the observed significant water influx to the deep mantle beneath North America. However, parts of the stagnated Farallon slab are thought to have subducted vertically (Liu et al., 2008) and are currently sinking in the lower mantle below Eastern North America (Bunge & Grand, 2000; Conrad et al., 2004). The mantle below Central and Eastern North America is now dominated by downwelling associated with the descent of this slab (Bokelmann, 2002; Conrad et al., 2004; Smith et al., 2008; Wang et al., 2019). Perhaps this downgoing flow of MTZ material drained the MTZ water into the lower mantle (Schmandt et al., 2014), leaving the MTZ below Central and Eastern North America relatively dry (Liu et al., 2008). Alternatively, downwelling flow would undermine positively buoyant hydrous melt and suppress volcanism. However, a relatively dry MTZ below Central and Eastern North America is also in accordance with electrical conductivity measurements (Figure 26a, Kelbert et al., 2009). Another plausible reason for potentially lower water content below these regions, which could decrease IPV production by hydrous upwellings, is past major volcanic events, such as the Mid-Tertiary ignimbrite flare-up (Best et al., 2016), that could have degassed the MTZ. In addition, both processes may be attributable to altering the MTZ water content beneath North America, manifesting the system's complexity. Such mechanisms may also be at play in other regions where there is downwelling or where there has been major volcanism, such as in large igneous provinces. For example, mantle downwelling is also present right now in the Western North Atlantic and a broad region that includes the Mediterranean and to the east of it (Conrad et al., 2004).

Even less IPV is present in South and Central America than in North America in the past 50 Myr, even though a significant water distribution is found in the MTZ (Figure 25). Besides substantial subduction influx, slab stagnation above the 600 km discontinuity is thought to be a central mechanism for MTZ hydration. The Cocos, Peru, and Antilles slabs beneath South and Central America appear to penetrate directly and deeply into the lower mantle without much deflection in the MTZ (Goes et al., 2017; Karato et al., 2001). Provided that there is a shortage in MTZ hydration resulting from the lack of stagnation, there could be less hydrous melt and consequently relatively minor IPV in South and Central America. Penetration into the lower mantle is also thought to be the case for the Kamchatka (Russian Far East), Marianas, Sumatra, Hellenic (Crete and the surrounding area), and Alaska slabs, in addition to the Java and Kermadec (New Zealand) slabs which are possibly flat laying in the upper lower mantle (Goes et al., 2017). There is no IPV in these regions at the present day, except for in Alaska and one IPV sample in New Zealand.

### 4.2.3 A dry mantle transition zone and intraplate volcanism

The water mapped using the models of this study is transported to the MTZ through subduction; thereby, areas far from subduction zones throughout the considered period will undoubtedly be relatively dry unless ancient water (here >400 Ma) is stable or transported by other means to these regions (elaborated in Section 4.1.2). With all water accumulated in the MTZ throughout the period of interest, the present Earth gives a good representation of these explicitly dry areas (Figure 27). The slab sinking rate applied (3 cm/yr) in this model of ∞ Myr MTZ water residence time only represents one scenario. However, my results show that varying the slab sinking rate does not cause substantial changes in the water distribution (Figure 20). Thus, the dry regions at 0 Ma with the scenario of accumulating all subducted water in the MTZ throughout the past four hundred million years provides a reasonable outline of areas with no water contribution from overlaying subduction zones (Figure 27).

The present-day predicted map of accumulating all water in the MTZ suggests that the MTZ beneath the Indian Ocean, Southeast Africa, the South Atlantic Ocean, large parts of the North Pacific Ocean, and a modest area below Western Europe is dry throughout the entire period (Figure 27). Only three locations of IPV samples are observed within the continuously dry regions of this study; they include Western Europe, Madagascar (Figure 27), and India (Figure 18d) at present and past times. Alternative non-hydrous IPV mechanisms have been suggested in Madagascar (Pratt et al., 2017; Rasoazanamparany et al., 2021). Therefore, it should be emphasized that not all non-hotspot IPV is expected to arise from a hydrous MTZ. Likewise, many IPV locations within the hydrated areas might not be affiliated with a possibly wet MTZ underneath.

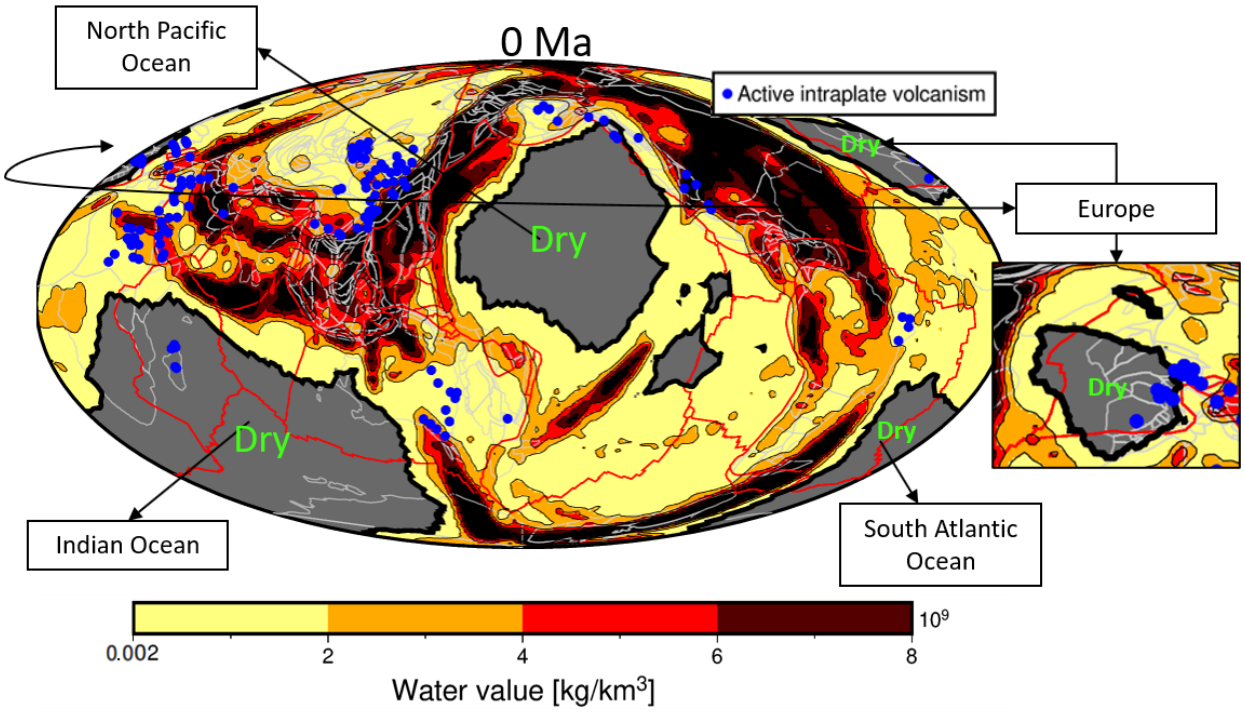


***Figure 27. Regions of no subduction input during the past 400 Myr.*** *The model parameters applied are an ∞ Myr MTZ water residence time, 3 cm/yr slab sinking rate, and 0 Myr IPV delay period, i.e., equivalent to Figure 17d. The outlined shaded gray areas represent large regions where no water has been mapped in none of the models of this study through the entire period investigated (past 400 Myr) and are therefore labeled as dry, i.e., water values <2 ·10$^6$ kg/km$^3$. In addition, a frame of Eastern Europe from an alternative view is shown.*

The dry area in Western Europe might be due to the lack of subduction in the used plate reconstructions model as a result of initial model inputs, such as velocity constraints and the selection of specific plate boundaries (Figure 12; elaborated in Section 2.1). However, it is well known that subduction of the Neo-Tethys, and later the Mediterranean, accommodating the convergence between Africa and Eurasia, has been ongoing since at least 100 Ma (e.g., Menant et al., 2018). Moreover, similar to the Pacific slab, slab stagnation has been imaged below this region (Faccenna et al., 2003; Goes et al., 2017; Utada et al., 2009). Nonetheless, the presence of subduction does not exclude the possibility of zero subduction water flux contribution to this region, as slabs may fully dehydrate before reaching the deeper mantle. Indeed, it has been suggested that the MTZ below Western Europe is relatively dry, resulting from slow subduction of young oceanic lithosphere (Utada et al., 2009). However, others have suggested that IPV in Europe is associated with slab stagnation in the MTZ (Faccenna et al., 2010; Long et al., 2019; Motoki & Ballmer, 2015; Yang & Faccenda, 2020). The Long et al. (2019) model predicts that any slab-associated hydrous minerals in the MTZ are expected to cause positively buoyant upwellings and sustain volcanism. Images of focused vertical upwellings below Europe, likely originating from the MTZ, have been attained from seismic tomography studies and are suggested to account for much of the IPV there (Keyser et al., 2002; Long et al., 2019; Ritter et al., 2001). In addition, subduction-related signatures in xenoliths from the Central European Volcanic Province have been found (Rizzo et al., 2021). However, there are many other proposed possible mechanisms for IPV in Europe (Bell et al., 2004; Buikin et al., 2005; Conrad et al., 2011; Goes et al., 1999).

Similarly to Europe, almost or complete dehydration of the oceanic lithosphere has also been proposed to occur at shallow mantle depths for the subduction zones of Cascadia and British Columbia, Mexico, Antilles, and parts of Marianas and Central and South America (Syracuse et al., 2010; van Keken et al., 2011). However, I do find a water contribution to the deep mantle at present-day at some of these locations (Figure 4c). The water flux to the deep mantle from subduction zone segments in this study is highly dependent on the $H_2O$ subduction flux parametrization applied (Karlsen et al., 2019), and subsequently, the used present-day regassing flux of $3.4 \cdot 10^{11}$ kg/yr (van Keken et al., 2011). Notably, this is a relatively high estimate and could result in predictive mappings of MTZ water in regions below subduction zones that have not, in reality, contributed to deep mantle hydration.

### 4.2.4 A dry mantle transition zone and no intraplate volcanism

Some of the above-mentioned regions with no water subducted during the past four hundred million years are not overlain by IPV (Figure 27), which fits well with the hypothesis of this study. There is no IPV above the dry North Pacific MTZ throughout all times investigated. However, there might not be IPV there since no continents have been present in this area, and oceanic intraplate volcanism has not been included in this study (elaborated in Section 2.3). Consequently, one cannot be confident that the lack of IPV results from these MTZ areas being continually dry since this study includes only continental IPV. Regardless, the absence of MTZ water beneath the Pacific Ocean is a reasonable assumption as degassing is sustained through mantle upwelling (Conrad & Behn, 2010), hotspot volcanism (Clouard & Bonneville, 2001), and past volcanism at mid-ocean ridges (Karlsen et al., 2020). The central Pacific basin exhibits all of these features, and therefore it is reasonable to believe that no ancient (here >400 Ma) stable MTZ water reservoir is present below the central Pacific Ocean. Moreover, lowered conductivity beneath the Pacific Ocean, South Atlantic Ocean, and South Africa is also observed (Figure 26a), which agrees with the explicitly dry areas found in this study.

Contradictorily, there is a high electrical conductivity region in the Indian ocean, suggesting an intensely hydrated MTZ (Figure 26a). This highly contrasts with the results of this study which shows an explicitly dry MTZ with no subduction input for the past 400 Myr in the same region (Figure 27). These discrepancies could partly be attributed to poor electrical conductivity data coverage. Areas of poor spatial data coverage include Middle and South America, the Southern Pacific, most of Africa, and the Indian Ocean (Few white points in Figure 26a; Kelbert et al., 2009). Alternatively, long-lived thermal upwelling of lower mantle material beneath Africa, associated with the Réunion or Kenya plume, is possibly extending into the Indian Ocean (Behn et al., 2004; Steinberger et al., 2021), which could cause the observed geophysical measurements by high temperatures and plume-related volcanism.

However, the results of this study do not rule out that water can be stable in the MTZ for more than 400 Myr. On the contrary, the statistically significant correlation determined with an infinite MTZ residence time indicates water stability over great time periods. Hence, some MTZ reservoirs could possibly be stable for millions of years while others undergo water drainage out of the MTZ; these processes likely differ depending on regional deep mantle material transport mechanisms. Therefore, the MTZ beneath the Indian ocean could contain stable water that perhaps subducted more than 400 Myr ago (Kuritani et al., 2011; Schulze et al., 2018). However, mantle upwelling and seafloor spreading have been active for the past ~150 Myr in the Indian Ocean (Karlsen et al., 2021; Karlsen et al., 2020; Matthews et al., 2016; Torsvik et al., 2019), suggesting that the MTZ should be highly degassed considering that there isn't displayed any contribution of subducted water to this region the past 400 Myr.

### 4.2.5 Spatial and temporal challenges

Mechanisms controlling MTZ water heterogeneity and affecting the development of IPV proposed in this section for different regions of the present Earth could have been representative of other regions of the Earth at past times. Unfortunately, insufficient knowledge of former mantle conditions poses an increasing challenge in interpreting and justifying concurrences and discrepancies observed further back in time. Other plausible explanations than those currently observable in the present Earth may also have been active.

## 4.3 Limitations

The uncertainties in the generated MTZ water grids are directly linked to and controlled by the underlying plate tectonic model (Karlsen et al., 2021; Karlsen et al., 2020; Matthews et al., 2016; Torsvik et al., 2019). Thus, the developed models are dependent on global plate motions and the locations of subduction zones. Since much of the geologic record is erased with time, the locations of plate boundaries and the plate kinematics are less constrained for the past. The predicted water maps will be characterized by more significant uncertainties for the older simulated times. In addition, various parameterizations and model inputs have been selected throughout this project, such as the threshold for wet MTZ and the number of nearest neighbors when spreading the water and processing the IPV dataset. Despite these various uncertainties, we identify a statistically significant correlation between IPV locations and the mapped hydrous regions of the MTZ.

### 4.3.1 IPV data

The locations of the active IPV samples are governed by uncertainties in their plate tectonic reconstructions and their GEOROC classification (GROROC, 2021). Remarkably, as discussed in Section 4.1, all scenarios display a generally better correspondence between IPV and MTZ water content further back in time (Figure 19; Figure 21; Figure 22). This is despite the fact that uncertainty surrounding IPV locations and eruption time is also increasing. Volcanism classified as intracontinental (far from plate boundaries) today might have erupted close to plate boundaries in the past. The locations of the intraplate eruptions have been reconstructed from plate tectonic reconstructions; since continents assemble and break up, the IPV samples could have been part of a volcanic arc in the past. Arc volcanism is created close to and due to the subduction of oceanic lithosphere and would therefore be significantly connected to mappings of hydrous MTZ regions from models of subduction flux. However, most IPV samples, when rotated back to their eruption locations, are not displayed close to the reconstructed plate boundaries (red lines) at 200 Ma and 250 Ma (Figure 14e-f). Alternative reasons for this trend are further discussed in Section 4.1.

Limitations in the model-test with IPV samples could be associated with the raw data selection. The used dataset includes only intraplate volcanism with basaltic composition erupted in continental lithosphere. Hence, oceanic intraplate volcanism has not been included in this study. The oceanic lithosphere is continually recycled into the deep mantle; thus, the record is inadequate back in time. In addition, the likelihood of ocean island basalts being plume-related is great and would presumably cause a lower statistical significance. Despite attempts to limit plume-related samples, an unknown number of IPV samples in the used dataset have a plume source, e.g., the Afar plume below the African rift. The ability to remove these points was constrained by limited knowledge of past plume events; known hotspot volcanism was therefore not filtered out to preserve consistency. Additional limitations could also arise from varying classifications of volcanism in the GEOROC database (GROROC, 2021).

Furthermore, IPV samples associated with the same nearest neighbor mesh point were clustered into one point (see Section 2.3); the distance set for which a sample was associated or not could be too long or too short depending on the particular event. This adds uncertainty; however, assumptions about the affiliation of IPV events were made to prevent oversampling. However, despite the above constraints, seeing that a significant percentage of IPV lies above wet MTZ and the sufficiently low p-values, the limitations concerning the IPV dataset do not significantly affect this study's general conclusions.

### 4.3.2 Model parameters

The distribution of water in the models is highly dependent on how the water is spread out, that is, the number of nearest neighbors to which the water is distributed. Ten neighbors have been chosen for all scenarios. A larger number of nearest neighbors results in more mesh points that contain water and fewer mesh points with very high water values (Figure 7). This spreading was done to account for the diffusion of water, slab dip, and possible horizontal movements of stagnated slabs. The horizontal transport of water in the mantle is poorly constrained and likely differs greatly depending on the subduction zone segment. However, vertical subduction has been suggested to be a reasonable assumption to map subducted slabs (Domeier et al., 2016); therefore, perhaps the spreading of the water in this study is not too modest. However, although diffusion of water is very slow in mantle conditions (Peslier et al., 2017), IPV often occurs above the tip of stagnated slabs (Motoki & Ballmer, 2015; and references therein; Long et al., 2019). Therefore, it is reasonable to consider some amount of horizontal spread of water that considers the complex shapes slabs could have in the MTZ. Additionally, the consequence of spreading the water is minimal compared to the MTZ residence time, both for the distribution of the water and the match with IPV.

One of the greatest uncertainties of the statistical significance test is the threshold for wet or dry MTZ, here set to $2 \cdot 10^6$ kg/km$^3$ (Section 2.4.1). A low threshold was reasonable as even a tiny amount of water could produce significantly lowered viscosities and melt production in mantle conditions. In addition, the mechanism behind the creation of IPV is not investigated here. Even though greater amounts of water are imperative to create positively buoyant hydrous upwelling to the lithosphere base, we do not know if this is the link between IPV and MTZ water. It might well be that small amounts of water in the MTZ accommodate other mechanisms that could produce IPV without MTZ water by increasing the amount of melt, therefore only increasing the possibility of the formation of IPV. In addition, if the occurrence of IPV is strongly connected to slab interaction with ancient hydration of the MTZ, a high threshold would be unreasonable when only considering ‘recent’ hydration. In conclusion, this threshold may greatly impact the match percentage and statistical significance between the IPV locations and the hydrated MTZ regions. An improved understanding of the mechanism behind non-hotspot IPV is needed to constrain this threshold further.

## 4.4 Future work

There is still much we do not know about the amount of water in the mantle, its distribution, and its effect on the creation of IPV. Future work is needed to limit the uncertainties associated with water transport and release to the deep mantle. Although I believe that the models of this study capture the fundamental mechanisms controlling the MTZ water distribution from recent subduction, these findings should be verified by further improving the models. This could be done by testing more variables starting from the model of greatest statistical significance (i.e., $t_{MTZ}$=100 Myr, $v_{sink}$=3 cm/yr, and $t_{IPV}$=35 Myr) as a starting point. Future research should also consider that individual subduction zones are controlled by different mechanisms that control the distribution of heterogeneous water storage in the mantle. For example, the MTZ water residence time, which depends on the slab stagnation time, could be approximated from slab age and trench retreat (Goes et al., 2017; Kameyama & Nishioka, 2012). While the slab sinking rate could be affected by the convergence velocity and vary among different slabs. In addition, slab dip should be considered to better constrain the spreading of the water.

Furthermore, this study is influenced by uncertainties in the tectonic reconstructions and the IPV dataset; thus, we need improved models and sampling to further determine the effect of water in the MTZ on IPV. The present-day water flux of this study is highly based on the estimate of van van Keken et al. (2011); however, other studies have suggested various different estimates. Although I have shown that this estimate does not profoundly affect the water distribution in the MTZ, it is essential if one were to consider the water concentration needed to create IPV. Hence, other factors that we should aim to better understand in the future are the processes behind the creation of IPV related to the hydrated MTZ; this would further improve our understanding of the IPV delay period and wet MTZ threshold. It should also for example be tested if increasing the wet MTZ threshold results in a reduced statistical significance. Additionally, better constraints on geophysical methods are of great importance to verify the MTZ water distribution and link to IPV discussed in this study. These advancements could perhaps give an enhanced understanding of the past and future evolution of the deep water cycle and volcanism on Earth and other planets.

# 5. Conclusions

In this study, I have demonstrated that the spatial and temporal heterogeneous distribution of water storage in the mantle transition zone (MTZ, 410-660 km) can be mapped based on tectonic reconstructions of subduction zones throughout time (here 400 Myr) despite various uncertainties related to the plate tectonic model. The statistical approach conducted here suggests a correlation between hydrous regions in the MTZ and the patterns of intraplate volcanism (IPV), supporting the hypothesis of this thesis. In this parametric study, I have varied the residence time of water in the MTZ, the slab sinking rate, and the delay period between water in the MTZ and IPV occurrence. All maps of MTZ water distribution with a 100 Myr and ∞ Myr water residence time within the MTZ yield a statistically significant correlation to locations of active IPV and show a large fraction of IPV locations above hydrated MTZ regions. This highlights the importance of slab deformation and associated stalling above the upper-lower mantle discontinuity for retaining water in the MTZ, and that water reservoirs within the MTZ are likely stable for ~100 million years or more.

The observed percentage of IPV locations above wet MTZ regions for MTZ water residence times of 30 Myr and shorter was not significantly different from the null-hypothesis at the 95% confidence level, suggesting that the MTZ residence time exert significant control on the water distribution. At the same time, changes in the distribution due to variations in slab sinking rate and IPV delay period are modest, suggesting these factors impart only a secondary effect. However, with a 35 Myr delay period between water in the MTZ and occurrence of IPV the match percentage increases by 5% compared to when not accounting for a delay (Table 3), supporting the likelihood of some IPV delay. In addition, with an infinite MTZ water residence time, I find a statistically significant correlation and an outstanding correspondence of 89% between hydrous MTZ regions and IPV. These findings are in good agreement with suggestions from previous studies that intraplate volcanism can arise from a hydrous MTZ and with observations of IPV above parts of the MTZ with substantial subduction input, such as Eastern Asia, Eastern North America, Eastern Europe, Australia, and the Turkish-Iranian Plateau.

The parametrized maps of MTZ water distribution are not strongly affected by the amount of water subducted at trenches or the total amount of water in the MTZ, but rather the extent of the subduction zones. I find that the area fraction of wet MTZ observed with the reference scenario to be much greater in the past (>150 Ma; Figure 16), while the MTZ water content was more significant at younger times (~100-25 Ma; Table 2). Several potential geodynamic processes can explain the concurrences and discrepancies between wet or dry MTZ regions and IPV. However, it is beyond the scope of this thesis to conclude which reasons have caused the concurrences and discrepancies observed; comprehensive future research is essential to understand the mechanisms behind the IPV and wet MTZ link found in this study and the effects of these findings on a regional scale. Nevertheless, the statistically significant link between IPV and the distribution of water in the MTZ discovered in this study suggests that water is both transported into the MTZ by subduction and that this water facilitates IPV at the surface.

# Bibliography


Aivazpourporgou, S., Thiel, S., Hayman, P. C., Moresi, L. N., & Heinson, G. (2015). Decompression melting driving intraplate volcanism in Australia: Evidence from magnetotelluric sounding. *Geophys. Res. Lett*, *42*(2), 346-354. https://doi.org/10.1002/2014GL060088

Alinaghi, A., Koulakov, I., & Thybo, H. (2007). Seismic tomographic imaging of P- and S-waves velocity perturbations in the upper mantle beneath Iran. *Geophys. J. Int*, *169*(3). https://doi.org/10.1111/j.1365-246X.2007.03317.x

Andrault, D., & Bolfan-Casanova, N. (2021). Mantle rain toward the Earth's surface: A model for the internal cycle of water. *Physics of the earth and planetary interiors*, *322*. https://doi.org/10.1016/j.pepi.2021.106815

Ballmer, M. D., Conrad, C. P., Smith, E. I., & Harmon, N. (2013). Non-hotspot volcano chains produced by migration of shear-driven upwelling toward the East Pacific Rise. *Geology (Boulder)*, *41*(4), 479-482. https://doi.org/10.1130/G33804.1

Ballmer, M. D., Conrad, C. P., Smith, E. I., & Johnsen, R. (2015). Intraplate volcanism at the edges of the Colorado Plateau sustained by a combination of triggered edge-driven convection and shear-driven upwelling. *Geochem. Geophys. Geosyst*, *16*, 366-379. https://doi.org/10.1002/2014GC005641

Ballmer, M. D., van Hunen, J., Ito, G., Tackley, P. J., & Bianco, T. A. (2007). Non-hotspot volcano chains originating from small-scale sublithospheric convection. *Geophys. Res. Lett*, *34*(23). https://doi.org/10.1029/2007GL031636

Behn, M. D., Conrad, C. P., & Silver, P. G. (2004). Detection of upper mantle flow associated with the African Superplume. *Earth and planetary science letters*, *224*(3), 259-274. https://doi.org/10.1016/j.epsl.2004.05.026

Bell, D. R., & Rossman, G. R. (1992). Water in Earth's Mantle: The Role of Nominally Anhydrous Minerals. *Science*, *255*(5050), 1391-1397. https://doi.org/10.1126/science.255.5050.1391

Bell, K., Castorina, F., Lavecchia, G., Rosatelli, G., & Stoppa, F. (2004). Is there a mantle plume below Italy? *Eos Trans. AGU*, *85*(50), 541-547. https://doi.org/10.1029/2004EO500002

Bercovici, D., & Karato, S.-i. (2003). Whole-mantle convection and the transition-zone water filter. *Nature*, *425*(6953), 39-44. https://doi.org/10.1038/nature01918

Best, M. G., Christiansen, E. H., de Silva, S. L., & Lipman, P. W. (2016). Slab-rollback ignimbrite flareups in the southern Great Basin and other Cenozoic American arcs; a distinct style of arc volcanism. *Geosphere (Boulder, Colo.)*, *12*(4), 1097-1135. https://doi.org/10.1130/GES01285.1

Bianco, T. A., Conrad, C. P., & Smith, E. I. (2011). Time dependence of intraplate volcanism caused by shear-driven upwelling of low-viscosity regions within the asthenosphere. *J. Geophys. Res*, *116*(B11). https://doi.org/10.1029/2011JB008270

Bodnar, R. J., Azbej, T., Becker, S. P., Cannatelli, C., Fall, A., & Severs, M. J. (2013, 2013). Whole Earth geohydrologic cycle, from the clouds to the core: The distribution of water in the dynamic Earth system.

Bokelmann, G. H. R. (2002). Which forces drive North America? *Geology (Boulder)*, *30*(11), 1027-1030. https://doi.org/https://doi.org/10.1130/0091-7613(2002)030<1027:WFDNA>2.0.CO;2

Bolfan-Casanova, N., McCammon, C. A., & Mackwell, S. J. (2006). Water in Transition Zone and Lower Mantle Minerals. In (Vol. 168, pp. 57-68). Washington, D. C: American Geophysical Union. https://doi.org/10.1029/168GM06

Bonatti, E., & Harrison, C. G. A. (1976). Hot lines in the Earth's mantle. *Nature (London)*, *263*(5576), 402-404. https://doi.org/10.1038/263402a0

Boyden, J. A., Müller, R. D., Gurnis, M., Torsvik, T. H., Clark, J. A., Turner, M., Ivey-Law, H., Watson, R. J., & Cannon, J. S. (2011). Next-generation plate-tectonic reconstructions using GPlates. In (Vol. 9780521897150, pp. 95-114). Cambridge University Press. https://doi.org/10.1017/CBO9780511976308.008

Buikin, A., Trieloff, M., Hopp, J., Althaus, T., Korochantseva, E., Schwarz, W. H., & Altherr, R. (2005). Noble gas isotopes suggest deep mantle plume source of late Cenozoic mafic alkaline volcanism in Europe. *Earth and planetary science letters*, *230*(1-2), 143-162. https://doi.org/10.1016/j.epsl.2004.11.001

Bunge, H.-P., & Grand, S. P. (2000). Mesozoic plate-motion history below the northeast Pacific Ocean from seismic images of the subducted Farallon slab. *Nature*, *405*(6784), 337-340. https://doi.org/10.1038/35012586

Butterworth, N. P., Talsma, A. S., Müller, R. D., Seton, M., Bunge, H. P., Schuberth, B. S. A., Shephard, G. E., & Heine, C. (2014). Geological, tomographic, kinematic and geodynamic constraints on the dynamics of sinking slabs. *Journal of geodynamics*, *73*, 1-13. https://doi.org/10.1016/j.jog.2013.10.006

Chen, C., Zhao, D., Tian, Y., Wu, S., Hasegawa, A., Lei, J., Park, J.-H., & Kang, I.-B. (2017). Mantle transition zone, stagnant slab and intraplate volcanism in Northeast Asia. *Geophysical journal international*. https://doi.org/10.1093/gji/ggw491

Clouard, V., & Bonneville, A. (2001). How many Pacific hotspots are fed by deep-mantle plumes? *Geology (Boulder)*, *29*(8), 695-698. https://doi.org/https://doi.org/10.1130/0091-7613(2001)029<0695:HMPHAF>2.0.CO;2

Conrad, C. P. (2013). The solid Earth's influence on sea level. *GSA Bulletin*, *125*(7-8), 1027-1052. https://doi.org/10.1130/b30764.1

Conrad, C. P., & Behn, M. D. (2010). Constraints on lithosphere net rotation and asthenospheric viscosity from global mantle flow models and seismic anisotropy. *Geochem. Geophys. Geosyst*, *11*(5). https://doi.org/10.1029/2009GC002970

Conrad, C. P., Bianco, T. A., Smith, E. I., & Wessel, P. (2011). Patterns of intraplate volcanism controlled by asthenospheric shear. *Nature geoscience*, *4*(5), 317-321. https://doi.org/10.1038/ngeo1111

Conrad, C. P., Lithgow-Bertelloni, C., & Louden, K. E. (2004). Iceland, the Farallon Slab, and dynamic topography of the North Atlantic. *Geology (Boulder)*, *32*(3), 177-180. https://doi.org/10.1130/G20137.1

Conrad, C. P., Wu, B., Smith, E. I., Bianco, T. A., & Tibbetts, A. (2010). Shear-driven upwrelling induced by lateral viscosity variations and asthenospheric shear: A mechanism for intraplate volcanism. *Physics of the earth and planetary interiors*, *178*(3-4), 162-175. https://doi.org/10.1016/j.pepi.2009.10.001

Crowley, J. W., Gérault, M., & O'Connell, R. J. (2011). On the relative influence of heat and water transport on planetary dynamics. *Earth and planetary science letters*, *310*(3), 380-388. https://doi.org/10.1016/j.epsl.2011.08.035

Davies, D. R., & Rawlinson, N. (2014). On the origin of recent intraplate volcanism in Australia. *Geology (Boulder)*, *42*(12), 1031-1034. https://doi.org/10.1130/G36093.1

Demouchy, S. (2010). Diffusion of hydrogen in olivine grain boundaries and implications for the survival of water-rich zones in the Earth's mantle. *Earth and planetary science letters*, *295*(1-2), 305-313. https://doi.org/10.1016/j.epsl.2010.04.019

Demouchy, S., Deloule, E., Frost, D. J., & Keppler, H. (2005). Pressure and temperature-dependence of water solubility in Fe-free wadsleyite. *The American mineralogist*, *90*(7), 1084-1091. https://doi.org/10.2138/am.2005.1751

Domeier, M., Doubrovine, P. V., Torsvik, T. H., Spakman, W., & Bull, A. L. (2016). Global correlation of lower mantle structure and past subduction. *Geophys Res Lett*, *43*(10), 4945-4953. https://doi.org/10.1002/2016GL068827

Drewitt, J. W. E., Walter, M. J., Brodholt, J. P., Muir, J. M. R., & Lord, O. T. (2022). Hydrous silicate melts and the deep mantle H.sub.2O cycle. *Earth and planetary science letters*, *581*. https://doi.org/10.1016/j.epsl.2022.117408

Dudas, F. O. (1991). Geochemistry of igneous rocks from the Crazy Mountains, Montana, and tectonic models for the Montana Alkalic Province. *J. Geophys. Res*, *96*(B8), 13261-13277. https://doi.org/10.1029/91JB00246

Dumoulin, C., Choblet, G., & Doin, M. P. (2008). Convective interactions between oceanic lithosphere and asthenosphere: Influence of a transform fault. *Earth and planetary science letters*, *274*(3), 301-309. https://doi.org/10.1016/j.epsl.2008.07.017

Faccenda, M. (2014). Water in the slab: A trilogy. *Tectonophysics*, *614*, 1-30. https://doi.org/10.1016/j.tecto.2013.12.020

Faccenda, M., Gerya, T. V., Mancktelow, N. S., & Moresi, L. (2012). Fluid flow during slab unbending and dehydration: Implications for intermediate-depth seismicity, slab weakening and deep water recycling. *Geochem. Geophys. Geosyst*, *13*(1). https://doi.org/10.1029/2011GC003860

Faccenna, C., Becker, T. W., Lallemand, S., Lagabrielle, Y., Funiciello, F., & Piromallo, C. (2010). Subduction-triggered magmatic pulses: A new class of plumes? *Earth and planetary science letters*, *299*(1), 54-68. https://doi.org/10.1016/j.epsl.2010.08.012

Faccenna, C., Jolivet, L., Piromallo, C., & Morelli, A. (2003). Subduction and the depth of convection in the Mediterranean mantle. *J. Geophys. Res*, *108*(B2). https://doi.org/10.1029/2001JB001690

Fei, H., Yamazaki, D., Sakurai, M., Miyajima, N., Ohfuji, H., Katsura, T., & Yamamoto, T. (2017). A nearly water-saturated mantle transition zone inferred from mineral viscosity. *Sci Adv*, *3*(6), e1603024-e1603024. https://doi.org/10.1126/sciadv.1603024

Fix, E., & Hodges, J. J. L. (1951). *Discriminatory Analysis - Nonparametric Discrimination: Consistency Properties*.

Gerbault, M., Burov, E. B., Poliakov, A. N. B., & Daignières, M. (1999). Do faults trigger folding in the lithosphere? *Geophys. Res. Lett*, *26*(2), 271-274. https://doi.org/10.1029/1998GL900293

Goes, S., Agrusta, R., van Hunen, J., & Garel, F. (2017). Subduction-transition zone interaction; a review. *Geosphere (Boulder, Colo.)*, *13*(3), 644-664. https://doi.org/10.1130/GES01476.1

Goes, S., Capitanio, F. A., Morra, G., Seton, M., & Giardini, D. (2011). Signatures of downgoing plate-buoyancy driven subduction in Cenozoic plate motions. *Physics of the earth and planetary interiors*, *184*(1), 1-13. https://doi.org/10.1016/j.pepi.2010.10.007

Goes, S., Spakman, W., & Bijwaard, H. (1999). A Lower Mantle Source for Central European Volcanism. *Science*, *286*(5446), 1928-1931. https://doi.org/10.1126/science.286.5446.1928

GROROC. (2021). *GEOROC - Geochemistry of Rocks of the Oceans and Continents*. Max Planck Institute for Chemistry Mainz Germany. Retrieved 16.11.2021 from http://georoc.mpch-mainz.gwdg.de/georoc/Start.asp

Gurnis, M., Turner, M., Zahirovic, S., DiCaprio, L., Spasojevic, S., Müller, R. D., Boyden, J., Seton, M., Manea, V. C., & Bower, D. J. (2012). Plate tectonic reconstructions with continuously closing plates. *Computers & geosciences*, *38*(1), 35-42. https://doi.org/10.1016/j.cageo.2011.04.014

Hackeling, G. (2017). Classification and regression with k-Nearest Neighbors. In *Mastering Machine Learning with scikit-learn - Second Edition* (Second ed., pp. 32-37). Birmingham: Packt Publishing, Limited.

Hacker, B. R. (2008). H2O subduction beyond arcs. *Geochem. Geophys. Geosyst*, *9*(3). https://doi.org/10.1029/2007GC001707
Hassanzadeh, J., & Wernicke, B. P. (2016). The Neotethyan Sanandaj-Sirjan zone of Iran as an archetype for passive margin-arc transitions. *Tectonics (Washington, D.C.)*, *35*(3), 586-621. https://doi.org/10.1002/2015TC003926
Hernlund, J. W., Stevenson, D. J., & Tackley, P. J. (2008). Buoyant melting instabilities beneath extending lithosphere: 2. Linear analysis. *J. Geophys. Res*, *113*(B4). https://doi.org/10.1029/2006JB004863
Hieronymus, C. F., & Bercovici, D. (1999). Discrete alternating hotspot islands formed by interaction of magma transport and lithospheric flexure. *Nature (London)*, *397*(6720), 604-607. https://doi.org/10.1038/17584
Hieronymus, C. F., & Bercovici, D. (2000). Non-hotspot formation of volcanic chains: control of tectonic and flexural stresses on magma transport. *Earth and planetary science letters*, *181*(4), 539-554. https://doi.org/10.1016/S0012-821X(00)00227-2
Hirschmann, M., & Kohlstedt, D. (2012). Water in Earth's mantle. *Physics today*, *65*(3), 40-45. https://doi.org/10.1063/PT.3.1476
Hirschmann, M. M. (2006). Water, melting, and the deep Earth H2O cycle. *Annual review of earth and planetary sciences*, *34*(1), 629-653. https://doi.org/10.1146/annurev.earth.34.031405.125211
Hounslow, M. W., Domeier, M., & Biggin, A. J. (2018). Subduction flux modulates the geomagnetic polarity reversal rate. *Tectonophysics*, *742-743*, 34-49. https://doi.org/10.1016/j.tecto.2018.05.018
Houser, C. (2016). Global seismic data reveal little water in the mantle transition zone. *Earth and planetary science letters*, *448*, 94-101. https://doi.org/10.1016/j.epsl.2016.04.018
Huang, J.-X., Li, P., Griffin, W. L., Xia, Q.-K., Gréau, Y., Pearson, N. J., & O'Reilly, S. Y. (2014). Water contents of Roberts Victor xenolithic eclogites: primary and metasomatic controls. *Contributions to mineralogy and petrology*, *168*(6), 1-13. https://doi.org/10.1007/s00410-014-1092-5
Huang, X., Xu, Y., & Karato, S.-i. (2005). Water content in the transition zone from electrical conductivity of wadsleyite and ringwoodite. *Nature*, *434*(7034), 746-749. https://doi.org/10.1038/nature03426
Inoue, T., Wada, T., Sasaki, R., & Yurimoto, H. (2010). Water partitioning in the Earth's mantle. *Physics of the earth and planetary interiors*, *183*(1-2), 245-251. https://doi.org/10.1016/j.pepi.2010.08.003
Kameyama, M., & Nishioka, R. (2012). Generation of ascending flows in the Big Mantle Wedge (BMW) beneath northeast Asia induced by retreat and stagnation of subducted slab. *Geophys. Res. Lett*, *39*(10). https://doi.org/10.1029/2012GL051678
Karato, S.-I. (2007). Microscopic Models for the Effects of Hydrogen on Physical and Chemical Properties of Earth Materials. In (pp. 321-356). Dordrecht: Springer Netherlands. https://doi.org/10.1007/978-1-4020-5750-2_12
Karato, S.-i. (2011). Water distribution across the mantle transition zone and its implications for global material circulation. *Earth and planetary science letters*, *301*(3), 413-423. https://doi.org/10.1016/j.epsl.2010.11.038
Karato, S.-i., Karki, B., & Park, J. (2020). Deep mantle melting, global water circulation and its implications for the stability of the ocean mass. *Progress in earth and planetary science*, *7*(1), 1-25. https://doi.org/10.1186/s40645-020-00379-3
Karato, S.-i., Riedel, M. R., & Yuen, D. A. (2001). Rheological structure and deformation of subducted slabs in the mantle transition zone: implications for mantle circulation and deep earthquakes. *Physics of the earth and planetary interiors*, *127*(1), 83-108. https://doi.org/10.1016/S0031-9201(01)00223-0

Karlsen, K. S., Conrad, C. P., Domeier, M., & Trønnes, R. G. (2021). Spatiotemporal Variations in Surface Heat Loss Imply a Heterogeneous Mantle Cooling History. *Geophysical research letters*, *48*(6). https://doi.org/10.1029/2020GL092119

Karlsen, K. S., Conrad, C. P., & Magni, V. (2019). Deep Water Cycling and Sea Level Change Since the Breakup of Pangea. *Geochemistry, geophysics, geosystems : G3*, *20*(6), 2919-2935. https://doi.org/10.1029/2019GC008232

Karlsen, K. S., Domeier, M., Gaina, C., & Conrad, C. P. (2020). A tracer-based algorithm for automatic generation of seafloor age grids from plate tectonic reconstructions. https://doi.org/https://doi.org/10.1016/j.cageo.2020.104508

Kelbert, A., Schultz, A., & Egbert, G. (2009). Global electromagnetic induction constraints on transition-zone water content variations [Report]. *Nature*, *460*, 1003+. https://link.gale.com/apps/doc/A206866718/AONE?u=anon~a570ec64&sid=googleScholar&xid=f290d8e0

Keyser, M., Ritter, J. R. R., & Jordan, M. (2002). 3D shear-wave velocity structure of the Eifel plume, Germany. *Earth and planetary science letters*, *203*(1), 59-82. https://doi.org/10.1016/S0012-821X(02)00861-0

Kohlstedt, D. L., & Mackwell, S. J. (1998). Diffusion of Hydrogen and Intrinsic Point Defects in Olivine. *Zeitschrift für physikalische Chemie (Neue Folge)*, *207*(1), 147-162. https://doi.org/10.1524/zpch.1998.207.Part_1_2.147

Komabayashi, T., & Omori, S. (2006). Internally consistent thermodynamic data set for dense hydrous magnesium silicates up to 35GPa, 1600°C: Implications for water circulation in the Earth's deep mantle. *Physics of the earth and planetary interiors*, *156*(1-2), 89-107. https://doi.org/10.1016/j.pepi.2006.02.002

Korenaga, J. (2011). Thermal evolution with a hydrating mantle and the initiation of plate tectonics in the early Earth. *J. Geophys. Res*, *116*(B12). https://doi.org/10.1029/2011JB008410

Korenaga, J., Planavsky, N. J., & Evans, D. A. D. (2017). Global water cycle and the coevolution of the Earth's interior and surface environment. *Philos Trans A Math Phys Eng Sci*, *375*(2094), 20150393-20150393. https://doi.org/10.1098/rsta.2015.0393

Koulakov, I., Zabelina, I., Amanatashvili, I., & Meskhia, V. (2012). Nature of orogenesis and volcanism in the Caucasus region based on results of regional tomography. *Solid earth (Göttingen)*, *3*(2), 327-337. https://doi.org/10.5194/se-3-327-2012

Kuritani, T., Ohtani, E., & Kimura, J.-I. (2011). Intensive hydration of the mantle transition zone beneath China caused by ancient slab stagnation. *Nature geoscience*, *4*(10), 713-716. https://doi.org/10.1038/ngeo1250

Kuritani, T., Xia, Q.-K., Kimura, J.-I., Liu, J., Shimizu, K., Ushikubo, T., Zhao, D., Nakagawa, M., & Yoshimura, S. (2019). Buoyant hydrous mantle plume from the mantle transition zone. *Sci Rep*, *9*(1), 6549-6549. https://doi.org/10.1038/s41598-019-43103-y

Lipman, P. W., & Glazner, A. F. (1991). Introduction to Middle Tertiary Cordilleran Volcanism: Magma Sources and Relations to Regional Tectonics. *J. Geophys. Res*, *96*(B8), 13193-13199. https://doi.org/10.1029/91JB01397

Liu, L., Spasojevic, S., & Gurnis, M. (2008). Reconstructing Farallon Plate Subduction beneath North America Back to the Late Cretaceous. *Science*, *322*(5903), 934-938. https://doi.org/10.1126/science.1162921

Long, X., Ballmer, M. D., Córdoba, A. M. C., & Li, C. F. (2019). Mantle Melting and Intraplate Volcanism Due to Self-Buoyant Hydrous Upwellings From the Stagnant Slab That Are Conveyed by Small-Scale Convection. *Geochemistry, geophysics, geosystems : G3*, *20*(11), 4972-4997. https://doi.org/10.1029/2019GC008591

Luth, R. W. (2003). Mantle Volatiles-Distribution and Consequences. In (Vol. 2-9, pp. 319-361). https://doi.org/10.1016/B0-08-043751-6/02124-1

Magni, V., Bouilhol, P., & van Hunen, J. (2014). Deep water recycling through time. *Geochem. Geophys. Geosyst*, *15*(11), 4203-4216. https://doi.org/10.1002/2014GC005525

Mather, B. R., Dietmar Müller, R., Seton, M., Ruttor, S., Nebel, O., & Mortimer, N. (2020). Intraplate volcanism triggered by bursts in slab flux. *Sci Adv*, *6*(51). https://doi.org/10.1126/sciadv.abd0953

Matthews, K. J., Maloney, K. T., Zahirovic, S., Williams, S. E., Seton, M., & Müller, R. D. (2016). Global plate boundary evolution and kinematics since the late Paleozoic. *Global and planetary change*, *146*, 226-250. https://doi.org/10.1016/j.gloplacha.2016.10.002

Meier, U., Trampert, J., & Curtis, A. (2009). Global variations of temperature and water content in the mantle transition zone from higher mode surface waves. *Earth and planetary science letters*, *282*(1), 91-101. https://doi.org/10.1016/j.epsl.2009.03.004

Menant, A., Jolivet, L., Tuduri, J., Loiselet, C., Bertrand, G., & Guillou-Frottier, L. (2018). 3D subduction dynamics: A first-order parameter of the transition from copper- to gold-rich deposits in the eastern Mediterranean region. *Ore geology reviews*, *94*, 118-135. https://doi.org/10.1016/j.oregeorev.2018.01.023

Merle, R., Marzoli, A., Reisberg, L., Bertrand, H., Nemchin, A., Chiaradia, M., Callegaro, S., Jourdan, F., Bellieni, G., Kontak, D., Puffer, J., & Gregory McHone, J. (2014). Sr, Nd, Pb and Os isotope systematics of CAMP tholeiites from Eastern North America (ENA): Evidence of a subduction-enriched mantle source. *Journal of petrology*, *55*(1), 133-180. https://doi.org/10.1093/petrology/egt063

Miles, R. E. (1965). On random rotations in R3. *Biometrika*, *52*(3-4), 636-639. https://doi.org/10.1093/biomet/52.3-4.636

Motoki, M. H., & Ballmer, M. D. (2015). Intraplate volcanism due to convective instability of stagnant slabs in the mantle transition zone. *Geochem. Geophys. Geosyst*, *16*(2), 538-551. https://doi.org/10.1002/2014GC005608

Murakami, M., Hirose, K., Yurimoto, H., Nakashima, S., & Takafuji, N. (2002). Water in Earth's Lower Mantle. *Science*, *295*(5561), 1885-1887. https://doi.org/10.1126/science.1065998

Müller, R. D., Cannon, J., Qin, X., Watson, R. J., Gurnis, M., Williams, S., Pfaffelmoser, T., Seton, M., Russell, S. H. J., & Zahirovic, S. (2018). GPlates: Building a Virtual Earth Through Deep Time. *Geochemistry, geophysics, geosystems : G3*, *19*(7), 2243-2261. https://doi.org/10.1029/2018GC007584

Nestola, F., & Smyth, J. R. (2016). Diamonds and water in the deep Earth: a new scenario. *International geology review*, *58*(3), 263-276. https://doi.org/10.1080/00206814.2015.1056758

Ohtani, E. (2005). Water in the mantle. *Elements (Quebec)*, *1*(1), 25-30. https://doi.org/10.2113/gselements.1.1.25

Parai, R., & Mukhopadhyay, S. (2012). How large is the subducted water flux? New constraints on mantle regassing rates. *Earth and planetary science letters*, *317-318*, 396-406. https://doi.org/10.1016/j.epsl.2011.11.024

Parmentier, E. M., & Buck, W. R. (1986). Convection beneath young oceanic lithosphere: Implications for thermal structure and gravity. *J. Geophys. Res*, *91*(B2), 1961-1974. https://doi.org/10.1029/JB091iB02p01961

Parsons, B., & McKenzie, D. (1978). Mantle convection and the thermal structure of the plates. *J. Geophys. Res*, *83*(B9), 4485-4496. https://doi.org/10.1029/JB083iB09p04485

Parsons, B., & Sclater, J. G. (1977). An analysis of the variation of ocean floor bathymetry and heat flow with age. *J. Geophys. Res*, *82*(5), 803-827. https://doi.org/10.1029/JB082i005p00803

Pearson, D. G., Brenker, F. E., Nestola, F., McNeill, J., Nasdala, L., Hutchison, M. T., Matveev, S., Mather, K., Silversmit, G., Schmitz, S., Vekemans, B., & Vincze, L. (2014). Hydrous mantle transition zone indicated by ringwoodite included within diamond. *Nature*, *507*(7491), 221-224. https://doi.org/10.1038/nature13080

Peslier, A. H., & Bizimis, M. (2015). Water in Hawaiian peridotite minerals: A case for a dry metasomatized oceanic mantle lithosphere. *Geochem. Geophys. Geosyst*, *16*(4), 1211-1232. https://doi.org/10.1002/2015GC005780

Peslier, A. H., Schönbächler, M., Busemann, H., & Karato, S.-I. (2017). Water in the Earth's Interior: Distribution and Origin. *Space science reviews*, *212*(1-2), 743-810. https://doi.org/10.1007/s11214-017-0387-z

Pratt, M. J., Wysession, M. E., Aleqabi, G., Wiens, D. A., Nyblade, A. A., Shore, P., Rambolamanana, G., Andriampenomanana, F., Rakotondraibe, T., Tucker, R. D., Barruol, G., & Rindraharisaona, E. (2017). Shear velocity structure of the crust and upper mantle of Madagascar derived from surface wave tomography. *Earth and planetary science letters*, *458*, 405-417. https://doi.org/10.1016/j.epsl.2016.10.041

Raddick, M. J., Parmentier, E. M., & Scheirer, D. S. (2002). Buoyant decompression melting: A possible mechanism for intraplate volcanism. *J. Geophys. Res*, *107*(B10), ECV 7-1-ECV 7-14. https://doi.org/10.1029/2001JB000617

Rasoazanamparany, C., Widom, E., Kuentz, D., Raharimahefa, T., Rakotondravelo, K., & Rakotondrazafy, A. M. F. (2021). Geochemistry and mantle source characteristics of the Itasy volcanic field: Implications for the petrogenesis of basaltic magmas in intra-continental-rifts. *Geochimica et cosmochimica acta*, *300*, 137-163. https://doi.org/10.1016/j.gca.2021.02.025

Renka, R. (1997a). Algorithm 772: STRIPACK: Delaunay triangulation and Voronoi diagram on the surface of a sphere. *ACM transactions on mathematical software*, *23*(3), 416-434. https://doi.org/10.1145/275323.275329

Renka, R. (1997b). Algorithm 773: SSRFPACK: interpolation of scattered data on the surface of a sphere with a surface under tension. *ACM transactions on mathematical software*, *23*(3), 435-442. https://doi.org/10.1145/275323.275330

Richter, F. M., & Parsons, B. (1975). On the interaction of two scales of convection in the mantle. *J. Geophys. Res*, *80*(17), 2529-2541. https://doi.org/10.1029/JB080i017p02529

Ritter, J. R. R., Jordan, M., Christensen, U. R., & Achauer, U. (2001). A mantle plume below the Eifel volcanic fields, Germany. *Earth and planetary science letters*, *186*(1), 7-14. https://doi.org/10.1016/S0012-821X(01)00226-6

Rizzo, A. L., Faccini, B., Casetta, F., Faccincani, L., Ntaflos, T., Italiano, F., & Coltorti, M. (2021). Melting and metasomatism in West Eifel and Siebengebirge Sub-Continental Lithospheric Mantle: Evidence from concentrations of volatiles in fluid inclusions and petrology of ultramafic xenoliths. *Chemical geology*, *581*, 120400. https://doi.org/10.1016/j.chemgeo.2021.120400

Rüpke, L. H., Morgan, J. P., Hort, M., & Connolly, J. A. D. (2004). Serpentine and the subduction zone water cycle. *Earth and planetary science letters*, *223*(1), 17-34. https://doi.org/10.1016/j.epsl.2004.04.018

Sandu, C., Lenardic, A., & McGovern, P. (2011). The effects of deep water cycling on planetary thermal evolution. *J. Geophys. Res*, *116*(B12). https://doi.org/10.1029/2011JB008405

Sandwell, D. T., Winterer, E. L., Mammerickx, J., Duncan, R. A., Lynch, M. A., Levitt, D. A., & Johnson, C. L. (1995). Evidence for diffuse extension of the Pacific Plate from Pukapuka ridges and cross-grain gravity lineations. *J. Geophys. Res*, *100*(B8), 15087-15099. https://doi.org/10.1029/95JB00156

Schilling, J. G. (1973). Afar Mantle Plume: Rare Earth Evidence. *Nature. Physical science (London)*, *242*(114), 2-5. https://doi.org/10.1038/physci242002a0

Schmandt, B., Jacobsen, S. D., Becker, T. W., Liu, Z., & Dueker, K. G. (2014). Dehydration melting at the top of the lower mantle. *Science (American Association for the Advancement of Science)*, *344*(6189), 1265-1268. https://doi.org/10.1126/science.1253358

Schmeling, H., Marquart, G., & Nawa, V. (2017). The role of hydrothermal cooling of the oceanic lithosphere for ocean floor bathymetry and heat flow: HYDROTHERMAL

COOLING OF LITHOSPHERE. *Journal of geophysical research. Solid earth*, *122*(5), 3934-3952. https://doi.org/10.1002/2016JB013881

Schulze, K., Marquardt, H., Kawazoe, T., Boffa Ballaran, T., McCammon, C., Koch-Müller, M., Kurnosov, A., & Marquardt, K. (2018). Seismically invisible water in Earth's transition zone? *Earth and planetary science letters*, *498*, 9-16. https://doi.org/10.1016/j.epsl.2018.06.021

Sclater, J. G., Jaupart, C., & Galson, D. (1980). The heat flow through oceanic and continental crust and the heat loss of the Earth. *Rev. Geophys*, *18*(1), 269-311. https://doi.org/10.1029/RG018i001p00269

Sheng, J., Liao, J., & Gerya, T. (2016). Numerical modeling of deep oceanic slab dehydration: Implications for the possible origin of far field intra-continental volcanoes in northeastern China. *Journal of Asian earth sciences*, *117*, 328-336. https://doi.org/10.1016/j.jseaes.2015.12.022

Shirey, S. B., Wagner, L. S., Walter, M. J., Pearson, D. G., & van Keken, P. E. (2021). Slab Transport of Fluids to Deep Focus Earthquake Depths—Thermal Modeling Constraints and Evidence From Diamonds. *AGU advances*, *2*(2). https://doi.org/10.1029/2020AV000304

Smith, E., Conrad, C. P., Plank, T., Tibbetts, A., & Keenan, D. (2008). Testing models for basaltic volcanism: Implications for Yucca Mountain, Nevada. *Transactions of the American Nuclear Society*, 157-164.

Smyth, J. R., & Jacobsen, S. D. (2006). Nominally Anhydrous Minerals and Earth's Deep Water Cycle. In (Vol. 168, pp. 1-11). Washington, D. C: American Geophysical Union. https://doi.org/10.1029/168GM02

Soltanmohammadi, A., Grégoire, M., Rabinowicz, M., Gerbault, M., Ceuleneer, G., Rahgoshay, M., Bystricky, M., & Benoit, M. (2018). Transport of volatile-rich melt from the mantle transition zone via compaction pockets: Implications for mantle metasomatism and the origin of Alkaline Lavas in the Turkish-Iranian plateau. *Journal of petrology*, *59*(12), 2273-2310. https://doi.org/10.1093/petrology/egy097

Steinberger, B., Rathnayake, S., & Kendall, E. (2021). The Indian Ocean Geoid Low at a plume-slab overpass. *Tectonophysics*, *817*, 229037. https://doi.org/10.1016/j.tecto.2021.229037

Suetsugu, D., Inoue, T., Yamada, A., Zhao, D., & Obayashi, M. (2006). Towards Mapping the Three-Dimensional Distribution of Water in the Transition Zone from P-Velocity Tomography and 660-Km Discontinuity Depths. In (pp. 237-249). Washington, D. C: American Geophysical Union. https://doi.org/10.1029/168GM18

Sun, W., Ding, X., Hu, Y.-H., & Li, X.-H. (2007). The golden transformation of the Cretaceous plate subduction in the west Pacific. *Earth and planetary science letters*, *262*(3), 533-542. https://doi.org/10.1016/j.epsl.2007.08.021

Syracuse, E. M., van Keken, P. E., & Abers, G. A. (2010). The global range of subduction zone thermal models. *Physics of the earth and planetary interiors*, *183*(1-2), 73-90. https://doi.org/10.1016/j.pepi.2010.02.004

Thompson, A. B. (1992). Water in the Earth's upper mantle. *Nature (London)*, *358*(6384), 295-302. https://doi.org/10.1038/358295a0

Till, C. B., Elkins-Tanton, L. T., & Fischer, K. M. (2010). A mechanism for low-extent melts at the lithosphere-asthenosphere boundary. *Geochem. Geophys. Geosyst*, *11*(10), n/a. https://doi.org/10.1029/2010GC003234

Torsvik, T. H., Steinberger, B., Shephard, G. E., Doubrovine, P. V., Gaina, C., Domeier, M., Conrad, C. P., & Sager, W. W. (2019). Pacific-Panthalassic Reconstructions: Overview, Errata and the Way Forward. *Geochemistry, geophysics, geosystems : G3*, *20*(7), 3659-3689. https://doi.org/10.1029/2019GC008402

Uieda, L., Tian, D., Leong, W. J., Jones, M., Schlitzer, W., Toney, L., Grund, M., Yao, J., Magen, Y., Materna, K., Newton, T., Anant, A., Ziebarth, M., Wessel, P., & Quinn, J. (2021).

PyGMT: A Python interface for the Generic Mapping Tools. *Zenodo*, *v0.5.0*. https://doi.org/10.5281/zenodo.5607255

Utada, H., Koyama, T., Obayashi, M., & Fukao, Y. (2009). A joint interpretation of electromagnetic and seismic tomography models suggests the mantle transition zone below Europe is dry. *Earth and planetary science letters*, *281*(3), 249-257. https://doi.org/10.1016/j.epsl.2009.02.027

van der Lee, S., Regenauer-Lieb, K., & Yuen, D. A. (2008). The role of water in connecting past and future episodes of subduction. *Earth and planetary science letters*, *273*(1-2), 15-27. https://doi.org/10.1016/j.epsl.2008.04.041

van der Meer, D. G., van Hinsbergen, D. J. J., & Spakman, W. (2018). Atlas of the underworld: Slab remnants in the mantle, their sinking history, and a new outlook on lower mantle viscosity. *Tectonophysics*, *723*, 309-448. https://doi.org/10.1016/j.tecto.2017.10.004

van Keken, P. E., Hacker, B. R., Syracuse, E. M., & Abers, G. A. (2011). Subduction factory: 4. Depth-dependent flux of H2O from subducting slabs worldwide. *J. Geophys. Res*, *116*(B1), n/a. https://doi.org/10.1029/2010JB007922

Vollmer, R., Ogden, P., Schilling, J. G., Kingsley, R. H., & Waggoner, D. G. (1984). Nd and Sr isotopes in ultrapotassic volcanic rocks from the Leucite Hills, Wyoming. *Contributions to mineralogy and petrology*, *87*(4), 359-368. https://doi.org/10.1007/BF00381292

Wallmann, K. (2001). The geological water cycle and the evolution of marine delta O-18 values. *Geochimica et cosmochimica acta*, *65*(15), 2469-2485. https://doi.org/10.1016/S0016-7037(01)00603-2

Wang, X.-C., Wilde, S. A., Li, Q.-L., & Yang, Y.-N. (2015). Continental flood basalts derived from the hydrous mantle transition zone. *Nat Commun*, *6*(1), 7700-7700. https://doi.org/10.1038/ncomms8700

Wang, X.-J., Chen, L.-H., Hofmann, A. W., Mao, F.-G., Liu, J.-Q., Zhong, Y., Xie, L.-W., & Yang, Y.-H. (2017). Mantle transition zone-derived EM1 component beneath NE China: Geochemical evidence from Cenozoic potassic basalts. *Earth and planetary science letters*, *465*, 16-28. https://doi.org/10.1016/j.epsl.2017.02.028

Wang, Y., Pavlis, G. L., & Li, M. (2019). Heterogeneous distribution of water in the mantle transition zone inferred from wavefield imaging. *Earth and planetary science letters*, *505*, 42-50. https://doi.org/10.1016/j.epsl.2018.10.010

Wessel, P., Luis, J. F., Uieda, L., Scharroo, R., Wobbe, F., Smith, W. H. F., & Tian, D. (2019). The Generic Mapping Tools Version 6. *Geochemistry, geophysics, geosystems : G3*, *20*(11), 5556-5564. https://doi.org/10.1029/2019GC008515

Williams, S., Cannon, J., Qin, X., & Müller, D. (2017). PyGPlates-a GPlates Python library for data analysis through space and deep geological time. EGU General Assembly Conference Abstracts,

Wirth, R., Vollmer, C., Brenker, F., Matsyuk, S., & Kaminsky, F. (2007). Inclusions of nanocrystalline hydrous aluminium silicate “Phase Egg” in superdeep diamonds from Juina (Mato Grosso State, Brazil). *Earth and planetary science letters*, *259*(3), 384-399. https://doi.org/10.1016/j.epsl.2007.04.041

Wright, K. (2006). Atomistic models of OH defects in nominally anhydrous minerals. *Reviews in mineralogy and geochemistry*, *62*(1), 67-83. https://doi.org/10.2138/rmg.2006.62.4 (Reviews in Mineralogy & Geochemistry)

Yang, J., & Faccenda, M. (2020). Intraplate volcanism originating from upwelling hydrous mantle transition zone. *Nature*, *579*(7797), 88-91. https://doi.org/10.1038/s41586-020-2045-y

Yoshino, T., Manthilake, G., Matsuzaki, T., & Katsura, T. (2008). Dry mantle transition zone inferred from the conductivity of wadsleyite and ringwoodite. *Nature*, *451*(7176), 326-329. https://doi.org/10.1038/nature06427

Zhong, S., Zuber, M. T., Moresi, L., & Gurnis, M. (2000). Role of temperature-dependent viscosity and surface plates in spherical shell models of mantle convection. *J. Geophys. Res*, *105*(B5), 11063-11082. https://doi.org/10.1029/2000JB900003

Zindler, A., & Hart, S. (1986). Chemical Geodynamics. *Annual review of earth and planetary sciences*, *14*(1), 493-571. https://doi.org/10.1146/annurev.ea.14.050186.002425